

**NOAA NESDIS  
CENTER for SATELLITE APPLICATIONS and  
RESEARCH**

**GOES-R Advanced Baseline Imager (ABI)  
Algorithm Theoretical Basis Document  
For  
Suspended Matter/Aerosol Optical Depth and  
Aerosol Size Parameter**

*Aerosol Product Application Team  
of the  
AWG Aerosols/Air Quality/Atmospheric Chemistry Team*

Version 3.0  
July 30, 2012

## TABLE OF CONTENT

LIST OF FIGURES .....	5
LIST OF TABLES .....	7
LIST OF ACRONYMS .....	9
ABSTRACT .....	11
1 INTRODUCTION .....	12
1.1 Purpose of This Document .....	12
1.2 Who Should Use This Documents .....	13
1.3 Inside Each Section .....	13
1.4 Related Documents .....	13
1.5 Revision History .....	14
2 OBSERVING SYSTEM OVERVIEW .....	14
2.1 Products Generated .....	14
2.2 Instrument Characteristics .....	16
3 ALGORITHM DESCRIPTION .....	17
3.1 Algorithm Overview .....	18
3.2 Processing Outline .....	20
3.3 Algorithm Input .....	20
3.3.1 Primary sensor data .....	20
3.3.2 Ancillary data .....	21
3.3.3 Derived data .....	22
3.4 Theoretical Description .....	24
3.4.1 Physical and mathematical description for aerosol optical depth retrieval over ocean .....	24
3.4.1.1 Strategy .....	24
3.4.1.2 Aerosol models .....	25
3.4.1.3 Calculation of TOA reflectance .....	26
3.4.1.4 Aerosol retrieval algorithm over ocean .....	28
3.4.1.5 Calculation of ocean surface reflectance .....	30
3.4.1.6 Sensitivity study .....	31
3.4.2 Physical and mathematical description for aerosol optical depth retrieval over land .....	35
3.4.2.1 Strategy .....	35
3.4.2.2 Aerosol models .....	36
3.4.2.3 Retrieval of land surface reflectance .....	37
3.4.2.4 Calculation of TOA reflectance .....	39
3.4.2.5 Aerosol retrieval algorithm over land .....	39
3.4.2.6 Sensitivity study .....	43
3.4.3 Calculation of aerosol size parameter .....	46
3.4.4 Calculation of suspended matter mass concentration .....	46
3.4.5 Look-up table .....	48
3.4.5.1 Atmospheric look-up table .....	49
3.4.5.2 Ocean surface reflectance look-up table .....	54
3.4.6 Gas transmittance parameterization .....	55
3.4.7 Calculation of molecular atmospheric functions .....	58

3.4.8	Algorithm output .....	61
4	TEST DATA SETS AND OUTPUTS .....	65
4.1	Input Data Sets .....	65
4.1.1	Development of a fast simulator to simulate cloud-free ABI TOA reflectance .....	65
4.1.1.1	One MODIS/Terra granule for dust case over ocean .....	66
4.1.1.2	Two MODIS/Aqua granules for smoke case over land .....	66
4.1.2	MODIS radiance as proxy data sets .....	70
4.2	Output Analysis from Input Data Sets .....	70
4.2.1	Precisions and accuracy estimates .....	70
4.2.1.1	Estimates using simulated input radiances .....	71
4.2.1.2	Estimates using MODIS reflectances .....	72
4.2.1.3	Framework validation using MODIS radiance .....	75
4.2.2	Error Budget .....	76
5	PRACTICAL CONSIDERATIONS .....	82
5.1	Numerical Computation Considerations .....	82
5.2	Programming and Procedural Considerations .....	82
5.3	Quality Assessment and Diagnostics .....	82
5.4	Exception Handling .....	82
5.5	Algorithm Validation .....	83
6	ASSUMPTIONS AND LIMITATIONS .....	83
6.1	Performance .....	84
6.2	Assumed Sensor Performance .....	84
6.3	Pre-Planned Product Improvements .....	85
6.3.1	Retrieval over bright land surface .....	85
6.3.2	Additional internal tests .....	85
	REFERENCES .....	85
	APPENDIX .....	90
A.	Effect of Instrument noise on AOD Retrieval .....	90
B.	Sunglint directional reflectance .....	97
C.	Internal checks for aerosol retrieval .....	99
C.1.	Snow/ice contamination over land .....	99
C.2.	Glint .....	100
C.3.	Turbid water over ocean .....	100
	Appendix D: Common Ancillary Data Sets .....	102
1.	LAND_MASK_NASA_1KM .....	102
a.	<i>Data description</i> .....	102
b.	<i>Interpolation description</i> .....	102
2.	MDS_L2_CLD_MASK_FILE .....	102
a.	<i>Data description</i> .....	102
b.	<i>Interpolation description</i> .....	103
3.	MDS_L2_OZON_5KM_FILE .....	103
a.	<i>Data description</i> .....	103
b.	<i>Interpolation description</i> .....	103
4.	MDS_L2_TPW_5KM_FILE .....	103
a.	<i>Data description</i> .....	103

b.	<i>Interpolation description</i> .....	104
5.	NWP_GFS.....	104
a.	<i>Data description</i> .....	104
b.	<i>Interpolation description</i> .....	104
6.	SFC_ELEV_GLOBE_1KM.....	106
a.	<i>Data description</i> .....	106
b.	<i>Interpolation description</i> .....	106
7.	SNOW_MASK_IMS_SSMI.....	106
a.	<i>Data description</i> .....	106
b.	<i>Interpolation description</i> .....	106

## LIST OF FIGURES

Figure 3-1. High level flowchart of the AOD retrieval illustrating the main processing sections. ....	19
Figure 3-2. Average uncertainties in the retrieved aerosol optical depth at 0.55 $\mu\text{m}$ , fine-mode weight and percentage of model misidentification for all sensitivity tests.....	34
Figure 3-3. Angular dependence of the uncertainty of retrieved $\tau_{550}$ (left) and FMW (right) for one case: increasing TOA reflectance at 1.61 $\mu\text{m}$ by 3%, applied to the second fine mode #2 and coarse mode #1 with 0.4 FMW and $\tau_{550} = 0.2$ . Solar zenith angle is 42.83°. In the figure, local zenith angle increases in the radial direction; PHI represents the relative azimuth angle.....	34
Figure 3-4. Uncertainty of retrieved aerosol optical depth at 0.55 $\mu\text{m}$ when all ABI channels used for aerosol retrieval over water are perturbed by 3% or 5% (systematic bias plus random noise).....	35
Figure 3-5. Relative frequency of 0.86- $\mu\text{m}$ NDVI for 1.24- $\mu\text{m}$ NDVI $\geq 0.2$ (vegetation-based in blue) and 1.24- $\mu\text{m}$ NDVI $< 0.2$ (soil-based in red).....	39
Figure 3-6. Flowchart of aerosol retrieval over land.....	42
Figure 3-7. Average uncertainties in the retrieved aerosol optical depth at 0.55 $\mu\text{m}$ (top) and percentage of model misidentification (bottom) for the sensitivity tests of the aerosol retrieval over land. ....	44
Figure 3-8. Sensitivity test results of aerosol retrieval over land with TOA reflectance increased by 5% in all channels. a) relative uncertainty of retrieved $\tau_{550}$ as functions of surface reflectance and $\tau_{550}$ ; b) absolute uncertainty of retrieved $\tau_{550}$ as functions of surface reflectance and $\tau_{550}$ ; c) percentage of misidentification for each aerosol model; d) relative uncertainty of retrieved $\tau_{550}$ as function of scattering angle. ....	45
Figure 3-9. Uncertainty of retrieved aerosol optical depth at 0.55 $\mu\text{m}$ when all ABI channels used for aerosol retrieval over land are perturbed by 3% or 5% (systematic bias plus random noise).....	46
Figure 3-10. The layout of atmospheric reflectance array for a given aerosol model, aerosol optical depth and wavelength (top) and indexing vector (bottom). The starting position of each block can be accessed by the corresponding element in the indexing vector. ....	53
Figure 3-11. Fitting water vapor transmission (left, where original data in black and fitted data in color) and relative difference in percentage between fitted and original transmission (right) with absorber amount for ABI channels 2, 3, 5, and 6. ....	56
Figure 3-12. Left: Fit of ozone transmission (where original data are in black and fitted data are in color). Right: Relative difference in percentage between fitted and original transmission with absorber amount for ABI channels 1 and 2. ....	57
Figure 4-1. Flow chart of fast simulation scheme for GOES-R ABI radiance field. ....	67
Figure 4-2. Example of ABI reflectances simulated from one MODIS/TERRA granule at UTC 20:10 on September 30 (day 273), 2002. Top left: RGB image; top right: AOD: aerosol optical depth at 550 nm; second row left: fine mode to coarse mode	

optical depth weight (FMW); second row right: wind speed; third and fourth rows: simulated for channel 2, 3, 5, and 6 reflectances.....	68
Figure 4-3. Reflectance fields simulated for MODIS/AQUA granules at UTC: 18:15 on April 12, 2003 (left panel) and at UTC 16:45 on May 16, 2007 (right panel). RGB images are shown in the top row. ....	69
Figure 4-4. Comparison of AOD (left) and fine-mode weight (FW) in percentage (right) from the MODIS reference with those retrieved from the ABI algorithm for a selected test scene over ocean. ....	71
Figure 4-5. Comparison of retrieved and reference (MODIS) AOD for two MODIS granules: (left) May 16, 2007, (right) April 12, 2002. ....	72
Figure 4-6. Comparison of ABI AOD with AERONET AOD at 550 nm over land (left) and over ocean (right) using collocated AERONET-MODIS dataset for years 2000-2009. ....	73
Figure 4-7. Comparison of ABI Ångström Exponent with AERONET over land (left) and over ocean (right) using collocated AERONET-MODIS dataset for years 2000-2009. ....	74
Figure 4-8. Aerosol optical depths at 550 nm, for one MODIS granule at 03:25 UTC on June 4, 2005, generated by the AIT framework run (left) and the AWG research code (right). ....	75
Figure 4-9. Comparison of framework ABI AOD with AERONET AOD at 550 nm over land and over water from 2-day framework run of Aug. 24-25, 2006. ....	76
Figure 4-10. Mean values and standard deviations of relative AOD uncertainty for uncertainties in ozone, water vapor (watvap) and surface pressure (sfcpre) over land and water, and dust presence test in SWIR channel (dust in swir) over land.....	80
Figure 4-11. Land aerosol model misidentification for ozone, water vapor (watvap), surface pressure (sfcpre) and cloud contamination (cloud) tests.....	81
Figure 4-12. Mean values and standard deviations of fine-mode weight (FMW) uncertainty over water for ozone, water vapor (watvap), surface pressure (sfcpre), cloud contamination (cloud), and surface wind speed (wspd) tests. ....	81
Figure A-1. Locations selected for aerosol retrievals in the GOES east and west domains. ....	93
Figure C-1: Relative frequency of 1.6- $\mu\text{m}$ NDSI, i.e. $(\rho_{0.86} - \rho_{1.61})/(\rho_{0.86} + \rho_{1.61})$ , for 1.24- $\mu\text{m}$ NDSI (i.e. $(\rho_{0.86} - \rho_{1.24})/(\rho_{0.86} + \rho_{1.24}) > 0.05$ (in blue) and 1.24- $\mu\text{m}$ NDSI $\leq 0.05$ (in red) using MODIS reflectances. ....	100
Figure C-2: Relative frequency of $\Delta\rho_{0.66}$ for $\Delta\rho_{0.55} > 0.01$ (turbid water indicator, in blue) and $\Delta\rho_{0.55} \leq 0.01$ (in red) using MODIS reflectances. ....	101

## LIST OF TABLES

Table 2-1. GOES-R mission requirements for Aerosol Optical Depth. ....	15
Table 2-2. Product qualifiers for Aerosol Optical Depth. LZA=local zenith angle. ....	15
Table 2-3. GOES-R mission requirements for Aerosol Particle Size. ....	15
Table 2-4. Product qualifiers for Aerosol Particle Size. LZA=local zenith angle. ....	16
Table 2-5. Wavelengths, spatial resolution, and noise characteristics of ABI channels. ...	16
Table 3-1. ABI primary sensor input data. ....	20
Table 3-2. ABI dynamic ancillary input data. ....	21
Table 3-3. Non-ABI dynamic ancillary input data. ....	22
Table 3-4. Non-ABI Static ancillary input data. ....	22
Table 3-5. ABI derived input data. ....	23
Table 3-6. Microphysical properties of ocean aerosols (Fine modes: F1-F4; Coarse modes: C1-C5) used in the ABI algorithm (refractive indices, number median ( $r_g$ ) and standard deviation ( $\sigma_g$ ), and effective radius ( $r_{eff}$ )) ....	26
Table 3-7. Whitecap effective reflectance and underwater reflectance. ....	30
Table 3-8. Seawater index of refraction and extinction coefficient for ABI bands. ....	31
Table 3-9. Geometry and aerosol conditions covered by the sensitivity tests. ....	31
Table 3-10. Microphysical properties of land aerosols used in ABI algorithm. ....	37
Table 3-11. Inverse of mass-extinction coefficients for over-land aerosols [ $\text{cm}^2/\mu\text{g}$ ] ....	48
Table 3-12. Extinction Properties ( $\pi Q_{ext} M^{(2)}$ in $\text{cm}^2$ and $M^{(3)}$ in $\mu\text{m}^3$ ) of Ocean Aerosol Models. ....	48
Table 3-13. Contents of atmospheric look-up table. ....	49
Table 3-14. Discrete values/description of atmospheric LUT dimensions. ....	50
Table 3-15. Contents of ocean surface reflectance look-up table. ....	54
Table 3-16. Discrete values of ocean reflectance LUT dimensions. ....	54
Table 3-17. Gas absorption fitting coefficients. ....	58
Table 3-18. Rayleigh optical depth at standard surface pressure for the ABI channels. ....	59
Table 3-19. ABI aerosol algorithm output. ....	61
Table 3-20. Detailed input and output quality and critical path flags. ....	62
Table 4-1. Channel mapping between ABI and MODIS. ....	65
Table 4-2. AOD validation statistics over land obtained from the collocated AERONET- MODIS dataset for years 2000-2009. RMSE is the root mean square error. MinErr and MaxErr are minimum and maximum differences, respectively. ....	73
Table 4-3. AOD validation statistics over ocean obtained from the collocated AERONET-MODIS dataset for years 2000-2009. RMSE is the root mean square error. MinErr and MaxErr are minimum and maximum differences, respectively. ...	73
Table 4-4. Accuracy and precision of ABI AOD from comparison with AERONET AOD at 550 nm over land (left) and over water (right) using collocated AERONET- MODIS dataset for years 2000-2009. F&PS requirements are in parenthesis. ....	74
Table 4-5. Accuracy and precision of Ångström Exponent retrieval from collocated AERONET-MODIS dataset for years 2000-2009. ....	75
Table 4-6. Accuracy and precision for different AOD ranges from 2-day framework run. .....	76
Table 4-7. Geometry and aerosol conditions. ....	77

Table 4-8. Uncertainty levels and values of input atmospheric and surface parameters...	78
Table 4-9. Mean values and standard deviations of relative AOD errors due to cloud contamination and error in wind speed. (AOD550: aerosol optical depth at 550 nm; wspd: wind speed) .....	79
Table A-1. $\Delta\rho$ and $\tau$ for the ABI “aerosol” channels.....	90
Table A-2. Aerosol optical depth sensitivity $\Delta\tau$ for ABI ocean aerosol models.....	91
Table A-3. Signal-to-noise ratio for optical depth for ocean aerosol models at 2-km resolution. ....	91
Table A-4. Signal-to-noise ratio of optical depth for land aerosol models at 2-km resolution. ....	91
Table A-5. Aerosol optical depth signal-to-noise ratio for ocean aerosol models at 2.25 $\mu\text{m}$ for different spatial resolutions. ....	92
Table A-6. Aerosol optical depth signal-to-noise ratio for land aerosol models at 2.25 $\mu\text{m}$ for different spatial resolutions.....	92
Table A-7. Bias and standard deviation (Std.dev) of AOD retrieved over water from noisy reflectances relative to that from noise-free reflectance.....	94
Table A-8. Bias and standard deviation (Std.dev) of the Ångström Exponent retrieved over water from noisy reflectance relative to that from noise-free reflectance.....	95
Table A-9. Bias and standard deviation (Std.dev) of AOD retrieved over land from noisy reflectances relative to that from noise-free reflectance.....	95
Table A-10. Bias and standard deviation (Std.dev) of the Ångström Exponent retrieved over land from noisy reflectance relative to that from noise-free reflectance.....	96

## LIST OF ACRONYMS

AAA	Aerosol, Air Quality and Air chemistry
ABI	Advanced Baseline Imager
AERONET	AERosol ROBotic NETwork
AIT	Algorithm Integration Team
AOD	Aerosol Optical Depth
ASP	Aerosol Size Parameter
ASTER	Advanced Space Thermal Emission and Reflection Radiometer
ATBD	Algorithm Theoretical Basis Document
ATIP	Algorithm and Test Implementation Plan
AWG	Algorithms Working Group
BRDF	Bi-directional Reflectance Distribution Function
CONUS	Continental US
FMW	Fine Mode Weight
F&PS	Functional and Performance Specification document
GFS	Global Forecast System
GOES	Geostationary Operational Environmental Satellite
IMS	Interactive Multisensor Snow and Ice Mapping System
JPSS	Joint Polar Satellite System
LUT	Lookup Table
MODIS	Moderate Resolution Imaging Spectroradiometer
MRD	Mission Requirements Document
NASA	National Aeronautics and Space Administration
NCEP	National Centers for Environmental Prediction
NDVI	Normalized Difference Vegetation Index
NESDIS	National Environmental Satellite, Data, and Information Service
NIR	Near Infrared
NOAA	National Oceanic and Atmospheric Administration
NPOESS	National Polar-orbiting Operational Environmental Satellite System
NWS	National Weather Service
PDF	Probability Distribution Function
PM <sub>2.5</sub>	Particulate Mass of particles smaller than 2.5 $\mu\text{m}$ in median diameter
PORD	Performance and Operation Requirements Document
RMS	Root Mean Square
RTM	Radiative Transfer Model
SWIR	Shortwave Infrared
SEBN	Surface Energy Balance Network
SEVIRI	Spinning Enhanced Visible and Infra-red Imager
TOA	Top of Atmosphere
TPW	Total Precipitable Water
UMBC	University of Maryland Baltimore County
VIIRS	Visible Infrared Imaging Radiometer Suite

VIS	Visible
-----	---------

## ABSTRACT

Atmospheric aerosols (liquid or solid particles suspended in the air) affect the radiative energy budget, the hydrological cycle, atmospheric circulation, land surface processes, and climate. They also play a role in air quality and have an impact on human health. Large-scale continuous characterization of atmospheric aerosols relies upon satellite remote sensing.

This document describes the algorithm for remote sensing of aerosol properties from the multispectral reflectances observed by the Advanced Baseline Imager (ABI) onboard the geostationary satellite GOES-R. The ABI aerosol algorithm retrieves the aerosol optical depth, suspended matter and aerosol size parameter at 2-km spatial and 5- and 15- minute temporal resolutions over the CONUS and full-disk domains, respectively, under daytime clear-sky conditions. Separate algorithms have been developed for the retrieval over land and over ocean due to the distinct surface properties and aerosol types. To aid rapid retrieval of aerosol properties, look-up tables of spectral atmospheric (aerosols plus molecules) optical functions (reflectance, transmittances and spherical albedo) are pre-calculated for a wide range of geometries and standard aerosol models at standard surface pressure. Over land, surface reflectance in the visible spectrum is obtained from the shortwave infrared reflectance based on pre-determined spectral relationships. Over ocean, the surface reflectance is modeled as the sum of underwater, whitecap, and sun glint direct reflection. Top of the atmosphere (TOA) reflectance is calculated from coupling the surface and atmospheric reflections, which is then compared with observations to determine the optimal solution for aerosol optical depth and aerosol type. The suspended matter is determined from the retrieved aerosol optical depth applying the mass extinction coefficient indicated by the aerosol model retrieved simultaneously with the optical depth. Aerosol size parameter (Ångström Exponent) is calculated from retrieved spectral aerosol optical depths. Validation of the ABI algorithm is performed with proxy data from MODIS. The retrieved aerosol optical depth and Ångström exponent are compared with ground measurements from AERONET. The comparisons indicate compliance with requirements for aerosol optical depth. Accuracy of Ångström exponent also meets the requirement, but the precision does not.

# 1 INTRODUCTION

Aerosols are liquid or solid particles suspended in the atmosphere. Aerosols modify the energy budget of the earth-atmosphere system in several ways. They directly scatter and absorb solar and thermal infrared radiation [e.g., Bohren and Huffman, 1983; Coakley et al., 1983; Charlson et al., 1992]; modify cloud amount, life time, and microphysical and radiative properties and therefore indirectly change the Earth-leaving radiation [e.g., Twomey, 1977; Albretch, 1989; Rosenfeld and Lensky, 1998]. Absorption of radiant energy by aerosols leads to heating of the troposphere and cooling of the surface, which can change the relative humidity and atmospheric stability thereby influencing cloud formation and precipitation [Hansen et al., 1997; Koren et al., 2004; Ackerman et al., 2000]. Consequently, aerosols can influence land surface process [Yu, et al., 2002], the global surface temperature [Coakley et al., 1983; Charlson et al., 1992; Ramanathan et al., 2001], climate and the hydrological cycle [Ramanathan et al., 2001], and ecosystems [Chameides et al., 1999]. As complex mixtures of particles and particle aggregates of varying chemical composition, aerosols also affect regional air quality and human health [Pope et al., 2002]. Epidemiological studies have linked exposure to PM<sub>2.5</sub> (particulate mass in units of  $\mu\text{g}/\text{m}^3$  for particles smaller than 2.5  $\mu\text{m}$  in median diameter) to a range of adverse health effects such as strokes, heart disease, respiratory ailments, and premature death [e.g. <http://www.epa.gov/region4/sesd/pm25/p2.html>].

Aerosols have high spatial and temporal variability due to the heterogeneous distribution of sources, short lifetime, and episodic feature of emission events. Therefore continuous global and regional characterization can only be realized through satellite remote-sensing. Real time monitoring of aerosol optical depth from Geostationary Operational Environmental Satellite (GOES) data are routinely conducted at the National Oceanic and Atmospheric Administration (NOAA). The current GOES algorithm uses only a single channel to retrieve aerosol optical depth (AOD). The need for using a fixed aerosol model does not allow estimation of size parameter in this algorithm. Moreover, the relatively large uncertainty in the estimated surface reflectance leads to inaccurate AOD for certain times and regions. The Advanced Baseline Imager (ABI) to be flown on the GOES-R series of NOAA geostationary meteorological satellites measures radiances at multiple wavelengths from the UV through the IR at high spatial resolution [Schmit et al., 2005]. In contrast to the one channel available in the solar reflective spectrum onboard the current GOES, GOES-R ABI has five channels between 0.47 and 2.25  $\mu\text{m}$  that are suitable for retrieving aerosol. Similar multi-channel instruments (e.g., Moderate Resolution Imaging Spectroradiometer, MODIS; Visible Infrared Imaging Radiometer Suite, VIIRS) have already been flown on various spacecrafts, and algorithms for retrieving aerosol from the measurements of these instruments are already available and tested (e.g., Kaufman et al., 1997; Remer et al., 2006; Levy et al., 2007; Vermote et al., 2006). The ABI aerosol algorithm described in this ATBD borrows heavily from these heritage algorithms.

## 1.1 Purpose of This Document

The Algorithm Theoretical Basis Document (ATBD) describes the theory and necessary assumptions for deriving aerosol properties from ABI aboard GOES-R. Details of the algorithm, the products, and their expected uncertainties (as estimated from proxy data) are also discussed.

## 1.2 Who Should Use This Documents

The intended users of this document are those interested in understanding the physical basis of the algorithm and use the aerosol retrieval outputs of this algorithm in applications requiring aerosol data. This document also provides information useful to anyone maintaining or modifying the original algorithm.

## 1.3 Inside Each Section

Specifically, this document is broken down into the following main sections:

- **Observing System Overview:** Provides the objectives of the algorithm, relevant characteristics of the instruments, and provides a brief description of the aerosol products generated by this algorithm.
- **Algorithm Description:** Provides detailed description of the physical and mathematical basis of the algorithm, the look-up tables, and inputs and outputs.
- **Test Data Sets and Output:** Describe the test data sets and processes to characterize the performance of the algorithm. This includes the method used for simulating proxy ABI data, algorithm output from the proxy ABI data, precision and accuracy estimates based on ground AERONET measurements, and error budget analysis.
- **Practical Considerations:** Provides an overview of the issues involving numerical computation, programming and procedures, quality assessment and diagnostics, and exception handling.
- **Assumptions and Limitations:** Provides an overview of the current limitations of the approach and gives the plan for overcoming these limitations with further algorithm development.

## 1.4 Related Documents

[GOES-R Series Mission Requirements Document](#) (MRD), P417-R-MRD-0070

[Geostationary Operational Environmental Satellite \(GOES\), GOES-R Series, Level I Requirements Document](#) (LIRD), P417-R-LIRD-0137

Geostationary Operational Environmental Satellite (GOES) GOES-R Series Spacecraft Functional and Performance Specification (F&PS), 417-R-PSPEC-0014

GOES-R ABI Performance and Operation Requirements Document (PORD)

GOES-R ABI *Suspended Matter/Optical Depth and Aerosol Size Parameter* Algorithm and Test Implementation Plan (ATIP) Document

GOES-R ABI *Suspended Matter/Optical Depth and Aerosol Size Parameter* Product Validation Plan Document

## 1.5 Revision History

*Version 3.0 – July 2012.* Version 3.0 is an update of the previous, Version 2.0 ATBD and incorporates the answers to questions raised by the Prime Contractor during the ATBD review reference code audit.

*Version 2.0 – September 2010.* Version 2.0 evaluates the ABI aerosol algorithm to meet the 100% requirements and follows the comments on Version 1.0 from the ADEB and IV&V reviewers. It was written by members of the Aerosol Team (I. Laszlo (lead), M. Zhou, H. Liu, and P. Ciren) of the GOES-R Algorithm Working Group (AWG) Aerosol, Air Quality and Air Chemistry (AAA) Application Team at NOAA/NESDIS/STAR.

*Version 1.0 – May 2009.* Version 1.0 of this document was written for the 80% maturity delivery. That revision evaluated the algorithm to meet the 80% requirements and addressed the comments on the draft version (Version 0.0) from the project office. Version 0.0 was delivered on September 30, 2008 to accompany the delivery of version 1 of the algorithm to the GOES-R AWG Algorithm Integration Team (AIT).

## 2 OBSERVING SYSTEM OVERVIEW

### 2.1 Products Generated

The algorithm is designed to retrieve the aerosol optical depth (AOD)/suspended matter (SM) and aerosol size parameter (ASP) from daytime clear-sky ABI spectral reflectances. The output is at 2-km spatial resolution and 5- and 15-minute temporal resolution during daytime. Due to the relatively weak aerosol signal and large uncertainties associated with surface reflectance, the current ABI algorithm does not attempt to do retrieval over bright surfaces, which include sun glint areas over water, desert, and bare soil surface over land. The primary retrieval product is AOD at 550 nm ( $\tau_{550}$ ), however AOD in five ABI channels (0.47, 0.64, 0.86, 1.61, and 2.25  $\mu\text{m}$ ) are also calculated based on the aerosol model selected by the algorithm during retrieval. Aerosol size parameter is represented by two Ångström Exponents corresponding to two pairs of wavelengths (0.47/0.86 and 0.86/2.25  $\mu\text{m}$ ). In addition, a single aerosol type over land, and a fine mode and a coarse

mode aerosol type along with the corresponding fine-mode weight over ocean are retrieved. The aerosol products are intended for air quality and weather applications.

Tables 2-1, 2-2, 2-3, and 2-4 show the current F&PS requirements and product qualifiers for aerosol optical depth and size parameter. Accuracy and precision requirements for suspended matter in terms of mass concentration are under study at the time of this writing; they will be included when approved by the GOES-R Program Office.

Table 2-1. GOES-R mission requirements for Aerosol Optical Depth.

Name	Geographic Coverage (G, H, C, M)	Vertical Resolution	Horizontal Resolution	Mapping Accuracy	Measurement Range	Measurement Accuracy	Refresh Rate/Coverage Time Option (Mode 3)	Refresh Rate Option (Mode 4)	Vendor Allocated Ground Latency	Product Measurement Precision
Aerosol Optical Depth	C, FD	Total Column	2 km	1 km	-1 – 5 in optical depth	Based on Aerosol Optical Depth ranges: Over land: <0.04: 0.06 0.04 – 0.80: 0.04 > 0.80: 0.12 Over water: < 0.40: 0.02 > 0.40: 0.10	CON US:5 min Full Disk: 15 min	CON US:5 min Full Disk: 15 min	CON S:50 sec Full Disk:1 59 sec	Based on Aerosol Optical Depth ranges: Over land: <0.04: 0.13 0.04 – 0.80: 0.25 > 0.80: 0.35 Over water: < 0.40: 0.15 > 0.40: 0.23

Table 2-2. Product qualifiers for Aerosol Optical Depth. LZA=local zenith angle.

Name	User & Priority	Geographic Coverage (G, H, C, M)	Temporal Coverage Qualifiers	Product Extent Qualifier	Cloud Cover Conditions Qualifier	Product Statistics Qualifier
Aerosol Optical Depth	GOES-R	C, FD	Daytime	Quantitative out to at least 60 degrees LZA (Threshold) and qualitative at large LZA	Clear conditions down to feature of interest associated with threshold accuracy	Over specified geographic area

Table 2-3. GOES-R mission requirements for Aerosol Particle Size.

Name	Geographic Coverage (G, H, C, M)	Vertical Resolution	Horizontal Resolution	Mapping Accuracy	Measurement Range	Measurement Accuracy	Refresh Rate/Coverage Time Option (Mode 3)	Refresh Rate Option (Mode 4)	Vendor Allocated Ground Latency	Product Measurement Precision
------	----------------------------------	---------------------	-----------------------	------------------	-------------------	----------------------	--	------------------------------	---------------------------------	-------------------------------

Aerosol Particle Size	FD	Total Column	2 km	1 km	Fine/Coarse Angstrom exponent range: -1 to +3	Fine/Coarse Angstrom exponent: 0.3 over ocean and land	Full Disk: 15 min	Full Disk: 5 min	Full Disk: 266 sec	0.15
-----------------------	----	--------------	------	------	---	--	-------------------	------------------	--------------------	------

Table 2-4. Product qualifiers for Aerosol Particle Size. LZA=local zenith angle.

Name	User & Priority	Geographic Coverage (G, H, C, M)	Temporal Coverage Qualifiers	Product Extent Qualifier	Cloud Cover Conditions Qualifier	Product Statistics Qualifier
Aerosol Particle Size	GOES-R	C, FD	Daytime	Quantitative out to at least 60 degrees LZA (Threshold) and qualitative at large LZA	Clear conditions down to feature of interest associated with threshold accuracy	Over specified geographic area

## 2.2 Instrument Characteristics

The Advanced Baseline Imager (ABI) on GOES-R will have a total of 16 spectral bands in the visible, near-infrared and infrared spectral regions. The ABI spatial resolution will be 2.0 km for the 1.38- $\mu\text{m}$ , 2.25- $\mu\text{m}$  and ten infrared (IR) spectral bands, and 0.5 km for the 0.64- $\mu\text{m}$  visible band. Spatial resolution of the other bands will be 1.0 km. Table 2-5 lists these and the spectral characteristics of the instrument. ABI will have an on-board calibration of the reflected solar channels and expected to provide an absolute radiometric calibration accuracy of 5.0%, relative (one-sigma) calibration deviations (short-term repeatability) of 0.2%, calibrated radiances that correct for instrument degradation drift in radiance to 0.5% of the radiance. (Additional observations of lunar or stellar sources may be employed by NOAA operationally to attempt to improve long-term radiometric stability of the on-board calibration methodology over the ABI lifetime.) Details on the instrument design, calibration, and additional information on its characteristics are provided elsewhere, and not included in this ATBD. Table 2-5 also indicates which channels are currently used by the algorithm for aerosol retrieval. (Note that channels used in internal tests, for example to detect turbid water, are not indicated in this table, as these tests are not yet implemented.)

Table 2-5. Wavelengths, spatial resolution, and noise characteristics of ABI channels.

<i>Channel ID</i>	<i>Wavelength Microns</i>	<i>Hor. Res.</i>	<i>Upper and lower 50% response points (in microns)</i>	<i>Noise @ Ref.</i>	<i>Max. Level</i>	<i>Used</i>
1	0.47	1km	0.45 $\pm$ 0.01 - 0.49 $\pm$ 0.01	300/1	100 %	✓ (land)

2	0.64	0.5km	0.59±0.01 - 0.69±0.01	300/1	100 %	✓ (land and water)
3	0.865	1km	0.8455±0.01 - 0.8845±0.01	300/1	100 %	✓ (water)
4	1.378	2km	1.3705±0.005 - 1.3855±0.005	300/1	100 %	
5	1.61	1km	1.58±0.01 - 1.64±0.01	300/1	100 %	✓ (water)
6	2.25	2km	2.225±0.01 - 2.275±0.01	300/1	100 %	✓ (land and water)
7	3.90	2km	3.80±0.05 - 4.00±0.05	0.1 K	400 K	
8	6.185	2km	5.77±0.03 - 6.6±0.03	0.1 K	300 K	
9	6.95	2km	6.75±0.03 - 7.15±0.03	0.1 K	300 K	
10	7.34	2km	7.24±0.02 - 7.44±0.02	0.1 K	320 K	
11	8.5	2km	8.3±0.03 - 8.7±0.03	0.1 K	330 K	
12	9.61	2km	9.42±0.02 - 9.8±0.03	0.1 K	300 K	
13	10.35	2km	10.1±0.1 - 10.6±0.1	0.1 K	330 K	
14	11.2	2km	10.8±0.1 - 11.6±0.1	0.1 K	330 K	
15	12.3	2km	11.8±0.1 - 12.8±0.1	0.1 K	330 K	
16	13.3	2km	13.0±0.06 - 13.6±0.06	0.3 K	305 K	

Table 2-5 also lists the expected noise characteristics of the ABI in the various channels as given in the MRD. A detailed analysis of the effect of instrument noise on the aerosol retrieval using various noise models is provided in Appendix A1.

### 3 ALGORITHM DESCRIPTION

This section describes the algorithm at the current level of maturity.

### 3.1 Algorithm Overview

The capabilities offered by ABI onboard GOES-R are similar to the multispectral observations currently provided by the Moderate Resolution Imaging Spectroradiometer (MODIS) flown on the NASA Earth Observing System (EOS) satellites Terra and Aqua, and to those that will be available from the Joint Polar Satellite System (JPSS) (formerly NPOESS) Visible Infrared Imaging Radiometer Suite (VIIRS). The ABI aerosol algorithm therefore heavily builds on the heritage of and the lessons learned from the MODIS [Remer et al., 2005, 2006; Levy et al., 2007] and VIIRS [Vermote et al., 2006] aerosol algorithms. Separate algorithms are developed for retrieval over land and ocean due to the distinct surface properties and aerosol types.

Due to varying contribution of the surface to the satellite-observed reflectance and large variation in aerosol optical properties, aerosol retrieval is a complex problem. However, it is expected that observations of TOA reflectance at more than one wavelength can provide more information, and thus can reduce the number of unknowns and provide better constraints [King et al., 1978; Tanre et al., 1997]. In the ABI algorithm, this is achieved by the selection of appropriate aerosol models and by calculating and estimating the surface reflectance over ocean and land, respectively. Over land, surface reflectance is estimated by the dark-dense vegetation approach, in which the surface reflectance in the visible spectrum is obtained from the shortwave infrared (SWIR) reflectance from pre-determined spectral relationships between these surface reflectances. To aid rapid retrieval of aerosol, look-up tables of spectral atmospheric (aerosols plus molecules) optical functions (reflectance, transmittances and spherical albedo) are pre-calculated for a wide range of geometries and typical aerosol models at standard surface pressure. Surface and atmospheric reflections are coupled following the VIIRS approach [Vermote et al., 2006]. The resulting calculated spectral TOA reflectances are compared with observations to determine the optimal solution.

The geostationary platform offers observations at near constant local zenith angles, along with multiple looks of the same location in time over the course of a day. This feature has been exploited in remote sensing of aerosol and surface albedo in several algorithms [e.g., Knapp et al., 2005; Pinty et al., 2000; Thomas et al., 2007; Govaerts et al., 2010]. Many of these algorithms assume either that the aerosol amount is constant during the course of the day [Pinty et al., 2000], or require a priori information about the surface reflection properties [Thomas et al., 2007]. An algorithm that does not use many of these assumptions, and may replace the current ABI algorithm for retrieval over land, has been developed at the University of Maryland Baltimore County. This algorithm, which retrieves aerosol optical depth and surface bidirectional reflectance simultaneously even over bright surfaces, is briefly described in Section 6.3.1.

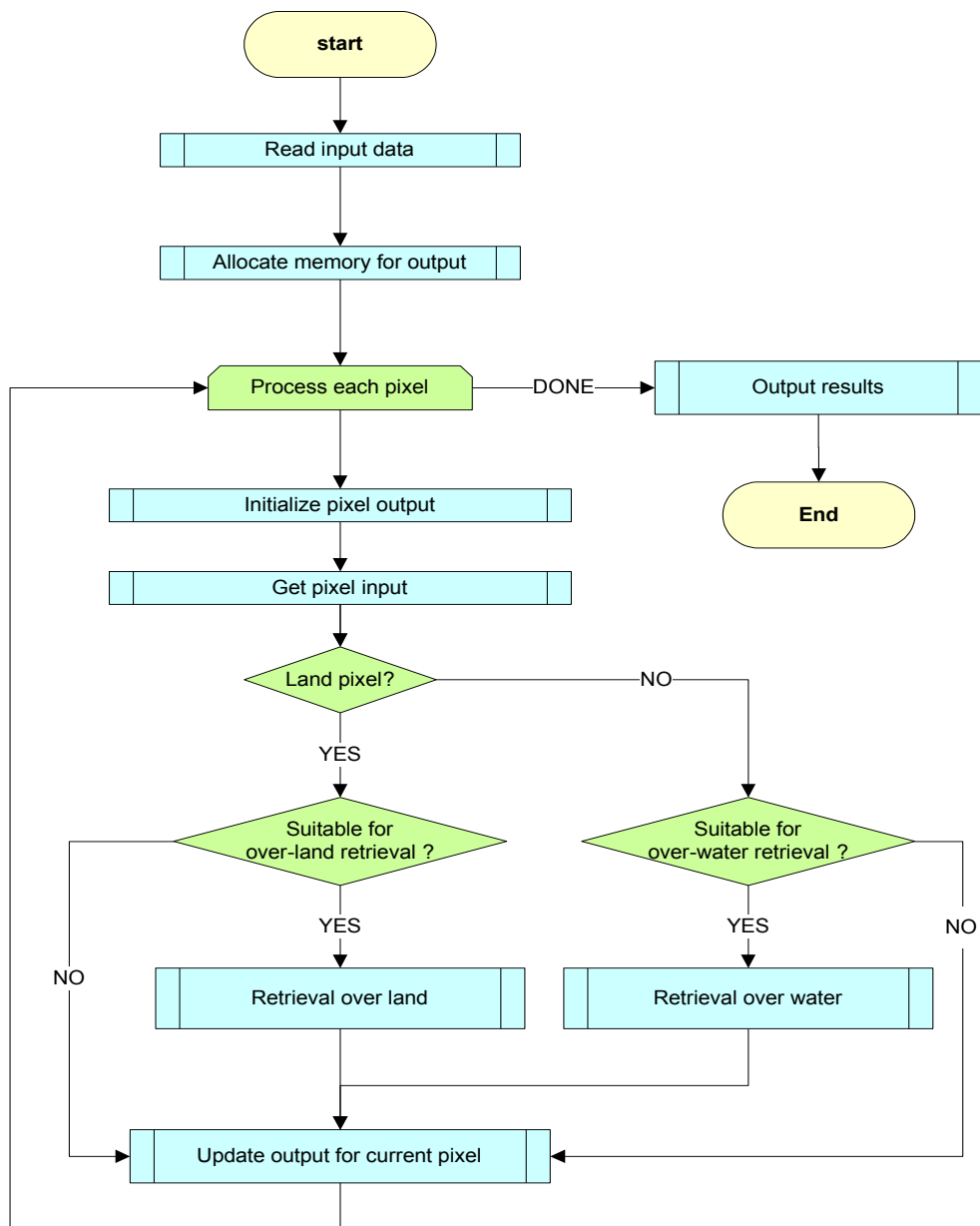


Figure 3-1. High level flowchart of the AOD retrieval illustrating the main processing sections.

In principle, the multiple look with varying solar angles of a scene at a fixed local zenith angle from the geostationary platform may allow to partially “map out” the phase function. However, this would require the assumption of an unchanging aerosol type and amount. In addition, it would require very accurate navigation, and very accurate knowledge of the surface bidirectional reflectance. It is doubtful that these requirements can be satisfied at this time, so the current algorithm does not build on this theoretical

possibility. Instead, the extensively tested and proven multi-channel algorithms developed for MODIS and VIIRS are used as heritage.

### 3.2 Processing Outline

The processing outline of the AOD retrieval algorithm is summarized in Figure 3-1, which shows the major components of the algorithm. These components are: 1) Prepare input data for each 2 km “pixel”; 2) Determine retrieval eligibility and relevant algorithm; 3) Perform aerosol retrieval; 4) Evaluate the retrieval quality and output the result.

### 3.3 Algorithm Input

This section describes the input needed to process the aerosol retrieval.

#### 3.3.1 Primary sensor data

Table 3-1 lists the primary sensor data used by the aerosol retrieval, including calibrated and geolocated level 1b reflectance (channels 1, 2, 6 for land, and channels 2, 3, 5, 6 for ocean) from ABI observations, geolocation information, and ABI sensor quality flags.

Table 3-1. ABI primary sensor input data.

<b>Name</b>	<b>Type</b>	<b>Description</b>	<b>Dimension</b>
Ch1 reflectance	Input	Calibrated ABI channel 1 reflectance	grid (xsize, ysize)
Ch2 reflectance	Input	Calibrated ABI channel 2 reflectance	grid (xsize, ysize)
Ch3 reflectance	Input	Calibrated ABI channel 3 reflectance	grid (xsize, ysize)
Ch5 reflectance	Input	Calibrated ABI channel 5 reflectance	grid (xsize, ysize)
Ch6 reflectance	Input	Calibrated ABI channel 6 reflectance	grid (xsize, ysize)
Latitude	Input	Pixel latitude	grid (xsize, ysize)
Longitude	Input	Pixel longitude	grid (xsize, ysize)
Solar geometry	Input	ABI solar zenith and azimuth angles	grid (xsize, ysize)
View geometry	Input	ABI local zenith and azimuth angles	grid (xsize, ysize)
QC flags	Input	ABI quality control flags with input data	grid (xsize, ysize)

The algorithm assumes the reflectance is calculated from the calibrated radiance by dividing  $\pi$  times the radiance by the product of the cosine of solar angle and the extraterrestrial solar irradiance at the actual sun-earth distance.

The inputs to the algorithm are the averages of the clear Level 1b reflectances for the 2-km grid. Note, however, that implementation and testing of internal tests to eliminate cloud, snow/ice contamination, identification of turbid water, etc. may require the use of the 1-km Level 1b reflectances directly. In this case, the algorithm needs to be updated such that averaging of qualified reflectances for the 2-km grid is done inside the aerosol retrieval algorithm.

The dimensions “xsize” and “ysize” correspond to the size of the grid in the longitude and latitude directions, respectively. Their values are determined in the framework outside of the aerosol algorithm.

### 3.3.2 Ancillary data

The algorithm requires three types of ancillary data: 1) ABI level 2 products (Table 3-2); 2) Global Forecast System (GFS) model data (Table 3-3); and 3) Non-ABI static data (Table 3-4).

ABI cloud and snow/ice masks are needed to identify clear-sky snow/ice-free pixels for aerosol retrievals. When the ABI snow/ice mask is not available, the Interactive Multisensor Snow and Ice Mapping System (IMS) is used. Land/sea mask is used to select the appropriate (land or ocean) algorithm for retrieval. In case ABI total precipitable water (TPW) and ozone data are missing or not valid, Global Forecast System (GFS) data are used instead. GFS model surface wind speed and direction over ocean is required for ocean surface reflectance calculation. Lower resolution model surface pressure is corrected to pixel-level pressure as:

$$P_{pixel} = P_{model} * \frac{e^{-H_{digital}/8.24}}{e^{-H_{model}/8.24}} \quad (3.3.1)$$

where  $P_{pixel}$  and  $P_{model}$  are actual pixel-level and model surface pressures ;  $H_{digital}$  and  $H_{model}$  are high-resolution digital and low-resolution model surface elevations, respectively. A constant scale height of 8.24 km (adopted from the VIIRS ATBD) is assumed in this pressure correction.

Table 3-2. ABI dynamic ancillary input data

Name	Type	Description	Dimension
Cloud mask	input	ABI level 2 cloud mask data	grid (xsize, ysize)
Snow/Ice mask	input	ABI level 2 Snow/Ice mask data	grid (xsize, ysize)
TPW	input	ABI level 2 total precipitable water	grid (xsize, ysize)

Ozone	input	ABI level 2 ozone data	grid(xsize, ysize)
-------	-------	------------------------	--------------------

Table 3-3. Non-ABI dynamic ancillary input data

<b>Name</b>	<b>Type</b>	<b>Description</b>	<b>Dimension</b>
Model ocean surface wind speed & direction	input	Global Forecast System (GFS) data	grid (xsize, ysize)
Model surface pressure	input	Global Forecast System (GFS) data	grid (xsize, ysize)
Model surface height	input	Global Forecast System (GFS) data	grid (xsize, ysize)
Model total precipitable water	input	Global Forecast System (GFS) data	grid (xsize, ysize)
Model total ozone	input	Global Forecast System (GFS) data	grid (xsize, ysize)
Model snow/ice mask	input	Ice Mapping System (IMS) data	grid (xsize, ysize)

The spatial and temporal interpolation of GFS model data is a common procedure to many ABI algorithms, and is implemented at the framework level outside of the ABI aerosol algorithm.

Table 3-4. Non-ABI Static ancillary input data

<b>Name</b>	<b>Type</b>	<b>Description</b>	<b>Dimension</b>
Land/Sea Mask	input	Global land/water mask	1 km
Surface elevation	input	Global digital elevation data	1 km

### 3.3.3 Derived data

The derived data (Table 3-5) include pre-calculated LUTs and aerosol normalized and mass extinction coefficients.

There are two LUTs. The atmospheric LUT includes atmospheric reflectance, transmittance and spherical albedo in the ABI channels used for retrievals (three channels for land: 0.47, 0.64 and 2.25 $\mu$ m; four channels for ocean: 0.64, 0.86, 1.61 and 2.25  $\mu$ m). The sunglint LUT contains water direct-hemispheric reflectance and spherical albedo. Details of the LUTs are presented in Section 3.4.5.

Aerosol normalized extinction coefficients (ratio of the aerosol optical depth in the ABI channels to that at 0.55  $\mu$ m) are used for calculating AODs in five ABI channels (0.47, 0.64, 0.86, 1.61, and 2.25  $\mu$ m) once AOD at 0.55  $\mu$ m ( $\tau_{0.55}$ ) and aerosol model are determined. Compared to the ocean aerosol models, land aerosol models are assumed to

be dynamic, i.e., microphysical and optical properties vary with aerosol loading. As a result, extinction coefficients of land aerosol models are functions of  $\tau_{0.55}$ .

Aerosol mass extinction coefficients are needed to calculate suspended matter mass loading based on the retrieved  $\tau_{0.55}$ . These coefficients are adopted from the MODIS Collection 5 algorithm since the same candidate aerosol models are used in the ABI retrieval. Similar to the normalized extinction coefficients, mass extinction of land aerosol models depends on the aerosol loading and it as a function of  $\tau_{0.55}$ . More information about aerosol column mass calculation is provided in section 3.4.4.

Table 3-5. ABI derived input data

Name	Type	Description	Dimension
Atmospheric LUT	Input	atmospheric reflectance $\rho_{R+A}$ as function of aerosol model, aerosol optical depth, ABI channel and scattering angle	(4, 20, 3, 7506)* (9, 20, 4, 7506)** (Nmodel, Ntau, Nchn, Nscaang)
		atmospheric transmittance $T_{R+A}$ as function of aerosol model, aerosol optical depth, ABI channel and zenith angle	(4, 20, 3, 21)* (9, 20, 4, 21)** (Nmodel, Ntau, Nchn, Nzen)
		atmospheric spherical albedo $S_{R+A}$ as function of aerosol model, aerosol optical depth, and ABI channel	(4, 20, 3)* (9, 20, 4)** (Nmodel, Ntau, Nchn)
Sunglint LUT	Input	water sunglint direct-hemispheric reflectance as function of aerosol model, aerosol optical depth, ABI channel, solar zenith angle, local zenith angle, relative azimuth angle, and surface wind speed	(9, 20, 4, 21, 21, 40, 9) (Nmodel, Ntau, Nchn, Nsolzen, Nsatzen, Nwndspd)
		water spherical albedo as function of ABI channel and wind speed	(4, 9) (Nchn, Nwndspd)
Aerosol Normalized Extinction Coefficients	Input	normalized aerosol extinction coefficient as function of aerosol model, aerosol optical depth (land only) and ABI channel	(4, 20, 5)* (Nmodel, Ntau, Nchn) (9 x 5)** (Nmodel, Nchn)
Aerosol Mass Extinction Coefficients	Input	Mass extinction coefficients for each aerosol model	(4, 20) * (Nmodel, Ntau) (9, 2) * (Nmodel, Npar)

\*: over land

\*\* : over ocean.

## 3.4 Theoretical Description

This section describes the physics key to the aerosol retrieval over ocean and land. Description of the mathematics used by the retrieval, including all simplifications, approximations, and numerical methods, as well as the algorithm outputs are also presented.

The feasibility of aerosol retrieval from satellite-observed radiances is based on the fact that these radiances are affected by the physical and chemical properties of aerosols [e.g., King et al., 1978; Kaufman et al., 1990]. The wavelength bands of satellite sensors are picked to minimize gas and other contaminants to the aerosol signal. Because the ABI channels closely match those of MODIS and VIIRS, and because the MODIS algorithm, and to a certain degree the VIIRS algorithm, has already been proven to work well, the ABI algorithm is designed to closely follow the approaches used with these sensors [Remer et al., 2005, 2006; Levy et al., 2007; Vermote et al., 2006]. Just like the MODIS and VIIRS algorithms, the ABI algorithm retrieves the aerosol optical depth and the most likely aerosol model simultaneously from radiances observed in the visible and near infrared channels. The assumption is that the contribution of the ocean surface can be accurately computed, and the land surface reflectance can be estimated. Therefore there are two separate algorithms: one for ocean and one for land.

Aerosol retrievals are also affected by the presence of various “contaminants” in the pixel that can degrade the quality of aerosol retrievals. These include snow for land, and glint and turbid water for ocean [e.g., Remer et al., 2005, 2006].

### 3.4.1 Physical and mathematical description for aerosol optical depth retrieval over ocean

#### 3.4.1.1 Strategy

The algorithm for aerosol retrieval over ocean is based on the VIIRS algorithm [Vermote et al., 2006]; however, the aerosol models used by the algorithm are from the MODIS Collection 5 algorithm [Remer et al., 2005, 2006; Levy et al., 2007]. ABI channels 2, 3, 5 and 6, for which surface reflection can be estimated without information on ocean color, are used [Vermote et al., 2006]. Thus, for example, ABI channel 1 (0.47 $\mu$ m) is not included due to the large uncertainty in water leaving radiance.

It is assumed that the surface reflectance of water can be modeled with sufficient accuracy as shown by Cox and Munk [1954]. Therefore, the essence of the multi-channel aerosol algorithm over water is the simultaneous retrieval of optical depth and aerosol model by matching calculated and observed TOA reflectances in selected ABI channels. The contribution of aerosol to the TOA reflectance is approximated by a linear combination of two aerosol modes corresponding to a fine and a coarse mode of the size distribution with a fine mode weight [e.g. Tanre et al., 1997]. Since an exact match of TOA reflectance in all selected channels is nearly impossible, the algorithm uses ABI

channel 3 (0.86  $\mu\text{m}$ ) as the principal channel, where the aerosol optical depth at 550 nm ( $\tau_{550}$ ) and fine-mode weight ( $\eta$ ) retrieval is performed to match the observed TOA reflectance. The 0.86- $\mu\text{m}$  channel is chosen because of its negligible underwater reflectance, while the contributions from the fine and coarse aerosol modes are still significant. Residuals - sum of squared differences of calculated and observed reflectances - in other channels are calculated and used to measure the degree of match. The minimum residual is considered the ‘best’ match. The process of checking for minimum residual is repeated for the various combinations of AOD and  $\eta$  and the solution that gives the minimum residual is chosen for the retrieval of  $\tau_{550}$  and  $\eta$ . AOD at other wavelengths is determined by using the spectral dependence of aerosol optical properties unique to that aerosol model, which is included in the pre-calculated LUT.

Surface reflection, including contributions from water leaving radiation, whitecaps and sun glint direct reflection (Section 3.4.1.5), and the atmosphere-surface coupling (Section 3.4.1.3) are explicitly calculated in the algorithm. Dependence of ocean surface reflectance on surface wind is incorporated, which can be significant at mid-high latitudes where relatively large wind speed dominates. This is in contrast to the MODIS Collection 5 aerosol algorithm that assumes a constant wind speed of 6 m/s [Remer et al., 2005]. (The MODIS Collection 6 algorithm will also include a wind-speed dependent ocean reflectance (Levy, 2012, personal communications.))

Internal tests for screening out glint and turbid water are discussed in Appendix C. Note that at present tests for turbid water are not performed.

### 3.4.1.2 Aerosol models

Over ocean, the aerosol model is represented by a combination of fine-mode and coarse mode aerosols. The four fine and five coarse modes adopted from MODIS [Remer et al., 2005, 2006; Levy et al., 2007] are summarized in Table 3-6. The size distribution for these aerosols is assumed to be log-normal:

$$\frac{dN(r)}{d \ln r} = \sum_{i=1}^2 \frac{N_0}{\sqrt{2\pi} \ln \sigma_{g,i}} \exp \left[ -\frac{(\ln r - \ln r_{g,i})^2}{2(\ln \sigma_{g,i})^2} \right], \quad (3.4.1)$$

where  $N(r)$  is the number density corresponding to particles of radii within ( $r, r+dr$ ),  $r_{g,i}$  is the median radius, and  $\sigma_{g,i}$  is the associated standard deviation. Microphysical properties of the aerosol models are listed in Table 3-6. These are derived from the prescribed size distribution and refractive index from MODIS aerosol models [Remer, et al, 2006]. The aerosol effective radius is an area weighted mean radius and defined as

$$r_{\text{eff}} = \frac{\int_0^{\infty} r^3 N(r) dr}{\int_0^{\infty} r^2 N(r) dr}, \text{ where } r \text{ is the particle radius in micrometers, and } N(r) \text{ the particle size}$$

distribution (number of particles per  $\text{cm}^2$  with radius in the range  $r$  and  $r+dr$ ). For calculation of aerosol optical properties, integration of aerosol size distribution (Eq. 3.4.1) is performed within the radius range of 0.05 to 15.0  $\mu\text{m}$  following the Mie calculation in the 6S radiative transfer model (RTM) [Kotchenova et al., 2006; 2007]

Table 3-6. Microphysical properties of ocean aerosols (Fine modes: F1-F4; Coarse modes: C1-C5) used in the ABI algorithm (refractive indices, number median ( $r_g$ ) and standard deviation ( $\sigma_g$ ), and effective radius ( $r_{eff}$ ))

Aerosol model	Refractive index Wavelength ( $\mu\text{m}$ )						$r_g$	$\sigma_g$	$r_{eff}$
	0.47	0.64	0.86	1.38	1.61	2.26			
F1	1.45-0.0035i	1.45-0.0035i	1.45-0.0035i	1.44-0.005i	1.43-0.01i	1.40-0.005i	0.07	1.49182	0.10
F2	1.45-0.0035i	1.45-0.0035i	1.45-0.0035i	1.45-0.005i	1.43-0.01i	1.40-0.0050i	0.06	1.82212	0.15
F3	1.40-0.002i	1.40-0.002i	1.40-0.002i	1.40-0.0035i	1.39-0.005i	1.36-0.003i	0.08	1.82212	0.20
F4	1.40-0.002i	1.40-0.002i	1.40-0.002i	1.40-0.0035i	1.39-0.005i	1.36-0.003i	0.10	1.82212	0.25
C1	1.35-0.001i	1.35-0.001i	1.35-0.001i	1.35-0.001i	1.35-0.001i	1.35-0.001i	0.40	1.82212	0.98
C2	1.35-0.001i	1.35-0.001i	1.35-0.001i	1.35-0.001i	1.35-0.001i	1.35-0.001i	0.60	1.82212	1.48
C3	1.35-0.001i	1.35-0.001i	1.35-0.001i	1.35-0.001i	1.35-0.001i	1.35-0.001i	0.80	1.82212	1.98
C4	1.53-0.003i	1.53-0.0i	1.53-0.0i	1.46-0.0i	1.46-0.001i	1.46-0.0i	0.60	1.82212	1.48
C5	1.53-0.003i	1.53-0.0i	1.53-0.0i	1.46-0.0i	1.46-0.001i	1.46-0.0i	0.50	2.2255	2.50

### 3.4.1.3 Calculation of TOA reflectance

Calculation of TOA reflectance follows that in the VIIRS ATBD [Vermote et al., 2006], which itself is based on the formulation in the Second Simulation of the Satellite Signal, 6S radiative transfer model [Vermote et al., 1997, Kotchenova et al., 2006; 2007] .

According to this formulation, the spectral reflectance at the satellite level ( $\rho_{toa}$ ) is the combination of two components  $\rho_{atm}$  and  $\rho_{surf}$  originating, respectively, in the atmosphere and at the surface. The atmospheric contribution is due to reflection, scattering by molecules and aerosols and absorption by aerosols and gases. The surface contribution comes from the multiple reflection of radiation between the surface and the

atmosphere that is subsequently attenuated by the atmosphere as it travels upward to the satellite. The atmosphere contribution is:

$$\rho_{toa} = \rho_{atm} + \rho_{surf} . \quad (3.4.2)$$

To facilitate the calculation of atmospheric reflection with varying gaseous amount and surface pressure, gas absorption, aerosol and Rayleigh scattering are decoupled in a layered model atmosphere. In this model, radiation produced in a layer with molecular scattering, aerosol extinction, and water vapor absorption is attenuated by absorption in the top layer by ozone, O<sub>2</sub>, CO<sub>2</sub>, N<sub>2</sub>O, and CH<sub>4</sub>. Ignoring the interaction between aerosol and Rayleigh scattering, the atmospheric contribution to TOA reflectance is computed as:

$$\rho_{atm} = T^{O_3} T^{og} \left[ (\rho_{R+A} - \rho_R(P_0)) T^{\frac{1}{2}H_2O} + \rho_R(P) \right], \quad (3.4.3)$$

where,  $T^{O_3}$  is the transmittance from ozone absorption;  $T^{og}$  is the transmittance from gas absorption other than ozone and water vapor;  $T^{\frac{1}{2}H_2O}$  is the transmittance from half-column water vapor absorption;  $\rho_{R+A}$  is the path reflectance by aerosols and molecules at standard surface pressure;  $\rho_R(P_0)$  is the Rayleigh reflectance from molecular scattering at standard surface pressure  $P_0$ ;  $\rho_R(P)$  is the Rayleigh reflectance from molecular scattering at the actual surface pressure  $P$ . Here,  $\rho_{R+A}$  is pre-calculated and stored in the atmospheric LUT (see section 3.4.5.1), while transmittances from gas absorption  $T$  and Rayleigh reflectance  $\rho_R$  are analytically modeled (see sections 3.4.6 and 3.4.7). Rayleigh reflectance  $\rho_R$  is calculated at the given local surface pressure and at standard pressure, respectively (see section 3.4.7). Note that the channel index has been dropped from the notation for convenience.

The reflectance of ocean surface is modeled as the sum of bi-directional sunglint reflection, Lambertian underwater reflection and whitecap reflection (see section 3.4.1.5). Interaction between the atmosphere and the surface reflection is decomposed as the sum of six terms in Eq. (3.4.4) corresponding to the contributions from (1) Lambertian reflection from underwater and whitecaps; (2) directional sunglint reflection without atmospheric scattering; (3) diffuse downward radiation reflected by the surface and transmitted to the sensor without scattering; (4) direct downward radiation reflected by surface and scattered back to the sensor; (5) diffuse downward radiation reflected by surface and scattered back to the sensor; and (6) radiation reflected by the surface more than once. For efficient calculations, a look-up table (see section 3.4.5.2) for the necessary terms (e.g.,  $\overline{\rho_{sgt}}$ ,  $\overline{\rho'_{sgt}}$  and  $\overline{\rho_{sgt}}$ ) is generated using the 6S radiative transfer model [Vermote et al., 1997]. The diffuse transmittance is calculated by subtracting the direct transmittance from the total transmittance. All terms are calculated for the central wavelength of the ABI channels.

$$\rho_{surf} = T^{O_3} T^{og} T^{H_2O} \left[ T_{R+A}^\downarrow T_{R+A}^\uparrow \frac{\rho_{w+wc}}{1 - S_{R+A} \rho_{w+wc}} + t_{R+A}^{dir\downarrow} t_{R+A}^{dir\uparrow} \rho_{sgt} + t_{R+A}^{dif\downarrow} t_{R+A}^{dif\uparrow} \overline{\rho_{sgt}} \right. \\ \left. + t_{R+A}^{dir\downarrow} t_{R+A}^{dif\uparrow} \overline{\rho_{sgt}'} + t_{R+A}^{dif\downarrow} t_{R+A}^{dif\uparrow} \overline{\overline{\rho_{sgt}}} + T_{R+A}^\downarrow T_{R+A}^\uparrow \frac{S_{R+A} (\overline{\rho_{sgt}})^2}{1 - S_{R+A} \rho_{sgt}} \right], \quad (3.4.4)$$

$$t_{R+A}^{dir\downarrow} = e^{-\tau_{R+A}/\cos(\theta_s)}, \quad (3.4.5)$$

$$t_{R+A}^{dir\uparrow} = e^{-\tau_{R+A}/\cos(\theta_v)}, \quad (3.4.6)$$

$$t_{R+A}^{dif\downarrow} = T_{R+A}^\downarrow - t_{R+A}^{dir\downarrow}, \quad (3.4.7)$$

$$t_{R+A}^{dif\uparrow} = T_{R+A}^\uparrow - t_{R+A}^{dir\uparrow}, \quad (3.4.8)$$

$$\tau_{R+A} = \tau_A + \tau_R(P), \quad (3.4.9)$$

where,  $T_{R+A}^\downarrow$  is the total (direct and diffuse) downward atmospheric transmission;  $T_{R+A}^\uparrow$  is the total (direct and diffuse) upward atmospheric transmission;  $t_{R+A}^{dir\downarrow}$  is the direct downward atmospheric transmission;  $t_{R+A}^{dir\uparrow}$  is the direct upward atmospheric transmission;  $t_{R+A}^{dif\downarrow}$  is the diffuse downward atmospheric transmission;  $t_{R+A}^{dif\uparrow}$  is the diffuse upward atmospheric transmission;  $S_{R+A}$  is the atmospheric spherical albedo;  $\rho_{w+wc}$  is the surface Lambertian reflectance from underwater and whitecaps;  $\rho_{sgt}$  is the sunglint directional reflectance;  $\overline{\rho_{sgt}}$  is the normalized integral of the downward irradiance reflectance by the sunglint directional reflectance;  $\overline{\overline{\rho_{sgt}}}$  is the reciprocal quantity of  $\overline{\rho_g}$  for the upward coupling;  $\overline{\rho_{sgt}'}$  is approximated as the sunglint spherical albedo;  $\theta_s$  is the solar zenith angle;  $\theta_v$  is the local zenith angle;  $\tau_{R+A}$  is the total column optical thickness of molecules and aerosols;  $\tau_R(P)$  is the Rayleigh optical depth at local actual pressure  $P$ , and  $\tau_A$  is the total column aerosol optical depth. Note that  $\tau_R(P)$  and  $\tau_A$  should use the values for the specific wavelength.  $T_{R+A}^\downarrow$ ,  $T_{R+A}^\uparrow$ , and  $S_{R+A}$  are obtained from the atmospheric look-up table, and require adjustment for actual surface pressure following Eq. (3.4.35) and Eq. (3.4.36) in Section 3.4.6.  $\overline{\rho_{sgt}}$ ,  $\overline{\rho_{sgt}'}$ , and  $\overline{\overline{\rho_{sgt}}}$  are obtained from the ocean surface reflectance look-up table (see Appendix B).

#### 3.4.1.4 Aerosol retrieval algorithm over ocean

The retrieval algorithm assumes that aerosol reflectance  $\rho_\lambda'$  for a given  $\tau_{550}$  can be approximated with a linear combination of contributions from one fine ( $\rho_\lambda^f$ ) and one coarse ( $\rho_\lambda^c$ ) aerosol modes with a proper fine-mode weight  $\eta$  [Wang and Gordon, 1994; Kaufman and Tanre, 1996],

$$\rho_{\lambda}^i(\tau_{550}) = \eta \rho_{\lambda}^f(\tau_{550}) + (1 - \eta) \rho_{\lambda}^c(\tau_{550}). \quad (3.4.10)$$

In the retrieval, the algorithm searches for the pair of fine and coarse modes, along with the fine mode weight ( $\eta$ ) and corresponding  $\tau_{550}$  that give the best match of TOA reflectance in multiple ABI channels between calculations and observations.

Specifically, there are two levels of iteration and selection involved. The first iteration is on the combination of candidate fine and coarse modes, which are predetermined and built into the lookup table. In the current algorithm, there are four (fine mode) by five (coarse model) combination pairs.

The second iteration (searching for  $\eta$  for any given pair of fine and coarse aerosol modes) uses bisection (interval halving), which repeatedly divides the fine-mode weight range in half and searches for the subinterval that includes the ‘best’ fit  $\eta$  with minimum residual. Ranges of the fine mode weight, starting with the full range of 0-1, are repeatedly bisected, AODs are retrieved and residuals are calculated. Altogether ten bisection steps are performed, regardless of measurement uncertainty. In each step, the interval that results the smallest residual in the previous step is selected for the next bisection. The process starts with dividing the range of  $\eta$  between 0 and 1 into four equal subintervals with ranges of 0.00-0.25, 0.25-0.50, 0.50-0.75, and 0.75-1.00. AODs are retrieved for the five boundary values of  $\eta$  (0, 0.25, 0.5, 0.75 and 1), and residuals are calculated. The smallest residual is identified among the five residuals and the subinterval containing the smallest residual is selected for further processing (bisection). So, for example, if the residuals corresponding to the five starting values of  $\eta$  are  $R_{0.0}$ ,  $R_{0.25}$ ,  $R_{0.5}$ ,  $R_{0.75}$  and  $R_{1.0}$ , and if  $R_{0.0}$  (or  $R_{0.25}$ ) is the smallest residual then the two intervals 0.00-0.25 and 0.25-0.50 are bisected leading to another five values of  $\eta$  (0.0, 0.125, 0.25, 0.375, 0.5). AODs and residuals are calculated for these  $\eta$  values. (Note that retrievals are already performed for the  $\eta$  values of 0, 0.25 and 0.5 in the previous step, so in reality they need to be done only for the  $\eta$  values of 0.125 and 0.375.) If  $R_{0.5}$  is the smallest then the middle two subintervals (0.25-0.5 and 0.5-0.75) are used. If  $R_{0.75}$  (or  $R_{1.0}$ ) is the smallest the upper two subintervals (0.5-0.75 and 0.75-1.0) are used. The process is repeated ten times and usually reaches 0.1% accuracy, and the  $\eta$  (and AODs) corresponding to the smallest residual is selected as the solution. If two or more residuals are identical within machine precision, the first one in the sequence is selected. The determination of  $\tau_{550}$  for any specific aerosol model (combination of fine and coarse modes with known  $\eta$ ) is performed by matching the calculated TOA reflectance at 0.86  $\mu\text{m}$  with the measurement; and extrapolation is allowed and flagged for  $\tau_{550} > 5$  or  $\tau_{550} < 0$  when  $\tau_{550}$  is outside of the tabulated AOD550 range in LUT. The best match is determined by comparing the residuals that are calculated as the sum of squared differences between calculated ( $\rho_{\lambda}^{cal}$ ) and observed ( $\rho_{\lambda}^{obs}$ ) TOA reflectances in the ABI channels 2, 5 and 6 (0.64, 1.61, and 2.25  $\mu\text{m}$ ):

$$residual = \sum_{i=1}^n (\rho_{\lambda}^{cal} - \rho_{\lambda}^{obs})^2, \quad (3.4.11)$$

where  $n = 3$ , the number of channels used for calculating the residual, and  $\rho_{\lambda}^{cal}$  corresponds to  $\rho_{toa}$  in Eq.(3.4.2)

Once the final solution of aerosol model and corresponding  $\tau_{550}$  are determined, AODs in five ABI channels (channels 1,2,3,5, and 6) are calculated by the unique spectral dependence of the aerosol extinction coefficient for the retrieved combination of fine and coarse mode aerosol models and fine mode weight  $\eta$ . That is, the optical depth at wavelength  $\lambda$  is calculated as  $\tau_{\lambda, fine/coarse} = n_{ext, \lambda, fine/coarse} \times \tau_{550}$  for the retrieved fine and coarse mode aerosol models, respectively, where  $n_{ext, \lambda}$  is the normalized extinction coefficient at wavelength  $\lambda$  included in the LUT for each fine and coarse mode aerosol model. The final AOD at wavelength  $\lambda$  is calculated as  $\tau_{\lambda} = \tau_{\lambda, fine} \times \eta + \tau_{\lambda, coarse} + (1 - \eta)$ .

### 3.4.1.5 Calculation of ocean surface reflectance

As discussed in Section 3.4.1.3, the reflectance of ocean surface is modeled as the sum of bi-directional sun-glint, Lambertian dark underwater and whitecap reflections. The calculation of each of these reflection terms contains wavelength-specific coefficients. These coefficients are derived for the visible-to-near-infrared ABI channels using the 6S RTM, where the sunlint bi-directional reflectance distribution function (BRDF) is calculated from the Cox and Munk model [Cox and Munk, 1954].

Underwater and whitecap reflectance  $\rho_{w+wc}$  is calculated as

$$\rho_{w+wc} = \rho_w + \rho_{wc}, \quad (3.4.12)$$

$$\rho_{wc} = \rho_{wc-eff} \cdot 2.95 \times 10^{-6} [ws]^{3.52} \quad (3.4.13)$$

where  $\rho_w$  and  $\rho_{wc}$  are reflectances from underwater and whitecap respectively,  $ws$  is the wind speed in  $m s^{-1}$ .  $\rho_{wc}$  is the product of an effective reflectance  $\rho_{wc-eff}$  and whitecap coverage [Koepke, 1984]. For simplicity, chlorophyll concentration is fixed ( $0.4 mg m^{-3}$ ). The dependence of underwater reflectance on wind speed is weak, and the wind-speed dependence of whitecap reflectance is accounted for by the wind-speed dependent whitecap coverage in Eq. (3.4.13). Table 3-7 contains the channel-dependent constants for  $\rho_w$  and  $\rho_{wc-eff}$ .

Table 3-7. Whitecap effective reflectance and underwater reflectance

ABI Channel (wavelength: $\mu m$ )	$\rho_{wc-eff}$	$\rho_w$
2 (0.64)	0.2200	0.0126
3 (0.86)	0.1983	0.0
5 (1.61)	0.1195	0.0

6 (2.25)	0.0475	0.0
----------	--------	-----

Calculation of sunglint directional reflectance  $\rho_{sgt}$  is adopted from the corresponding 6S subroutine [Vermote et al., 1997; Cox and Munk, 1954]. It requires inputs of wind speed  $w_s$  (in  $\text{m s}^{-1}$ ), index of refraction ( $n_r, n_i$ ) and extinction coefficient of the sea water, solar zenith angle  $\theta_s$ , local zenith angle  $\theta_v$ , and sun, local and wind azimuth angles  $\phi_s, \phi_v, \phi_w$  (clockwise from local North). The index of refraction and extinction coefficient (Table 3-8) of the sea water are calculated from the 6S RTM assuming a constant salinity of 34.3 ppt. Details of the sunglint directional reflectance calculation are given in Appendix B.

Table 3-8. Seawater index of refraction and extinction coefficient for ABI bands

ABI Channel (wavelength: $\mu\text{m}$ )	Nr	Ni
2 (0.64)	1.3374833	0.0
3 (0.86)	1.3343327	0.0000004
5 (1.61)	1.3227115	0.0000872
6 (2.25)	1.2985789	0.0004232

### 3.4.1.6 Sensitivity study

The quality of aerosol retrieval can be strongly affected by the uncertainties in the TOA radiances (for example, due to calibration, cross talk, polarization sensitivity, etc.). In multi-channel aerosol retrievals, estimation of these effects is not straightforward owing to the complex interdependencies of channel radiances and assumptions. As part of algorithm testing, numerical tests were designed to investigate the sensitivity of aerosol retrieval to uncertainties in ABI radiances.

For these tests, TOA ABI radiances are simulated by the 6S RTM for a wide range of geometries and aerosol conditions. Table 3-9 lists these varying parameters as inputs to the simulations. A constant water vapor (2 cm) and ozone content (380 Dobson units), and surface wind condition (6 m/s, westerly) is assumed in the simulation (and in the subsequent inversion). Among the 840,000 cases resulting from the combinations of input values listed in Table 3-9, there are 423,640 unique tests which are outside of the sunglint area (glint angle  $\theta_g > 40^\circ, \theta_g = \cos^{-1}((\cos\theta_s \cos\theta_v) - (\sin\theta_s \sin\theta_v \cos\phi))$ , where  $\theta_s, \theta_v$ , and  $\phi$  are the solar zenith, the local zenith and the relative azimuth angles) and used for the following evaluation.

Table 3-9. Geometry and aerosol conditions covered by the sensitivity tests

Parameters	Dimension	Values
cosine of solar zenith angle	10	from 0.4 to 1.0 with a constant interval of 1/15

Geometry	cosine of local zenith angle	10	from 0.4 to 1.0 with a constant interval of 1/15
	relative azimuth angle	10	from 0° to 180° with a constant interval of 20°
Aerosol Models	fine Mode	4	four fine modes same as those in the retrieval algorithm
	coarse Mode	5	five coarse modes same as those in the retrieval algorithm
	fine mode weight	6	0, 0.2, 0.4, 0.6, 0.8, 1.0
Aerosol optical depth at 0.55 $\mu$ m		7	0.1, 0.2, 0.4, 0.6, 0.8, 1.0, 1.5

To simulate the calibration uncertainty, the ABI radiances in all channels were perturbed at 3% and 5% levels, which included 1) random noise without systematic bias; 2) positive and negative systematic biases; and 3) systematic biases plus random noise. Variation in channel-to-channel calibration was also simulated by adding a 3% bias to the individual channels. All together, there were 14 types of perturbations with 423,640 retrieval cases for each type. Outputs from the retrievals with perturbed radiance were compared with unperturbed retrieval results to evaluate the sensitivity of the algorithm to the calibration uncertainties.

The general results for the 14 types of sensitivity tests are displayed in Figure 3-2, where the averaged uncertainty and standard deviation of retrieved  $\tau_{0.55\mu\text{m}}$  and aerosol fine mode weight (FMW), as well as the percentage of misidentification of aerosol models are shown. The tests with perturbations in all ABI channels (top panel in Figure 3-2), indicate that the random noise does not introduce a bias in the retrieved  $\tau_{0.55\mu\text{m}}$  and FMW; however, the large standard deviations indicate large variability. Large positive systematic errors in all channel radiances lead to the overestimation of  $\tau_{0.55\mu\text{m}}$  and FMW, while an underestimation occurs with negative perturbations. The relative uncertainties of retrieved  $\tau_{0.55\mu\text{m}}$  (defined as  $\frac{\text{perturbed} - \text{unperturbed}}{\text{unperturbed}}$ ) are about 5% and 9% for the radiance biases at 3% and 5% levels, respectively. Associated FMW uncertainties are in the range of 0.01 to 0.04.

Perturbation of TOA reflectance in a single channel also exhibits significant influence on aerosol retrievals (last 4 columns of top panel in Figure 3-2). Increasing the TOA reflectance by 3% in the reference channel (0.86  $\mu$ m) results in a similar positive bias (~3%) in the retrieved  $\tau_{0.55\mu\text{m}}$ , while the averaged uncertainty of FMW is small (< 0.01). When the perturbation is applied to the other channels used for residual calculation, it changes the spectral shape of reflectance, therefore different aerosol models can be selected, which in turn, affects the retrieved  $\tau_{0.55\mu\text{m}}$  even when the reference channel is unperturbed. Such effect is seen when the TOA reflectance in the red channel (0.64  $\mu$ m) is enhanced by 3%. This change in spectral shape favors fine mode aerosol selection; as a result, the retrieved average FMW is increased by 0.025 and the corresponding  $\tau_{0.55\mu\text{m}}$

increased by 2%. On the other hand, increasing the TOA reflectance in the near-infrared channel (1.61  $\mu\text{m}$ ) by 3% favors coarse mode aerosols, and the retrieved FMW decreases by 0.02 while  $\tau_{0.55\mu\text{m}}$  increases by 3%. As for the SWIR channel (2.26  $\mu\text{m}$ ), it appears that the effect on the aerosol retrieval is small; however, the averaged uncertainty of retrieved  $\tau_{0.55\mu\text{m}}$  is about 1.6%, which cannot be deemed insignificant.

As seen from Figure 3-2, aerosol model selection is very sensitive to the perturbation of reflectance as the average rate of misidentification is above 40% and 50% for the 3% and 5% perturbation in all channels. Misidentification can be greater than 80% when the individual channel perturbation changes the spectral shape of TOA reflectance.

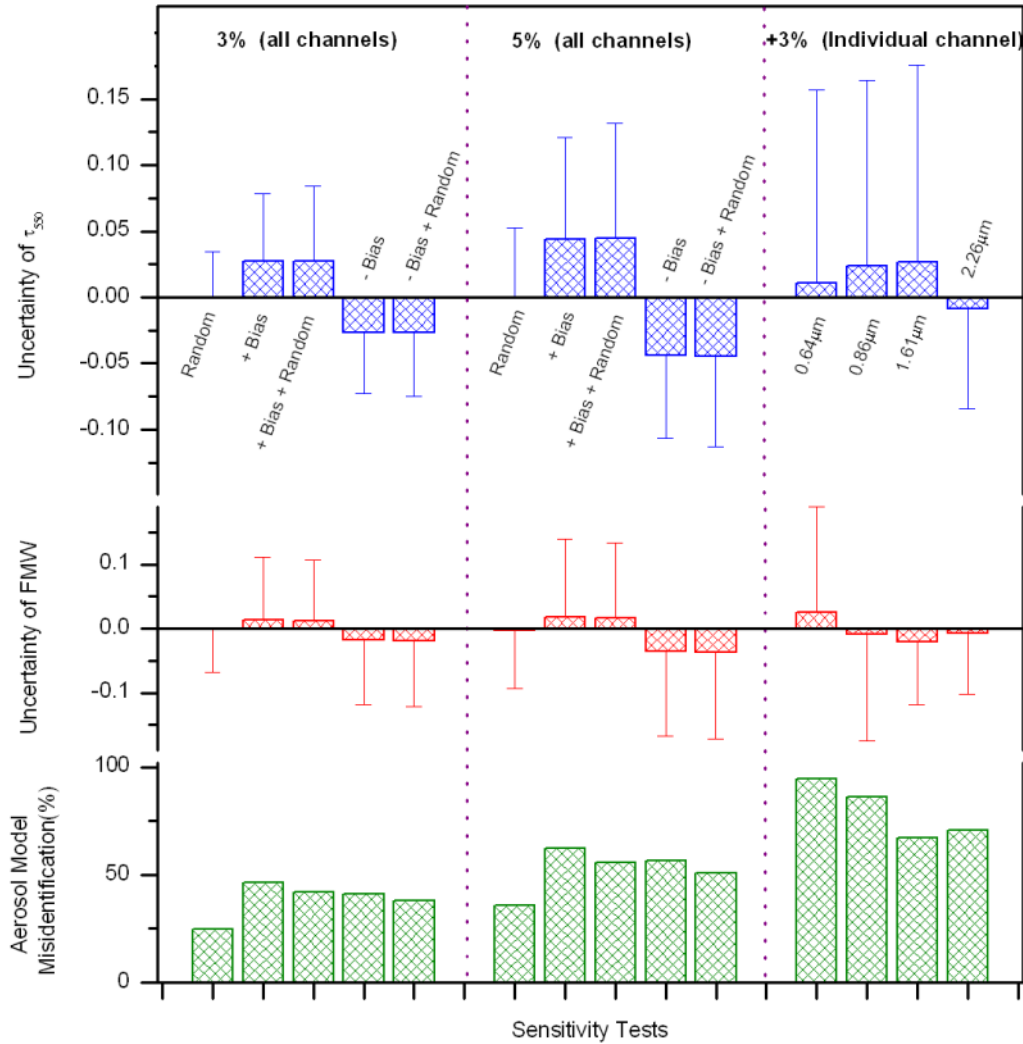


Figure 3-2. Average uncertainties in the retrieved aerosol optical depth at 0.55  $\mu\text{m}$ , fine-mode weight and percentage of model misidentification for all sensitivity tests.

It should be noted that the uncertainties calculated from these tests mask the detailed complex dependencies on the geometry, aerosol type and loading. An example of angular dependence is shown in Figure 3-3. In this case, the TOA reflectance at 1.61  $\mu\text{m}$  was increased by 3%, applied to the fine mode #2 and coarse mode #1 with 0.4 FMW and  $\tau_{0.55\mu\text{m}} = 0.2$ . The averaged uncertainty of retrieved  $\tau_{0.55\mu\text{m}}$  is -0.006, while the extreme values of  $\Delta\tau_{0.55\mu\text{m}}$  can be as large as 0.014 and -0.033. Similarly, the averaged  $\Delta$  FMW is -0.039, while the extreme values are 0.21 and -0.20.

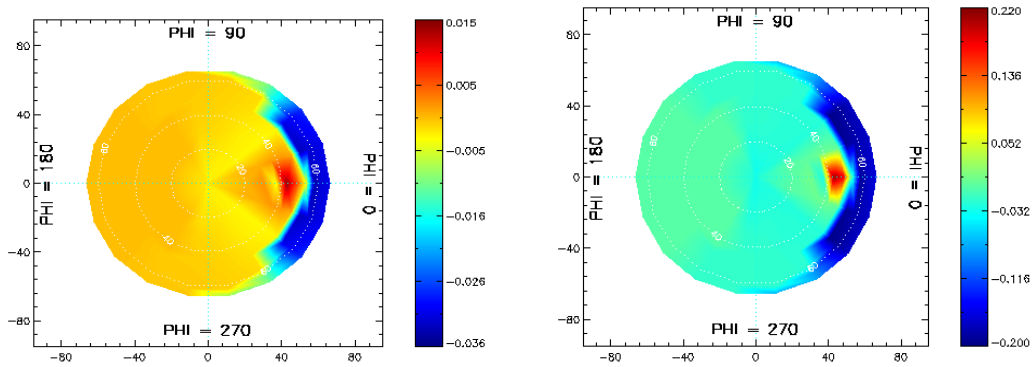


Figure 3-3. Angular dependence of the uncertainty of retrieved  $\tau_{550}$  (left) and FMW (right) for one case: increasing TOA reflectance at 1.61  $\mu\text{m}$  by 3%, applied to the second fine mode #2 and coarse mode #1 with 0.4 FMW and  $\tau_{550} = 0.2$ . Solar zenith angle is 42.83°. In the figure, local zenith angle increases in the radial direction; PHI represents the relative azimuth angle.

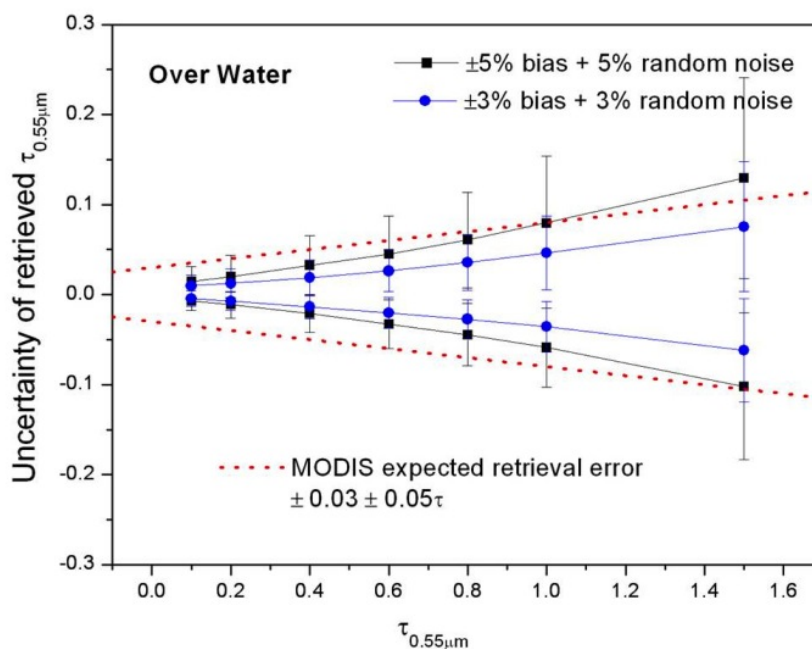


Figure 3-4. Uncertainty of retrieved aerosol optical depth at 0.55  $\mu\text{m}$  when all ABI channels used for aerosol retrieval over water are perturbed by 3% or 5% (systematic bias plus random noise).

Figure 3-4 shows the averaged uncertainty of retrieved  $\tau_{0.55\mu m}$  from tests in which TOA reflectances in all channels were perturbed by 3% and 5%. The results indicate that retrievals are within a retrieval error range of  $\pm 0.03 \pm 0.05\tau$  when  $\tau_{0.55\mu m}$  is less than 1.5. AOD values larger than 1.5 are very rare over the ocean, unless dust or smoke are transported from the continents.

Since other uncertainties (e.g., estimation of surface reflectance, gas absorption correction, cloud contamination, etc.) can also lead to errors in the TOA reflectance, the above sensitivity tests could serve as a general guide for estimating the “response” of the retrieval algorithm to these uncertainties, as well.

### 3.4.2 Physical and mathematical description for aerosol optical depth retrieval over land

#### 3.4.2.1 Strategy

The ABI aerosol algorithm over land follows a similar multi-channel strategy as that over ocean. The major differences include the usage of prescribed aerosol models and

estimation of surface reflection from ABI observations. This algorithm adopts the method from VIIRS [[Vermote et al., 2007] with an update of incorporating aerosol effects at 2.25µm channel, and adopting the land aerosol models from the MODIS Collection 5 [Remer et al., 2005, 2006; Levy et al., 2007].

Unlike water, land surface properties exhibit great variability and complexity, which prevent reliable modeling of the spectral reflectance. As a consequence, surface reflectance becomes an inherent unknown along with aerosol properties in the aerosol retrieval over land. Kaufman et al. [1997] observed that over vegetated and dark soil surfaces, the surface reflectance in the blue and red wavelengths correlated with the surface reflectance in the SWIR. The ABI algorithm follows the same strategy to utilize ABI channels 1, 2 and 6 (0.47, 0.64 and 2.25µm) to retrieve aerosol over dark surfaces.

Identifying dark target pixels is based on a threshold test which requires that the TOA reflectance observed in ABI channel 6 (2.25 µm) is not greater than 0.25. Spectral relationship of surface reflectance between visible (channel 1 and 2) and SWIR (channel 6) is prescribed (Section 3.4.2.3) using mid-IR NDVI (channel 3 and channel 6) to separate vegetation from soil surface type. Similarly to the MODIS Collection 5 algorithm, aerosol optical depth and surface reflectance are simultaneously retrieved from measurements in the blue (0.47 µm) and SWIR (2.25 µm) channels for each candidate aerosol models, and the optimal solution with the minimum difference between calculated and observed reflectance at red channel (0.64 µm) is selected.

Internal tests for screening out snow in the pixel are discussed in Appendix C. (Note: these tests are not yet implemented in Version 5 of the algorithm.)

### 3.4.2.2 Aerosol models

Four typical aerosol models as described by Levy et al. [2007] for MODIS collection C005 are adopted in the ABI algorithm. These represent generic, dust, smoke and urban aerosols. A bimodal lognormal distribution is used to describe each aerosol size distribution:

$$\frac{dV(r)}{d \ln r} = \sum_{i=1}^2 \frac{C_{V,i}}{\sqrt{2\pi}\sigma_i} \exp\left[-\frac{(\ln r - \ln r_{V,i})^2}{2\sigma_i^2}\right] \quad (3.4.14)$$

where  $V(r)$  is the volume corresponding to particles of radii within  $(r, r+dr)$ .  $C_{V,i}$  denotes the particle volume concentration,  $r_{V,i}$  is the median radius, and  $\sigma_i$  is the associated standard deviation. Microphysical properties of the candidate aerosol models are listed below in Table 3-10. Aerosol radiative properties are calculated with MIE code built in the 6S RTM for the spherical models (generic, urban and smoke), and the Dubovik spheroid kernel software [2006] is used for dust model to account for the non-spherical shape. Pre-calculated aerosol radiative properties are incorporated in the radiative transfer calculation for atmospheric reflectance, transmittance and spherical albedo stored in lookup table. Note that the generic, urban, and smoke models are dominated by the fine

mode, whereas the dust model is coarse-mode dominated. As the size distributions of the three fine-dominated models are similar, the main differences are in their absorption properties and refractive indices.

Table 3-10. Microphysical properties of land aerosols used in ABI algorithm

Aerosol Model	Mode	Volume median radius $r_V$	Standard Deviation $\sigma$	Volume Concentration $C_V$ ( $\mu\text{m}^3/\mu\text{m}^2$ )	Complex Refractive Index
Generic	Fine	0.145+ 0.0203 $\tau^{\&}$	0.3738+ 0.1365 $\tau$	0.1642 $\tau^{0.7747}$	1.43 - (0.008-0.002 $\tau$ )i
	Coarse	3.1007+ 0.3364 $\tau$	0.7292+ 0.098 $\tau$	0.1482 $\tau^{0.6846}$	
Urban	Fine	0.1604+ 0.434 $\tau$	0.3642+ 0.1529 $\tau$	0.1718 $\tau^{0.8213}$	1.42 - (0.007-0.0015 $\tau$ )i
	Coarse	3.3252+ 0.1411 $\tau$	0.7595+ 0.1638 $\tau$	0.0934 $\tau^{0.6394}$	
Smoke	Fine	0.1335+ 0.0096 $\tau$	0.3834+ 0.0794 $\tau$	0.1748 $\tau^{0.8914}$	1.51 - 0.02i
	Coarse	3.4479+ 0.9489 $\tau$	0.7433+ 0.0409 $\tau$	0.1043 $\tau^{0.6824}$	
Dust	Fine	0.1416 $\tau^{-0.0519}$	0.7561 $\tau^{0.148}$	0.087 $\tau^{1.026}$	$(1.48\tau^{-0.021}) - (0.0025 \tau^{0.132})i$ at 0.47 $\mu\text{m}^*$ $(1.48\tau^{-0.021}) - 0.002i$ at 0.55 $\mu\text{m}$ $(1.48\tau^{-0.021}) - (0.0018 \tau^{-0.08})i$ at 0.66 $\mu\text{m}$ $(1.46\tau^{-0.040}) - (0.0018 \tau^{-0.30})i$ at 2.12 $\mu\text{m}$
	Coarse	2.20	0.554 $\tau^{-0.0519}$	0.6786 $\tau^{1.0569}$	

<sup>&</sup> Aerosol optical depth ( $\tau$ ) is the spectral value at 0.55 $\mu\text{m}$ . The properties ( $r_V$ ,  $\sigma$  and  $C_V$ ) of smoke and generic aerosol model are defined for  $\tau < 2.0$ , and  $\tau = 2.0$  is used in calculation when  $\tau > 2.0$ . Likewise, parameters of urban and dust aerosol are defined for  $\tau < 1.0$ , and  $\tau = 1.0$  is applied for higher  $\tau$ .

\* Refractive index at other shortwave wavelength is estimated by spectral interpolation/extrapolation.

### 3.4.2.3 Retrieval of land surface reflectance

Over land, contribution of the surface ( $\rho_{surf}$ ) can be comparable or even larger than the atmospheric path reflectance ( $\rho_{atm}$ ), and accuracy of aerosol retrieval for such bright surface is expected to be low. Therefore the current algorithm retrieves aerosol only over sufficiently dark surfaces. Dark targets required by the algorithm are selected by requiring  $\rho_{2.25\mu\text{m}} \leq 0.25$ . Pixels with  $\rho_{2.25\mu\text{m}} > 0.25$  are discarded by the algorithm [Remer et al., 2005, 2006]. For the remaining dark target pixels, a linear relationship is used to estimate the surface reflectance at VIS channels of 0.47 and 0.64  $\mu\text{m}$  from that in the SWIR 2.25- $\mu\text{m}$  channel [Kaufman et al., 1997a 1997b, and 2002]. The physical reason for the spectral relationship is the simultaneous carotenoid, chlorophyll and liquid water absorption at blue, red and SWIR wavelengths associated with healthy vegetation [Kaufman and Remer, 1994].

The formulation of the VIS /SWIR relationship follows the VIIRS method, which makes use of the mid-IR NDVI to separate vegetation and soil surface types to improve the surface relationship based on analysis of Landsat data. VIIRS calculates the mid-IR NDVI,  $(\rho_{1.24} - \rho_{2.25})/(\rho_{1.24} + \rho_{2.25})$ , called 1.24- $\mu\text{m}$  NDVI, and determines vegetation-based surface as mid-IR NDVI  $\leq 0.2$  and soil-based surface otherwise. However, channel 1.24  $\mu\text{m}$  is not available on ABI. Therefore, the 0.86- $\mu\text{m}$  channel was tested and the threshold was tuned to best reproduce aerosol retrieval statistics. It was found that the ratio  $(\rho_{0.86} - \rho_{2.25})/(\rho_{0.86} + \rho_{2.25})$ , called 0.86- $\mu\text{m}$  NDVI, with a threshold of 0.1 could replace the 1.24- $\mu\text{m}$  NDVI. In order to better understand this replacement, the distribution of 0.86- $\mu\text{m}$  NDVI was analyzed in terms of the 1.24- $\mu\text{m}$  NDVI calculated from seven years of MODIS reflectances. As shown in Figure 3-5, the overlap area between the 1.24- $\mu\text{m}$  NDVI  $\geq 0.2$  and the 1.24- $\mu\text{m}$  NDVI  $< 0.2$  is about 10% for the 0.86- $\mu\text{m}$  NDVI, which suggests the 0.86- $\mu\text{m}$  NDVI is a good substitute for the 1.24- $\mu\text{m}$  NDVI, and the corresponding threshold is about 0.1 at the cross-over point that separates vegetation and soil. Note that the above reflectances in the mid-IR NDVI test use the observed TOA reflectance.

Therefore, the VIIRS VIS/SWIR surface relationship is transformed for ABI use as:

$$\rho_{0.64} = 0.55 * \rho_{2.25} \text{ and } \rho_{0.47} = 0.32 * \rho_{2.25} \quad (3.4.15)$$

for vegetation-based surface with mid-IR NDVI  $(\rho_{0.86} - \rho_{2.25})/(\rho_{0.86} + \rho_{2.25}) \geq 0.1$ , and

$$\rho_{0.64} = -0.113 + 1.03 * \rho_{2.25} \text{ and } \rho_{0.47} = -0.061 + 0.54 * \rho_{2.25} \quad (3.4.16)$$

for soil-based surface with  $(\rho_{0.86} - \rho_{2.25})/(\rho_{0.86} + \rho_{2.25}) < 0.1$ .

(These relationships between VIS/SWIR will need to be adjusted after the GOES-R launch.)

The 2.25- $\mu\text{m}$  surface reflectance needed in the above expressions is retrieved simultaneously with the optical depth. This process is described in Section 3.4.2.5.

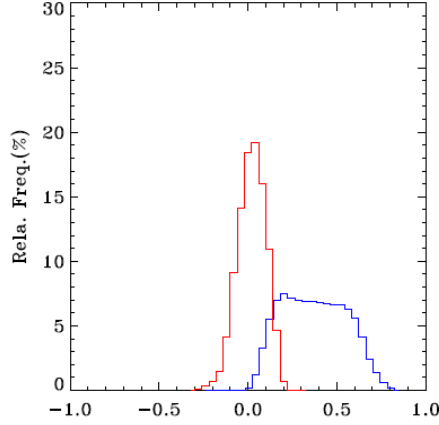


Figure 3-5. Relative frequency of 0.86- $\mu\text{m}$  NDVI for 1.24- $\mu\text{m}$  NDVI  $\geq 0.2$  (vegetation-based in blue) and 1.24- $\mu\text{m}$  NDVI  $< 0.2$  (soil-based in red).

### 3.4.2.4 Calculation of TOA reflectance

As described in Section 3.4.1.3, the TOA reflectance  $\rho_{toa}$  (Eq. 3.4.2) is the sum of atmospheric ( $\rho_{atm}$ ) and surface ( $\rho_{surf}$ ) contributions.

The path reflectance of the atmosphere  $\rho_{atm}$  is modeled following Eq. 3.4.3:

$$\rho_{atm} = T^{O_3} T^{og} \left[ (\rho_{R+A} - \rho_R(P_0)) T^{2^{H_2O}} + \rho_R(P) \right].$$

During the retrieval, the pre-calculated atmospheric reflectance  $\rho_{R+A}$  of a specific aerosol model and  $\tau_{550}$  is adjusted to local Rayleigh scattering and gas absorption. The look-up table values are interpolated to the actual observation geometry to get the optical functions at that geometry.

Under the assumption of Lambertian surface, the interaction between atmosphere and surface can be modeled using the adding equation of radiative transfer in a fairly simple manner [Chandrasekhar, 1960]. Therefore, the surface contribution to the TOA reflectance is calculated as:

$$\rho_{surf} = T^{O_3} T^{og} T^{H_2O} \left[ T_{R+A}^{\downarrow} T_{R+A}^{\uparrow} \frac{\rho_{lam}}{1 - S_{R+A} \rho_{lam}} \right], \quad (3.4.17)$$

where  $\rho_{lam}$  is the Lambertian land surface reflectance and the other terms are the same as in Section 3.4.1.3.

### 3.4.2.5 Aerosol retrieval algorithm over land

Due to the relatively strong aerosol signal and dark surface reflectance, TOA reflectances in the blue, red and SWIR channels are used for aerosol retrieval over land. Since three nearly independent observations allow us to extract three pieces of information, the ABI algorithm is designed to search for the appropriate aerosol model and retrieve  $\tau_{550}$  and surface reflectance by selecting the best match between ABI measurements and calculated reflectances.

The retrieval process can be described as individual retrievals for each candidate aerosol model followed by the determination of the best solution. For each aerosol model in the look-up table, the TOA reflectance in the blue and SWIR channels is used to invert  $\tau_{550}$  and surface reflectance. The associated residual is computed as the squared difference between calculated  $\rho_{0.64}^{cal}$  and observed reflectance  $\rho_{0.64}^{obs}$  in the red channel:

$$residual = (\rho_{0.64}^{cal} - \rho_{0.64}^{obs})^2. \quad (3.4.18)$$

The combination of surface albedo, aerosol optical depth and aerosol model with the minimum residual is chosen as the solution.

Aerosol optical depths in five ABI channels (channels 1,2,3,5, and 6) are calculated from the spectral dependence of the aerosol normalized extinction coefficient  $n_{ext}$  of the retrieved aerosol model. Since  $n_{ext}$  for the land aerosol model is a function of  $\tau_{550}$ , the  $n_{ext,\lambda}$  is linearly interpolated to the retrieved  $\tau_{550}$ , and the optical depth at wavelength  $\lambda$  is calculated as  $\tau_{\lambda} = n_{ext,\lambda} \times \tau_{550}$ .

The procedure of simultaneous retrieval of  $\tau_{550}$  and surface reflectance is illustrated in Figure 3-6. For any given aerosol model, a retrieval is performed by looping over the aerosol optical depth  $\tau_{550}$  in the look-up table in ascending order. At any step  $i$  in the loop, a Lambertian surface reflectance ( $\rho_{lam,i}$ ) in the SWIR channel is retrieved based on Eq. 3.4.19, which is derived from Eq. 3.4.17:

$$\rho_{lam,i} = \frac{R}{R * S_{R+A} + T_{R+A}^{\downarrow} T_{R+A}^{\uparrow} T^{H_2O}} \quad (3.4.19)$$

where  $R = \frac{\rho_{obs} - \rho_{atm}}{T^{O_3} T^{og}}$ , and  $\rho_{atm}$  is the atmospheric path reflectance corresponding to the  $i^{th}$  AOD in LUT ( $\tau_{550,i}$ ). Surface reflectances at 0.47 and 0.64  $\mu\text{m}$  are then estimated through the prescribed relationships discussed in Section 3.4.2.3. When a valid  $\rho_{lam,i}$  is retrieved (value is between 0 and 1) the TOA reflectance in the 0.47- $\mu\text{m}$  channel ( $\rho_{0.47,i}$ ) is calculated from  $\tau_{550,i}$  and  $\rho_{lam,i}$ . The loop of  $\tau_{550,i}$  is terminated once  $\rho_{0.47,i}$  converges to the observation ( $\rho_{0.47}^{obs}$ ). Here convergence means two adjacent steps in the loop,  $i$  and  $i+1$ , are found such that  $\rho_{0.47}^{obs}$  falls within  $\rho_{0.47,i}$  and  $\rho_{0.47,i+1}$ . The  $\tau_{550}$  for the current aerosol model is determined by linear interpolation:

$$\tau_{550} = \tau_{550,i} * \frac{\rho_{0.47,i+1} - \rho_{0.47}^{obs}}{\rho_{0.47,i+1} - \rho_{0.47,i}} + \tau_{550,i+1} * \frac{\rho_{0.47}^{obs} - \rho_{0.47,i}}{\rho_{0.47,i+1} - \rho_{0.47,i}} \quad (3.4.20)$$

The final surface reflectance  $\rho_{lam}$  is calculated similarly from  $\rho_{lam,i}$  and  $\rho_{lam,i+1}$ .

The retrieval of 2.25- $\mu\text{m}$  surface reflectance essentially finds the surface reflectance that when coupled with the atmosphere with a given aerosol optical depth results in the observed TOA reflectance  $\rho_{toa}(2.25)$ . This retrieval yields a negative surface reflectance when the atmosphere is already brighter than the observed reflectance, that is when  $\rho_{atm}(2.25) > \rho_{toa}(2.25)$  in Eq. 3.4.2. Because of the negative offsets in Eq. 3.4.16 for soil-based reflectance the 0.47 and 0.64- $\mu\text{m}$  surface reflectances can also become negative even when the 2.25- $\mu\text{m}$  reflectance itself is positive. Negative surface albedos are unphysical and therefore must be dealt with in the retrieval (see below). The 2.25- $\mu\text{m}$  reflectance retrieval can also lead to larger than unity when the atmosphere is “too dark”, that is when  $\rho_{atm}(2.25) \ll \rho_{toa}(2.25)$  even for the largest optical depth in the LUT. Since the surface is assumed Lambertian a larger than unity surface reflectance is also unphysical.

Another special case that must be treated is when the observed TOA 0.47- $\mu\text{m}$  reflectance is outside of the range of the ones calculated for a given aerosol model from the aerosol optical depth values in the LUT and from the retrieved 0.47- $\mu\text{m}$  surface reflectance, that is when  $\rho_{0.47}^{obs} < \rho_{0.47,1}$  or  $\rho_{0.47}^{obs} > \rho_{0.47,N}$ , where  $N$  is the number of optical depth values in LUT.

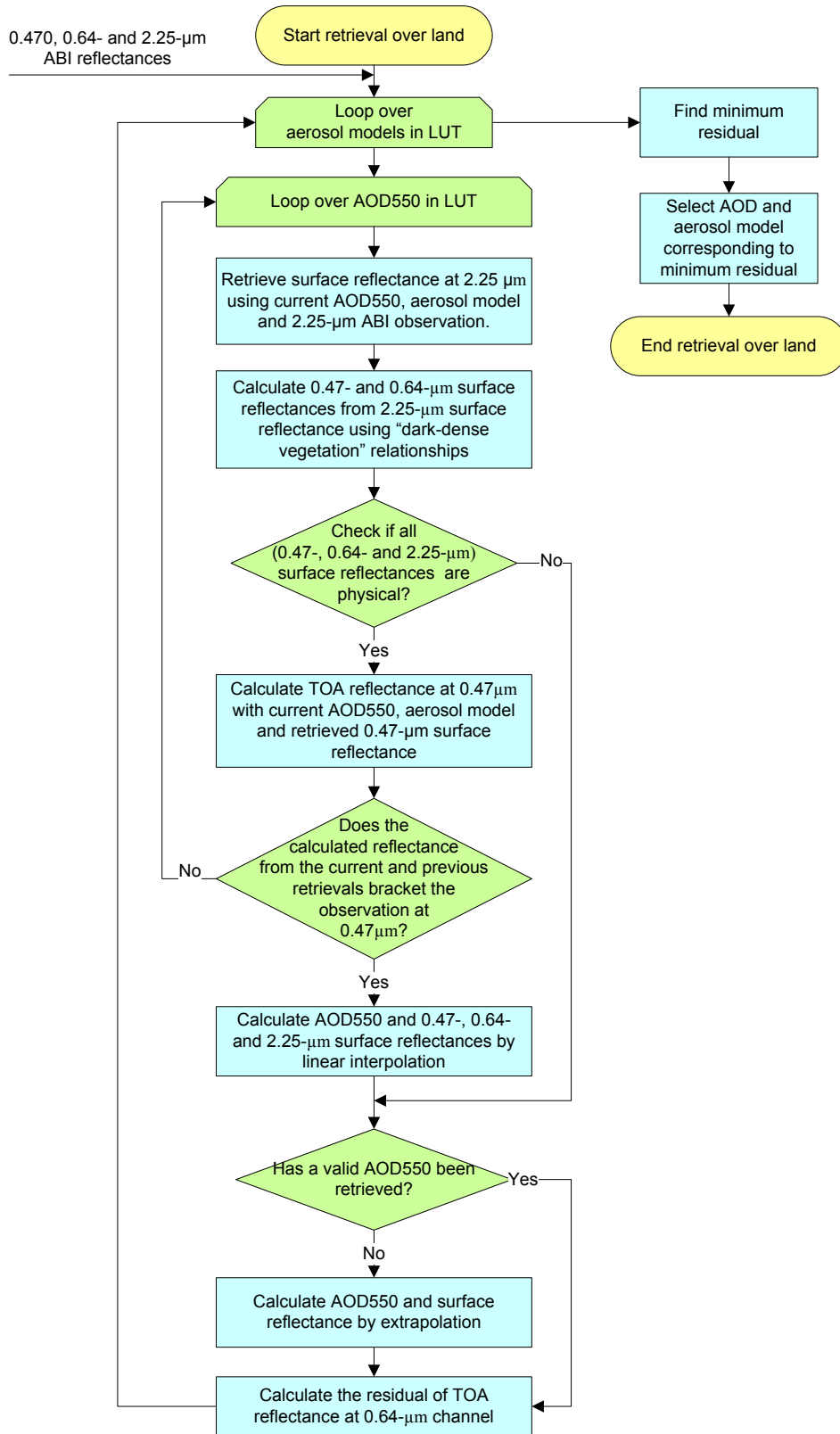


Figure 3-6. Flowchart of aerosol retrieval over land.

Both of the above special cases are handled by extrapolation of the AOD and the surface reflectance using Eq. 3.4.20. Denoting the step by  $j$  in which (any of) the surface reflectance is unphysical or  $\rho_{0.47}^{obs}$  is out of range, first  $\rho_{0.47}^{obs}$  is compared to the TOA reflectance calculated for the first value of the AOD in the LUT ( $\rho_{0.47,1}$ ) and to the one calculated in step  $j-1$  ( $\rho_{0.47,j-1}$ ). If  $\rho_{0.47}^{obs}$  is closer  $\rho_{0.47,1}$  then retrievals from the first two steps ( $\tau_{550,1}, \tau_{550,2}$ ) are used in the extrapolation. Otherwise, the aerosol optical depth  $\tau_{550}$  and surface reflectance (in all channels)  $\rho_{lam}$  are extrapolated from the calculated TOA ( $\rho_{0.47,j-1}, \rho_{0.47,j}$ ) and retrieved surface reflectances ( $\rho_{lam,j-1}, \rho_{lam,j}$ ) corresponding to the optical depth values ( $\tau_{550,j-1}, \tau_{550,j}$ ) at steps  $j-1$  and  $j$ . The extrapolation is not performed when  $j < 2$ ; in this case no retrieval is done and all values are set to missing.

Once  $\tau_{550}$  and  $\rho_{lam}$  are determined for the current aerosol model, the residual is calculated based on Eq. 3.4.18; it is then used to select the best solution among all the candidate aerosol models after the loop over all aerosol models finished.

Compared with algorithms where transparency of aerosol in the SWIR channel is assumed, the current algorithm is expected to improve aerosol retrievals for the enhanced aerosol cases. As expected, the evaluation with collocated MODIS and AERONET data during the period of year 2000 to 2009 shows that the accuracy of retrieved  $\tau_{550}$  is improved by  $\sim 40\%$  for the large AOD cases ( $\tau_{550} > 0.8$ ). Accounting for the aerosol effect in the SWIR channel decreases the estimated surface reflectance in that channel by  $\sim 0.003$  (2.5%) and increases the retrieved  $\tau_{550}$  by  $\sim 0.012$  (5.3%). Unlike the previous version of the algorithm, which assumed transparency of aerosol in the SWIR channel, the current version exhibits less preference for selecting the coarse mode aerosol model. (The previous version retrieved unrealistically large number of pixels with coarse mode aerosol.) The number of cases where dust model is selected is reduced by  $\sim 10.7\%$ , while the number of smoke retrievals is increased by  $\sim 8.3\%$ .

### 3.4.2.6 Sensitivity study

Tests of the sensitivity of aerosol retrieval over land to the uncertainty of TOA reflectance were performed. Similar to the tests over water, the TOA reflectances were estimated from radiative transfer calculations for the same set of geometries and aerosol optical depths. Four aerosol models used in the retrieval algorithm were adopted. Ten values of surface reflectances ranging from 0.02 to 0.2 at  $2.25\mu\text{m}$  with a constant interval of 0.02 were used. Perturbations to the ABI radiances in all channels were applied at 3% and 5% levels, which included 1) random noise; 2) positive and negative systematic biases; and 3) systematic biases plus random noise. Variation in channel-to-channel calibration was also simulated by adding a +3% bias to the individual channels. Overall, there were 13 types of perturbations with 280,000 retrieval cases for each type. Outputs from the retrievals with perturbed radiances were compared with unperturbed retrieval results to evaluate the sensitivity of the algorithm to the calibration uncertainties.

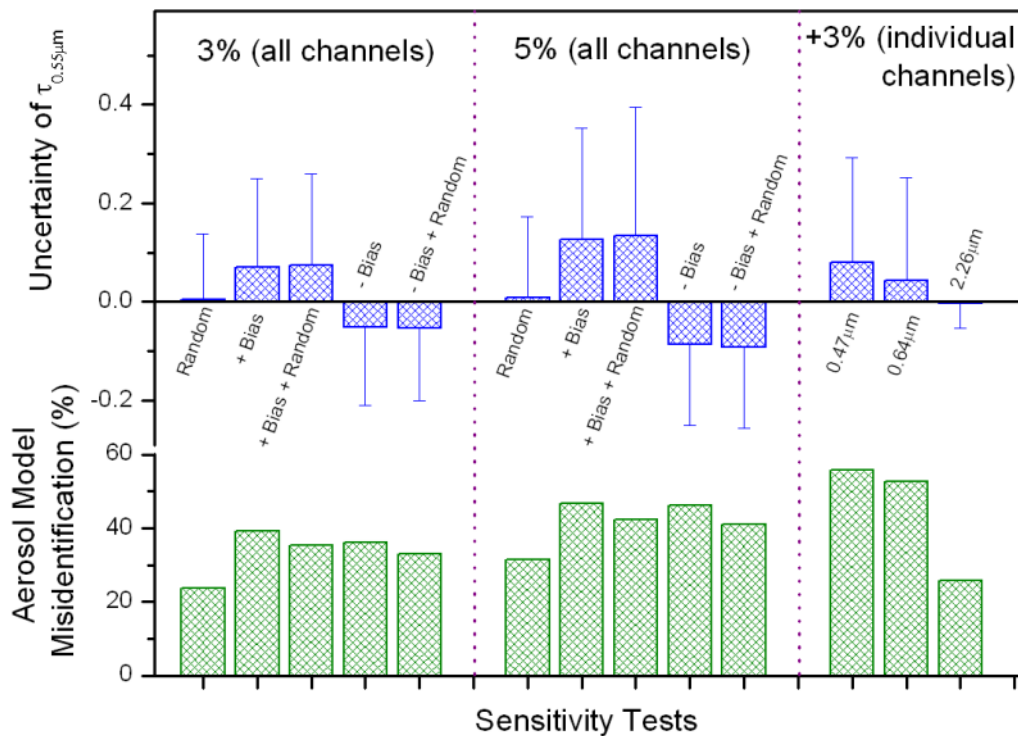


Figure 3-7. Average uncertainties in the retrieved aerosol optical depth at 0.55  $\mu\text{m}$  (top) and percentage of model misidentification (bottom) for the sensitivity tests of the aerosol retrieval over land.

The general results of the sensitivity tests are shown in Figure 3-7. The conclusions are similar to those described in Section 3.4.1.6 for the over-water retrieval. Specifically, the small bias but large dispersion of retrieved  $\tau_{550}$  is associated with the random perturbation of the TOA reflectances. The general overestimation/underestimation of  $\tau_{550}$  is associated with positive/negative biases of the TOA reflectance, with values of about 13% and 23% for the 3% and 5% systematic perturbations. This sensitivity is larger than that over water, and it can be attributed to the brighter land surface, which leads to a larger change of the TOA reflectance than that over water for the same percentage of perturbation applied. Perturbation of the individual channels also affects the retrievals with error in the 2.26- $\mu\text{m}$  channel having the smallest effect. The latter is due to the fact that only small fractions of the perturbation in the SWIR channel (through the spectral relationship of surface reflection) are transferred to the uncertainty of surface reflectance and enter into the retrieval process. Model misidentification is about 35% and 40% for the 3% and 5% perturbation of reflectances. Changing the spectral shape of TOA

reflectance by perturbing the radiance in a single visible channel increases the misidentification rate to more than 50%.

The large standard deviation associated with the above reported average values are due to the dependence of aerosol retrieval on geometry, surface brightness, aerosol type and loading. Examples of these dependencies are shown in Figure 3-8. It can be seen that the sensitivity of retrieved aerosol optical depth increases along with the surface reflectance, i.e., larger uncertainty is associated with a brighter surface. The relative uncertainty of the retrieved  $\tau_{550}$  decreases with optical depth, while the opposite is true for the absolute uncertainty. Geometry is also an important factor; sensitivity is larger at the back and forward scattering angles. As for the dynamic model selection, due to its distinctive characteristics, identification of the dust model is the most robust; while it appears difficult to distinguish between generic and urban models at the 5% perturbation level.

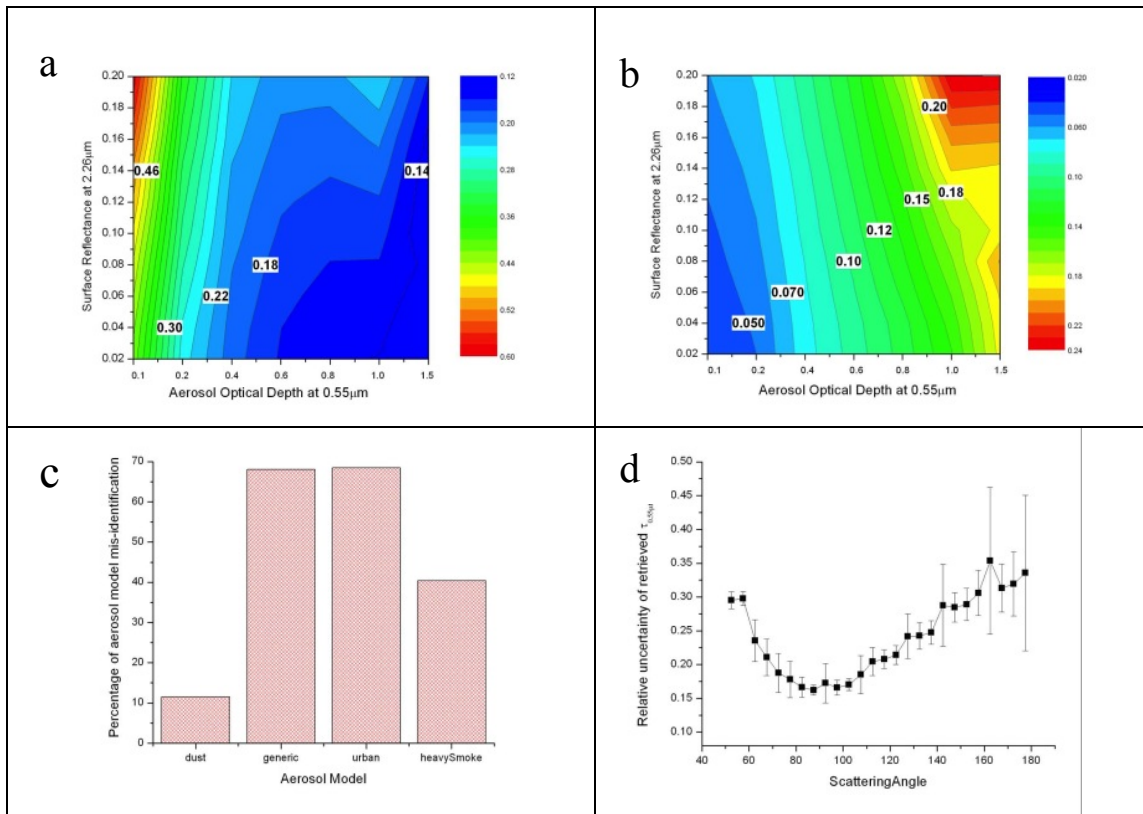


Figure 3-8. Sensitivity test results of aerosol retrieval over land with TOA reflectance increased by 5% in channels. a) relative uncertainty of retrieved  $\tau_{550}$  as functions of surface reflectance and  $\tau_{550}$ ; b) absolute uncertainty of retrieved  $\tau_{550}$  as functions of surface reflectance and  $\tau_{550}$ ; c) percentage of misidentification for each aerosol model; d) relative uncertainty of retrieved  $\tau_{550}$  as function of scattering angle.

Figure 3-9 shows the average uncertainty of retrieved  $\tau_{550}$  as a function of AOD for the tests when all ABI channels are perturbed by 3% or 5%. It appears that, on average, the retrievals are within an error range of  $\pm 0.05 \pm 0.15\tau$  when  $\tau_{550}$  is less than 1.5.

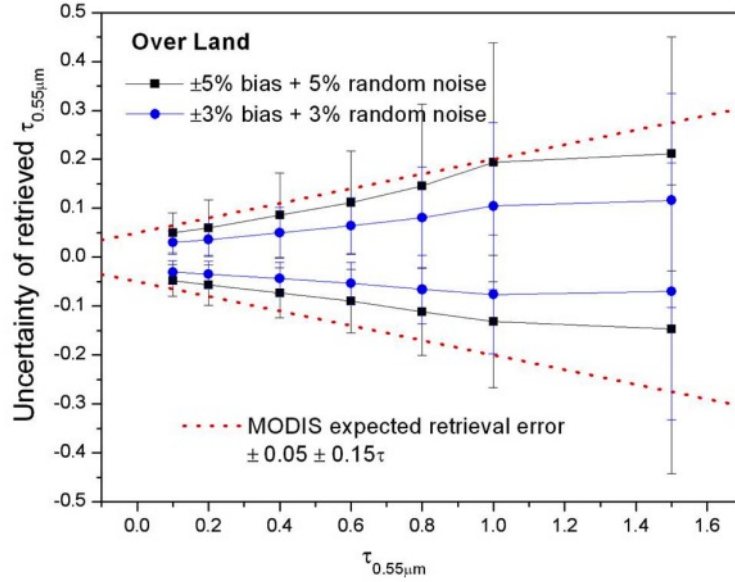


Figure 3-9. Uncertainty of retrieved aerosol optical depth at 0.55  $\mu\text{m}$  when all ABI channels used for aerosol retrieval over land are perturbed by 3% or 5% (systematic bias plus random noise).

### 3.4.3 Calculation of aerosol size parameter

The wavelength ( $\lambda$ ) dependence of aerosol optical depth is usually described as  $\tau \propto \lambda^{-\alpha}$ , where  $\tau$  is the optical depth and  $\alpha$  is the Ångström exponent. Large/small values of Ångström exponent indicate small/large particles, respectively. The Ångström exponent is calculated as the linear slope of aerosol optical depth versus wavelength in log scale for two wavelength pairs of (0.47, 0.86)  $\mu\text{m}$  and (0.86, 2.25)  $\mu\text{m}$ :

$$\alpha_{0.47;0.86} = -\frac{\ln\tau_{0.47} - \ln\tau_{0.86}}{\ln 0.47 - \ln 0.86} \quad (3.4.21)$$

$$\alpha_{0.86;2.25} = -\frac{\ln\tau_{0.86} - \ln\tau_{2.25}}{\ln 0.86 - \ln 2.25} \quad (3.4.22)$$

### 3.4.4 Calculation of suspended matter mass concentration

The National Weather Service (NWS) has a requirement for PM2.5 (particulate mass in  $\mu\text{g}/\text{m}^3$  of particles smaller than 2.5  $\mu\text{m}$  in median diameter) because its models predict PM2.5 concentration. NWS therefore needs AOD to be scaled to PM2.5. This scaling would require knowledge of aerosol type and height of the aerosol layer. However, the vertical distribution of aerosols cannot be determined from ABI. Therefore, the current algorithm reports column integrated mass concentration in  $\mu\text{g}/\text{cm}^2$ .

The GOES-R ABI aerosol algorithm retrieves AOD along with one aerosol model over land and one coarse-mode and one fine-mode aerosol model with a fine-mode weight fraction over water. The retrieved AOD can be scaled into column integrated suspended matter in units of  $\mu\text{g}/\text{cm}^2$  using a mass extinction coefficient ( $\text{cm}^2/\mu\text{g}$ ) computed for the aerosol models identified by the ABI algorithm. The approach used in the MODIS Collection 5 algorithm was adopted [Remer et al., 2005; 2006], which converts the retrieved aerosol optical depth to column mass concentration (SM) by dividing it by the relevant mass extinction coefficient ( $B_{ext}$ ).

Over land, the mass extinction coefficient  $B_{ext}$  is a function of aerosol type and AOD (Table 3-11), and the column integrated suspended matter SM is calculated as:

$$SM = \frac{\tau_{550}}{B_{ext}}. \quad (3.4.23)$$

Over ocean, the final SM is obtained from combining the fine and coarse modes as:

$$SM = \frac{\tau^f}{B_{ext}^f} + \frac{\tau^c}{B_{ext}^c}, \quad (3.4.24)$$

where  $B_{ext} = \frac{3 M^{(2)}}{4 M^{(3)}} \frac{Q_{ext}}{d}$ ,  $Q_{ext}$  is the extinction efficiency,  $M^{(n)}$  is the  $n^{\text{th}}$  moment of the aerosol number size distribution, (

Aerosol model	Aerosol extinction optical thickness $\tau_{550}$									
	1.00	1.20	1.40	1.60	1.80	2.00	2.50	3.00	4.00	5.00
Generic	30.043	29.307	28.572	27.836	27.101	26.365	26.189	26.013	25.799	25.584
Urban	26.825	26.648	26.470	26.293	26.115	25.938	25.7005	25.463	25.184	24.905
Smoke	26.492	26.171	25.850	25.528	25.207	24.886	24.579	24.271	23.917	23.563
Dust	71.541	72.309	73.077	73.845	74.613	75.381	75.479	75.577	75.699	75.822

Table 3-12), and  $d$  is the particle density assumed to be  $10^6 \mu\text{g}/\text{cm}^3$ .  $\tau^f = \eta \times \tau_{550}$ ,  $\tau^c = (1 - \eta) \times \tau_{550}$ , where  $\eta$  is the fine mode weight and  $\tau_{550}$  is the retrieved AOD at 550nm. Plugging  $B_{ext}$  into Eq. (3.4.24) one finds:

$$SM = \tau_{550} \times \left[ \eta \left( \frac{M^{(3)}}{\pi M^{(2)} Q_{ext}} \right)^f + (1 - \eta) \left( \frac{M^{(3)}}{\pi M^{(2)} Q_{ext}} \right)^c \right] \times \frac{4\pi d}{3} \times 10^{-12} \quad (3.4.25)$$

where  $\pi M^{(2)} Q_{ext}$  and  $M^{(3)}$  are the first and second quantities in Table 3-12. Since  $M^{(3)}$  is in unit of  $\mu\text{m}^3$ , the factor of  $10^{-12}$  converts  $M^{(3)}$  to  $\text{cm}^3$ .

In general, SM retrievals will only be validated indirectly via the comparison of ABI aerosol optical depth and particle size parameter with AERONET measurements. NWS recognizes this validation approach as adequate, as long as periodic spot check verification will also be performed/leveraged with *in situ* (aircraft) profile measurements of suspended matter. Accuracy and precision can be translated from AOD units to  $\mu\text{g}/\text{cm}^2$  units if needed but the ABI algorithm will be assessed based on AOD.

Table 3-11. Inverse of mass-extinction coefficients for over-land aerosols [ $\text{cm}^2/\mu\text{g}$ ]

Aerosol model	Aerosol extinction optical thickness $\tau_{550}$									
	0.00	0.01	0.05	0.10	0.15	0.20	0.30	0.40	0.60	0.80
Generic	37.529	37.529	37.529	37.529	37.529	37.529	36.868	35.545	33.387	31.715
Urban	31.678	31.678	31.678	31.678	31.678	31.678	31.1716	30.159	28.682	27.753
Smoke	30.117	30.117	30.117	30.117	30.117	30.117	29.755	29.031	27.944	27.218
Dust	63.792	63.792	63.792	63.792	63.792	63.792	64.573	66.134	68.465	70.003
Aerosol model	Aerosol extinction optical thickness $\tau_{550}$									
	1.00	1.20	1.40	1.60	1.80	2.00	2.50	3.00	4.00	5.00
Generic	30.043	29.307	28.572	27.836	27.101	26.365	26.189	26.013	25.799	25.584
Urban	26.825	26.648	26.470	26.293	26.115	25.938	25.7005	25.463	25.184	24.905
Smoke	26.492	26.171	25.850	25.528	25.207	24.886	24.579	24.271	23.917	23.563
Dust	71.541	72.309	73.077	73.845	74.613	75.381	75.479	75.577	75.699	75.822

Table 3-12. Extinction Properties ( $\pi Q_{ext} M^{(2)}$  in  $\text{cm}^2$  and  $M^{(3)}$  in  $\mu\text{m}^3$ ) of Ocean Aerosol Models

	<i>Fine mode</i>				
Model	F1	F2	F3	F4	
$\pi Q_{ext} M^{(2)}$	0.9300E-10	0.2331E-09	0.5449E-09	0.1124E-08	
$M^{(3)}$	0.00070	0.00108	0.00255	0.00498	
	<i>Coarse mode</i>				
Model	C1	C2	C3	C4	C5
$\pi Q_{ext} M^{(2)}$	0.2782E-07	0.5757E-07	0.9718E-07	0.5565E-07	0.6537E-07
$M^{(3)}$	0.31890	1.07600	2.55100	1.07600	2.10500

### 3.4.5 Look-up table

Two lookup tables (LUT), one for the atmosphere (aerosol plus molecules at standard pressure) and one for the ocean surface reflectance, store reflectances, transmittances and other quantities pre-calculated for discrete states of the atmosphere and the ocean surface. The tables were calculated with the vector version of the 6S radiative transfer code [Vermote et al., 1997; Kotchenova et al., 2006; 2007]. The atmospheric LUT is produced for a black surface (surface reflectance is zero). This increases flexibility since potentially any surface can be used to couple the atmosphere with in the retrieval. Note that the calculations are performed for the central wavelengths of the ABI channels. The lookup tables are for atmospheres free of gas absorption, and the spectral variability of aerosol extinction and molecular scattering are weak in the narrow ABI bands to warrant monochromatic calculations.

#### 3.4.5.1 Atmospheric look-up table

The atmospheric LUT contains radiative functions and mass extinction coefficients used to retrieve aerosol optical depth and suspended matter mass concentration. Table 3-13 lists the contents of this LUT. The corresponding discrete values for each dimension are listed in Table 3-14.

Table 3-13. Contents of atmospheric look-up table

Data Set Name	Description	Size of Dimensions
tau550	Discrete aerosol optical depth at 550nm in LUT	(20) (Ntau)
solar_zenith_angle	Discrete solar zenith angle in LUT	(21) (Nsolzen)
sensor_zenith_angle	Discrete sensor zenith angle in LUT	(25) (Nsenzen)
scattering_angle_position	Scattering angle indexing vector	(525) (Nsolzen x Nsenzen)
land_aer_nor_extinction_coef	Normalized extinction coefficient for land aerosol models in ABI channels 1,2,3,5,6	(4,20,5) (Nlndaer, Ntau, Nchn)
land_aer_sph_alb	Atmospheric spherical albedo corresponding to candidate land aerosol models	(4,20,3) (Nlndaer, Ntau, Nlndchn)
land_aer_trans	One-way atmospheric transmittance corresponding to candidate land aerosol models	(4,20,3,21) (Nlndaer, Ntau, Nlndchn, Nsolzen)
land_aer_refl	Atmospheric reflectance corresponding to candidate land aerosol models	(4,20,3,7506) (Nlndaer, Ntau, Nlndchn, Nscat)
water_aer_nor_extinction_coef	Normalized extinction coefficient for ocean aerosol models in ABI channels 1,2,3,5,6	(9, 5) (Nwataer, Nchn)
water_aer_sph_alb	Atmospheric spherical albedo corresponding	(9,20,4)

	to candidate ocean aerosol models	(Nwataer, Ntau, Nwatchn)
water_aer_trans	One-way atmospheric transmittance corresponding to candidate ocean aerosol models	(9,20,4,21) (Nwataer, Ntau, Nwatchn, Nsolzen)
water_aer_refl	Atmospheric reflectance corresponding to candidate ocean aerosol models	(9,20,4,7506) (Nwataer, Ntau, Nwatchn, Nscat)
land_aer_mass_ext_coef	Inverse of mass extinction coefficients for land aerosol models	(4,20) (Nlndaer, Ntau)
water_aer_mass_ext_coef	Parameters used for computing mass extinction coefficients for ocean aerosol models	(9,2) (Nwataer, Npars)

Table 3-14. Discrete values/description of atmospheric LUT dimensions

Dimension Name	Variable Name in Table	Number of Values	Discrete Values/Description
AOT at 550nm	Ntau	20	0.00, 0.01, 0.05, 0.10, 0.15, 0.20, 0.30, 0.40, 0.60, 0.80, 1.00, 1.20, 1.40, 1.60, 1.80, 2.00, 2.50, 3.00, 4.00, 5.00
Solar zenith angle	Nsolzen	21	0°, 4°, 8°, 12°, 16°, 20°, 24°, 28°, 32°, 36°, 40°, 44°, 48°, 52°, 56°, 60°, 64°, 68°, 72°, 76°, 80°
Sensor zenith angle	Nsenzen	25	0.0°, 2.84°, 6.52°, 10.22°, 13.93°, 17.64°, 21.35°, 25.06°, 28.77°, 32.48°, 36.19°, 39.90°, 43.61°, 47.32°, 51.03°, 54.74°, 58.46°, 62.17°, 65.88°, 69.59°, 73.30°, 77.01°, 80.72°, 84.43°, 88.14°
ABI channels for aerosol extinction coefficient	Nchn	5	ABI channels 1, 2, 3, 5, 6 (0.47, 0.64, 0.865, 1.61, 2.25 μm)
ABI channels for land aerosol radiative functions	Nlndchn	3	ABI channels 1, 2, 6 (0.47, 0.64, 2.25 μm)
Land aerosol models	Nlndaer	4	Dust, Generic, Urban, Smoke
Scattering angle	Nscat	7506	Every 4° interval in the range from 180-( $\theta_s+\theta_v$ ) to 180- $ \theta_s-\theta_v $ for all pairs combination of solar zenith angle ( $\theta_s$ ) and sensor zenith angle ( $\theta_v$ )
Ocean aerosol models	Nwataer	9	Four fine modes plus five coarse mode
ABI channels for ocean aerosol radiative functions	Nwatchn	4	ABI channels 2, 3, 5, 6 (0.64, 0.865, 1.61, 2.25 μm)
Parameters used for computing mass extinction coefficient for ocean aerosol	Npars	2	$\beta_{ext}$ and $M^{(3)}$ extinction coefficient [ $cm^2$ ] and third moment of size distribution [ $\mu m^3$ ]

### **3.4.5.1.1 Mass extinction coefficients for land aerosols**

Inverse of mass extinction coefficients are provided for four candidate land aerosol models and for each of the twenty aerosol optical depths. Linear interpolation on the optical depth dimension is needed to estimate the coefficient to convert the retrieved aerosol optical depth to mass concentration (ATBD Section 3.4.4).

### **3.4.5.1.2 Mass extinction coefficient for ocean aerosols**

Two sets of parameters are provided to estimate mass extinction coefficient for the ocean aerosol models. Specifically, the extinction coefficient at  $0.55\mu\text{m}$  ( $\beta_{\text{ext}} = \pi M^{(2)} Q_{\text{ext}}$ ) and  $M^{(3)}$  are available from LUT for each of the nine ocean aerosol models (four fine and five coarse modes), where  $M^{(n)}$  is the  $n^{\text{th}}$  moment of the log-normal aerosol particle size distribution and  $Q_{\text{ext}}$  is the aerosol extinction efficiency. Aerosol properties and mass extinction coefficients of ocean models do not depend on the optical depth as land aerosol models do. The units of the first coefficient ( $\beta_{\text{ext}}$ ) is in  $\text{cm}^2$ , and the unit of the second coefficient ( $M^{(3)}$ ) is in  $\mu\text{m}^3$ . Mass extinction coefficient is computed according to Section 3.4.4 of the ATBD.

### **3.4.5.1.3 Normalized spectral aerosol extinction coefficient**

Normalized spectral aerosol extinction coefficients are provided for all candidate aerosol models in five ABI channels (channels 1, 2, 3, 5, 6). For the land aerosol models, the coefficients are function of optical depth and interpolation on the optical depth dimension is needed to apply to the retrieved value.

### **3.4.5.1.4 Spherical albedo**

Atmospheric spherical albedos ( $S_{\text{R+A}}$ , subscript R+A represents combined contributions from both molecules and aerosols) are provided for each aerosol model and optical depth for the channels used in the retrieval. Since the spherical albedo is the integrated bidirectional reflectance distribution function over both illumination and viewing hemispheres, it does not depend on geometry and there is no need for interpolation.

### **3.4.5.1.5 Transmittance**

One-way atmospheric transmittances ( $T_{\text{R+A}}$ ) are provided for each aerosol model and optical depth for the channels used in the retrieval. The total transmittance is the sum of direct and diffuse components and assumed to be azimuthally invariant. Transmittances at twenty-one discrete zenith angles (for  $0^\circ$  to  $80^\circ$  in step of  $4^\circ$ ) are provided to describe the dependence on illumination and viewing geometry. The downward and upward

transmittance ( $T_{R+A}^\downarrow$  and  $T_{R+A}^\uparrow$ ) are estimated by linear interpolation of the one-way transmittance LUT to the solar zenith angle and sensor zenith angle, respectively.

### 3.4.5.1.6 Reflectance

Under the plane-parallel assumption, dependence of atmospheric reflectance on geometry is usually specified by the solar zenith angle  $\theta_s$ , view zenith angle  $\theta_v$  and corresponding azimuth angles. When no provision is made for preferentially oriented scatterers, and thus scattering depends only on the angle between the incident and scattered beam (scattering angle,  $\Theta$ ), not on the incident and scattered directions separately, the dependence can be described by the scattering angle. For a given pair of  $\theta_s$  and  $\theta_v$ , the realizable scattering angle spans a range of  $[\Theta_{\min}, \Theta_{\max}]$  depending on the relative azimuth angle ( $\phi$ ), where  $\Theta_{\min}=180^\circ-(\theta_s+\theta_v)$  and  $\Theta_{\max}=180^\circ-|\theta_s-\theta_v|$ . As a result, the actual scattering angle range varies for different combinations of  $\theta_s$  and  $\theta_v$ .

Normally, the atmospheric reflectance is calculated for discrete values of  $\theta_s$ ,  $\theta_v$  and  $\phi$  in a lookup table to describe its angular dependence. However, such scheme leads to a varying resolution in scattering angle for different atmospheric paths. For example, there are the same number (number of discrete  $\phi$  values) of reflectances pre-calculated for the case of  $\theta_s=10^\circ/\theta_v=10^\circ$  and the case  $\theta_s=60^\circ/\theta_v=60^\circ$ , where the former extends a range of  $20^\circ$  scattering angle (from  $160^\circ$  to  $180^\circ$ ) and the latter spreads  $120^\circ$  of  $\Theta$  (from  $60^\circ$  to  $180^\circ$ ). Therefore, a fixed resolution in relative azimuth angle might result in deficient or redundant representation of scattering angle dependence for certain combinations of  $\theta_s$  and  $\theta_v$ .

For the ABI aerosol retrieval algorithm, the atmospheric reflectance lookup table is generated aiming to achieve a fixed resolution ( $4^\circ$ ) in scattering angle for all the discrete combinations of  $\theta_s$  and  $\theta_v$  (there are 21 discrete values of  $\theta_s$  and 25  $\theta_v$ , a total of 525 combinations). Since the range of scattering angle varies for different ( $\theta_s$ ,  $\theta_v$ ), instead of being arranged as a rectangular array where extra space will be wasted, the reflectance entries (corresponding to a given aerosol model, aerosol optical depth, and wavelength) are organized as a one-dimensional array. Within the array, there are 525 blocks corresponding to the individual pairs of ( $\theta_s^i$ ,  $\theta_v^j$ ). The sequence of blocks is ordered by looping over the viewing zenith angle first ( $j=1, 25$ ) then followed by the solar zenith angle ( $i=1, 21$ ). Each block contains a varying number of reflectance entries with scattering angles separated by  $4^\circ$  from  $\Theta_{\max}$  to  $\Theta_{\min}$  (the last interval might be larger than  $4^\circ$  if  $\Theta_{\max}-\Theta_{\min}$  is not an integer multiple of  $4^\circ$ ). There are a total of 7506 reflectance entries pre-calculated to represent the angular dependence of atmospheric reflectance. In order to find the block corresponding to a given ( $\theta_s^i$ ,  $\theta_v^j$ ), an indexing vector with 525 elements is created to save the starting position of each block within the reflectance array. Figure 3-10 shows the layout of the atmospheric reflectance array and indexing vector, and the way the starting position of each block is accessed.

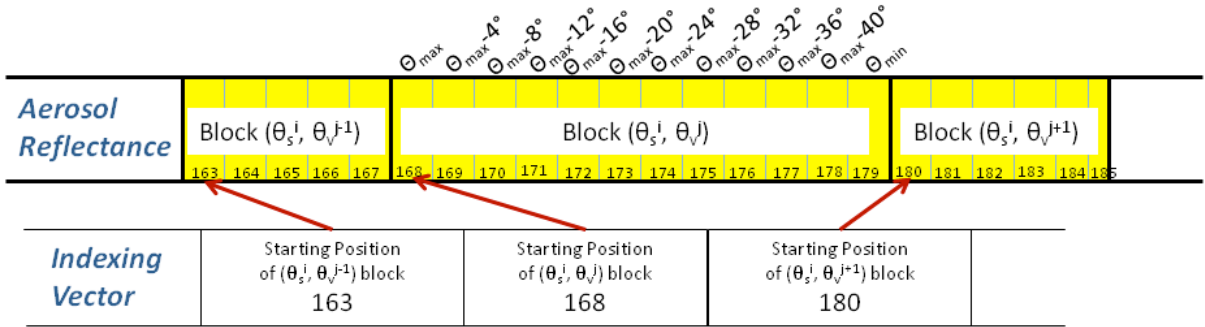


Figure 3-10. The layout of atmospheric reflectance array for a given aerosol model, aerosol optical depth and wavelength (top) and indexing vector (bottom). The starting position of each block can be accessed by the corresponding element in the indexing vector.

In the ABI aerosol retrieval, atmospheric reflectance corresponding to a given aerosol model, aerosol optical depth, wavelength and geometry ( $\theta_s$ ,  $\theta_v$  and  $\varphi$ ) is determined by linear interpolation on the values stored in the lookup table. The interpolation on geometry is implemented as follows:

1. The solar zenith angle bracket  $[\theta_s^{i-1}, \theta_s^i]$  containing  $\theta_s$  and the linear interpolation fraction  $f_s$  are determined such that  $\theta_s = f_s * \theta_s^{i-1} + (1 - f_s) * \theta_s^i$ .
2. The viewing zenith angle bracket  $[\theta_v^{j-1}, \theta_v^j]$  containing  $\theta_v$  and the linear interpolation fraction  $f_v$  are determined such that  $\theta_v = f_v * \theta_v^{j-1} + (1 - f_v) * \theta_v^j$ .
3. For each pair of  $(\theta_s^{i-1}, \theta_v^{j-1})$ ,  $(\theta_s^{i-1}, \theta_v^j)$ ,  $(\theta_s^i, \theta_v^{j-1})$ , and  $(\theta_s^i, \theta_v^j)$ , atmospheric reflectance corresponding to the instantaneous relative azimuth angle  $\varphi$  is interpolated from the reflectance array stored in the lookup table. For example, for the pair of  $(\theta_s^i, \theta_v^j)$ :
  - a. The corresponding position ( $k$ ) in the indexing vector is determined by  $k = i * n_v + j$ , where  $n_v$  is the number of tabulated viewing zenith angles ( $=25$ ), and the array index is assumed to start from zero following the convention in the C programming language. Therefore, the starting position of the block is read out from the  $k^{\text{th}}$  element of the indexing vector, and the number of entries in this block is determined by the difference between the  $(k+1)^{\text{th}}$  and  $k^{\text{th}}$  elements. The block of pre-calculated reflectances corresponding to the scattering angles from  $\Theta_{\text{max}}$  to  $\Theta_{\text{min}}$  for the current zenith angle pair are then extracted from the reflectance array.
  - b. The scattering angle  $\Theta$  corresponding to the measurement relative azimuth angle  $\varphi$  is calculated from

$$\cos\Theta = -\cos\theta_s^i * \cos\theta_v^j - \sin\theta_s^i * \sin\theta_v^j * \cos\varphi$$

Linear interpolation is performed to calculate the atmospheric reflectance  $\rho_{i,j}$  of the scattering angle  $\Theta$  from the block of reflectance.

4. With the four atmospheric reflectances  $\rho^{i-1,j-1}$ ,  $\rho^{i-1,j}$ ,  $\rho^{i,j-1}$ , and  $\rho^{i,j}$  corresponding to the four pairs of tabulated bracket zenith angles, instantaneous atmospheric reflectance is then estimated as:

$$\rho = f_s * f_v * \rho^{i-1,j-1} + f_s * (1-f_v) * \rho^{i-1,j} + (1-f_s) * f_v * \rho^{i,j-1} + (1-f_s) * (1-f_v) * \rho^{i,j}$$

### 3.4.5.2 Ocean surface reflectance look-up table

The ocean surface reflectance LUT is to account for its BRDF effect and to store the quantities needed for the analytical coupling of the atmosphere with the surface. Table 3-15 lists the contents of LUT, the corresponding discrete values for each dimension are listed in Table 3-16. There is no entry for wind direction as it is considered fixed at westerly direction.

Table 3-15. Contents of ocean surface reflectance look-up table

Data Set Name	Description	Size of Dimensions
rhobar	Ocean surface diffuse reflectance $\overline{\rho_{sgt}}$ which represents the portion of downwelling atmospheric diffuse radiation reflected upward direct to the satellite sensor	(9,20,4,21,21,40,4) (Nwataer,Ntau,Nwatchn,Nsolzen,Nsenzen,Nrelazi,Nwpd)
sgalb	Ocean surface spherical albedo $\overline{\rho_{sgt}}$	(4,4) (Nwatchn, Nwpd)

Table 3-16. Discrete values of ocean reflectance LUT dimensions

Dimension Name	Variable Name in Table 3-15	Number of Values	Discrete Values
Relative Azimuth Angle	Nrelazi	40	0°, 9°, 18°, 27°, 36°, 45°, 54°, 63°, 72°, 81°, 90°, 99°, 108°, 117°, 126°, 135°, 144°, 153°, 162°, 171°, 180°, 189°, 198°, 207°, 216°, 225°, 234°, 243°, 252°, 261°, 270°, 279°, 288°, 297°, 306°, 315°, 324°, 333°, 342°, 351°
Zenith angle	Nsolzen Nsenzen	21	0°, 4°, 8°, 12°, 16°, 20°, 24°, 28°, 32°, 36°, 40°, 44°, 48°, 52°, 56°, 60°, 64°, 68°, 72°, 76°, 80°
Wind speed (m/s)	Nwpd	4	1.0, 4.0, 6.0, 12.0

### 3.4.5.2.1 Ocean surface reflectivity

The ocean surface sunglint diffuse reflectances  $\overline{\rho_{sgt}}$ , representing the portion of downwelling atmospheric diffuse radiation reflected upward direct to the satellite sensor, are provided for each ocean aerosol model and optical depth for the channels used in the retrieval. The dependence on geometry and surface roughness of the reflectance is represented by the extra dimensions of solar/sensor zenith angle, relative azimuth angle and wind speed. Linear interpolation on these dimensions is used to estimate the  $\overline{\rho_{sgt}}$  for any given illumination and observation geometry and surface wind speed.

With the assumption of reciprocity principle, the ocean surface diffuse reflectance  $\overline{\rho'_{sgt}}$ , representing the portion of downwelling atmospheric direct radiation reflected diffusely skyward to the satellite sensor, can be regarded as  $\overline{\rho_{sgt}}$  with exchanged solar zenith ( $\theta_s$ ) and sensor zenith ( $\theta_v$ ) angles, i.e.,  $\overline{\rho'_{sgt}}(\theta_s, \theta_v) = \overline{\rho_{sgt}}(\theta_v, \theta_s)$ . Consequently,  $\overline{\rho'_{sgt}}$  at any given geometry and wind speed is determined via the interpolation of the  $\overline{\rho_{sgt}}$  LUT by switching the zenith angles.

### 3.4.5.2.2 Ocean surface spherical albedo

The ocean surface sunglint spherical albedo ( $\overline{\overline{\rho_{sgt}}}$ ) LUT is to account for the diffuse downwelling radiation that is scattered diffusely upward to the satellite sensor. It is assumed to be independent of the atmosphere and therefore only a function of surface wind speed and spectral channels. There is no interpolation involved with this parameter.

## 3.4.6 Gas transmittance parameterization

To simplify the radiative transfer model in the aerosol retrieval, the transmission of gases is parameterized as an analytical function of the effective absorber amount. The choice of analytical functions is guided by the JPSS/VIIRS aerosol algorithm. The coefficients appearing in the analytical expressions are determined for the ABI bands by applying a non-linear least squares fit to transmittances calculated by a line-by-line RTM to include continuum absorption for water vapor and ozone, and by the 6S RTM for the rest of the gases (O<sub>3</sub>, O<sub>2</sub>, CO<sub>2</sub>, N<sub>2</sub>O). In the line-by-line RTM calculation, 46 atmospheric profiles from ECWMF are utilized to cover various atmospheric conditions; while in the 6S calculation, the profiles of temperature and pressure in the standard mid-latitude summer atmosphere are used.

The analytical functions are fitted with the path absorber amount and channel-dependent coefficients  $C$ . The path absorber amount is the product of the column absorber amount  $u$

and the air mass  $M$  for water vapor and ozone, while it is simply  $M$  for the other gases due to the constant content. The column water vapor and ozone amounts are supplied as inputs to the algorithm. The air mass  $M$  is

$$M = \frac{1}{\cos(\theta_s)} + \frac{1}{\cos(\theta_v)}, \quad (3.4.26)$$

where  $\theta_s$  and  $\theta_v$  are solar and local zenith angles, respectively. The fitting ranges are  $2 \leq M \leq 20$  for both downward and upward paths, approximating the solar and local zenith angles of  $0 \sim 85^\circ$ .

The transmission for water vapor is expressed as

$$T_\lambda^{H_2O} = \exp[C_{1,\lambda}^{H_2O} Mu_{H_2O} + C_{2,\lambda}^{H_2O} \ln(Mu_{H_2O}) + C_{3,\lambda}^{H_2O} Mu_{H_2O} \ln(Mu_{H_2O})], \quad (3.4.27)$$

where  $T_\lambda^{H_2O}$  is the water vapor transmission at a given wavelength,  $u_{H_2O}$  is the column water vapor amount in unit cm, and  $C_{i,\lambda}^{H_2O}$  are band-dependent coefficients. The reasonable fitting range for total precipitable water vapor is  $0 \sim 40$  cm. The relative fitting accuracy (fitted-calculated transmittance divided by calculated transmittance) is generally within  $\sim 1\%$  for all channels as shown in Figure 3-11.

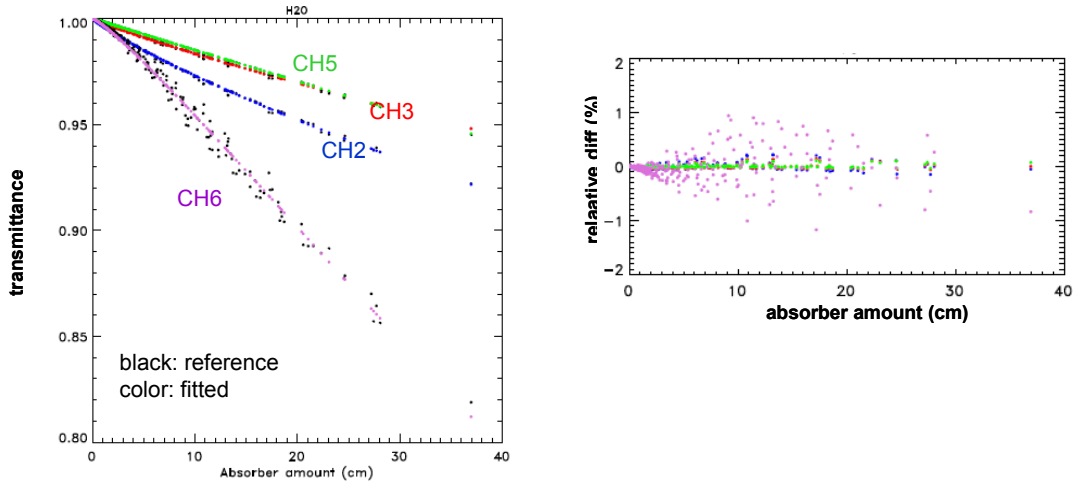


Figure 3-11. Fitting water vapor transmission (left, where original data in black and fitted data in color) and relative difference in percentage between fitted and original transmission (right) with absorber amount for ABI channels 2, 3, 5, and 6.

Similarly, ozone transmission is calculated as

$$T_\lambda^{O_3} = \exp(-Mu_{O_3} C_\lambda^{O_3}), \quad (3.4.28),$$

where the  $u_{O_3}$  is the input column ozone amount in unit atm-cm. This function is fitted for ozone content range of  $0 \sim 600$  Dobson units. The relative fitting accuracy is again within  $\sim 1\%$ .

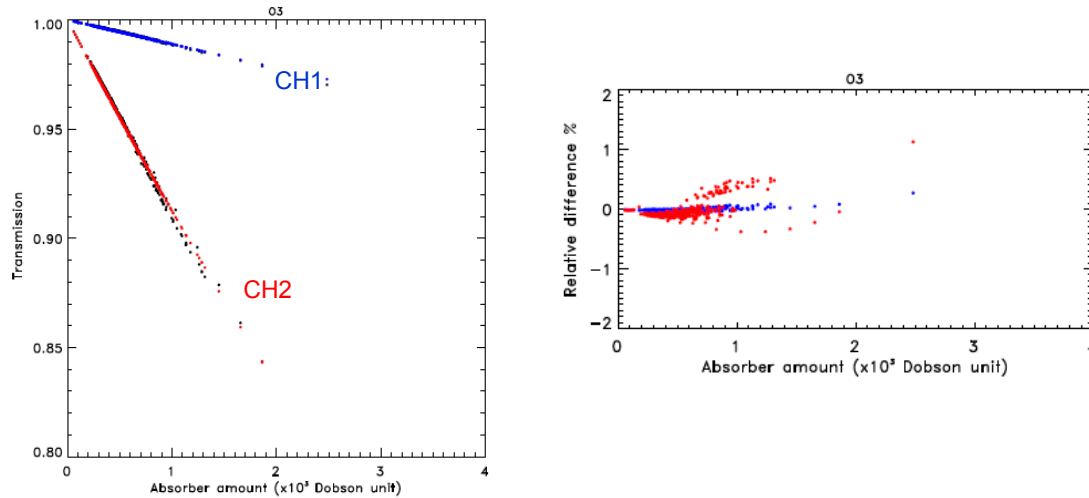


Figure 3-12. Left: Fit of ozone transmission (where original data are in black and fitted data are in color). Right: Relative difference in percentage between fitted and original transmission with absorber amount for ABI channels 1 and 2.

The transmission by gases other than water vapor and ozone, including O<sub>2</sub>, CO<sub>2</sub>, N<sub>2</sub>O, and CH<sub>4</sub>, is modeled as

$$T_{\lambda}^{gas_i} = 1.0 + C_{1,\lambda}^{gas_i} \times \left( M \times \frac{P}{P_0} \right)^{C_{2,\lambda}^{gas_i}}, \quad (3.4.29)$$

where  $gas_i$  represents O<sub>2</sub>, CO<sub>2</sub>, N<sub>2</sub>O, and CH<sub>4</sub> respectively,  $M$  is air mass, and applied with a surface pressure adjustment (ratio of actual  $P$  to standard surface pressure  $P_0 = 1013$  mb). The relative accuracies of fitting for the other gases are well within 1%. Table 3-17 lists the fitting coefficients for corresponding ABI channels. Note that no value is provided when a specific gas does not contribute to absorption in a channel (i.e. when  $T=1$ ).

The total transmittance by the other gases in Eqs. (3.4.3), (3.4.4), and (3.4.17) is calculated as:

$$T_{\lambda}^{og} = T_{\lambda}^{O_2} \times T_{\lambda}^{CO_2} \times T_{\lambda}^{N_2O} \times T_{\lambda}^{CH_4} \quad (3.4.30)$$

Table 3-17. Gas absorption fitting coefficients

ABI channel (wavelength: $\mu\text{m}$ )	$C_{1,\lambda}^{H_2O}$	$C_{2,\lambda}^{H_2O}$	$C_{3,\lambda}^{H_2O}$	$C_{\lambda}^{O_3}$	$C_{1,\lambda}^{O_2}$	$C_{2,\lambda}^{O_2}$	$C_{1,\lambda}^{CO_2}$	$C_{2,\lambda}^{CO_2}$	$C_{1,\lambda}^{CH_4}$	$C_{2,\lambda}^{CH_4}$	$C_{1,\lambda}^{N_2O}$	$C_{2,\lambda}^{N_2O}$
1 (0.47)				0.0111								
2 (0.64)	-0.0036	-5.28e-05	0.0004	0.0916	-0.0043	0.4386						
3 (0.865)	-0.0020	-3.28e-05	0.0002		-1.97e-05	0.8745						
5 (1.61)	-0.0015	-8.07e-06	-1.53e-05				-0.0187	0.6292	-0.0027	0.8140		
6 (2.25)	-0.0030	-1.25e-05	-0.0007						-0.0392	0.6884	-0.0027	0.8369

### 3.4.7 Calculation of molecular atmospheric functions

Molecular scattering is important in the radiative transfer computation and satellite remote sensing especially in the blue spectral range. Since the blue channel is the reference (primary) channel for aerosol retrieval over land, variation of molecular reflectance and transmission need to be incorporated in an accurate and efficient manner. Instead of expanding the lookup table with an extra dimension on surface pressure, analytical formulas [Vermote and Tanré, 1992] are used in the ABI aerosol retrieval algorithm to compute molecular scattering, and to adjust the atmospheric functions pre-calculated at standard pressure to local conditions. With the contribution of polarization being implicitly considered, the analytical expressions were shown to be valid for a large range of observation conditions.

Molecular reflection is calculated as the sum of single-scattering contribution and the correction for higher orders of scatterings. The relevant formulas are from subroutine CHAND for Rayleigh scattering function in the 6S code [E. F. Vermote, D. Tanré, J. L. Deuzé, M. Herman, J. J. Morcrette, S. Y. Kotchenova, and T. Miura, Second Simulation of the Satellite Signal in the Solar Spectrum (6S), 6S User Guide Version 3 (November, 2006), <http://www.6s.ltdri.org>]. According to these the Rayleigh (molecular) reflectance  $\rho_R$  corresponding to the cosines of solar and local zenith angles,  $\mu_s$  and  $\mu_v$ , azimuth angles  $\phi_s$ ,  $\phi_v$  and the Rayleigh optical depth  $\tau$  is computed as:

$$\rho_R = \sum_{m=0}^2 (2 - \delta_{0,m}) \times \rho_1^m(\mu_s, \mu_v, \tau) \times \cos[m(\pi - (\phi_v - \phi_s))] + \left(1 - e^{-\tau/\mu_s}\right) \times \left(1 - e^{-\tau/\mu_v}\right) \times \sum_{m=0}^2 (2 - \delta_{0,m}) \times \Delta^m(\tau) \times P^m(\mu_s, \mu_v) \times \cos[m(\pi - (\phi_v - \phi_s))] \quad (3.4.31)$$

Here  $\delta_{0,s}$  is the Kronecker delta,  $\rho_1^m(\mu_s, \mu_v, \tau)$  is the single-scattering reflectance corresponding to the  $m^{\text{th}}$  term of the phase function. The first three single-scattering reflectance terms ( $m=0, 1, 2$ ) are:

$$\rho_1^m(\mu_s, \mu_v, \tau) = P^m \times \left(1 - e^{-\tau \left(\frac{1}{\mu_s} + \frac{1}{\mu_v}\right)}\right) \times \frac{1}{4(\mu_s + \mu_v)} \quad (3.4.32)$$

The first three terms of the Fourier series expansion of the Rayleigh phase function  $P^m$  ( $m=0,1,2$ ) appearing in the equations above are:

$$\begin{aligned}
 P^0 &= 1 + (3\mu_s^2 - 1)(3\mu_v^2 - 1) * \frac{1 - \frac{\delta}{2 - \delta}}{1 + 2\frac{\delta}{2 - \delta}} * \frac{1}{8} \\
 P^1 &= -\mu_s\mu_v(1 - \mu_s^2)^{1/2}(1 - \mu_v^2)^{1/2} * \frac{1 - \frac{\delta}{2 - \delta}}{1 + 2\frac{\delta}{2 - \delta}} * \beta * 1.5 \\
 P^2 &= (1 - \mu_s^2)(1 - \mu_v^2) * \frac{1 - \frac{\delta}{2 - \delta}}{1 + 2\frac{\delta}{2 - \delta}} * \beta * 0.375
 \end{aligned} \tag{3.4.33}$$

Here  $\delta$  is the depolarization factor set to 0.0279, and the  $\beta$  factor equals to 0.5.

The Rayleigh optical depth  $\tau$  is calculated as  $\tau = \tau_0 * \frac{P}{P_0}$ , where  $\tau_0$  is the Rayleigh optical depth at standard surface pressure  $P_0$  (Table 3-18), and  $P$  is the local actual pressure.  $\tau_0$  is pre-calculated using the 6S subroutine ODRAYL and the ABI spectral response function for standard pressure and temperature profiles.

Adjustment of optical depth  $\Delta^s(\tau)$  corresponding to the multiple scattering term is approximated as:

$$\Delta^s(\tau) = a^s + b^s \ln(\tau) \tag{3.4.34}$$

Where

$$a^0 = a_0^0 + a_1^0(\mu_s + \mu_v) + a_2^0\mu_s\mu_v + a_3^0(\mu_s^2 + \mu_v^2) + a_4^0(\mu_s\mu_v)^2,$$

$$\{a_n^0\}_{n=0,1,\dots,4} = \{0.332438, 0.162854, -0.309248, -0.103244, 0.114933, \}$$
 and

$$b^0 = b_0^0 + b_1^0(\mu_s + \mu_v) + b_2^0\mu_s\mu_v + b_3^0(\mu_s^2 + \mu_v^2) + b_4^0(\mu_s\mu_v)^2,$$

$$\{b_n^0\}_{n=0,1,\dots,4} = \{-6.7771(10^{-2}), 1.577(10^{-3}), -1.2409(10^{-2}), 3.2417(10^{-2}), -3.5037(10^{-2})\}.$$

and  $a^1 = 0.19666$ ,  $a^2 = 0.145459$ ;  $b^1 = -0.054391$ ,  $b^2 = -0.029108$ .

Table 3-18. Rayleigh optical depth at standard surface pressure for the ABI channels

ABI Channel (wavelength: $\mu\text{m}$ )	$\tau_0$
1 (0.47)	0.1851

2 (0.64)	0.0549
3 (0.86)	0.0155
5 (1.61)	0.0013
6 (2.25)	0.0003

The Rayleigh reflectance  $\rho_R$  is calculated at the actual surface pressure and at the standard pressure, respectively, and used in Eq. (3.4.3) in Section 3.4.1.3. The dependence on pressure is realized through the Rayleigh optical depth  $\tau$  that enters in the calculation of the Rayleigh reflectance.

The Rayleigh transmission  $T_R(\mu)$  and spherical albedo  $S_R$  are used to correct the optical functions stored in the LUT to the local pressure, which are computed at standard surface pressure. Specifically, the LUT transmissions  $T_{R+A}^\downarrow$  and  $T_{R+A}^\uparrow$  in Eq. (3.4.4) and in Eq. (3.4.17) need to be multiplied by the ratio of Rayleigh transmission  $T_R(\mu)$  at actual pressure to that at standard pressure; the LUT spherical albedo  $S_{R+A}$  in Eq. (3.4.4) and in Eq. (3.4.17) is corrected by adding the difference between the Rayleigh spherical albedo  $S_R$  at actual pressure and that at standard pressure. The pressure correction is realized through the Rayleigh optical depth  $\tau$ .

The analytical expression of Rayleigh transmission function is based on the two-stream method,

$$T_R(\mu) = \frac{[\frac{2}{3} + \mu] + [\frac{2}{3} - \mu]e^{-\tau/\mu}}{\frac{4}{3} + \tau} \quad (3.4.35)$$

where  $\mu$  is the cosine of the solar/view zenith angle for downward/upward transmittance, respectively.

For conservative molecular scattering, the spherical albedo  $S$  is given by:

$$S_R = \frac{1}{4 + 3\tau} [3\tau - 4E_3(\tau) + 6E_4(\tau)] \quad (3.4.36)$$

where  $E_n$  is the exponential integral ( $E_n(x) = \int_1^\infty \frac{e^{-xt}}{t^n} dt$ ). The exponential integral is estimated as:

$$E_1(\tau) = \sum_{i=0}^5 c_i \tau^i - \ln \tau, \quad (3.4.37)$$

where  $\tau$  is the Rayleigh optical depth, coefficients  $c_i = -0.57721566, 0.99999193, -0.24991055, 0.5519968, -0.00976004, 0.00107857$  for  $i=0$  to  $5$ . The recurrence relation is used to calculate  $E_n(x)$  for  $n>0$ :

$$E_{n+1}(\tau) = \frac{1}{n}(e^{-\tau} - \tau E_n(\tau)). \quad (3.4.38)$$

### 3.4.8 Algorithm output

The final output of this algorithm includes aerosol optical depth, aerosol type, particle size parameter, and suspended matter mass concentration. Aerosol type is an intermediate product, but used by the GOES-R Shortwave Radiation Budget (SRB) algorithm. The parameters are given below in Table 3-19 . The overall quality flag is set to ‘Bad’ when the retrieval fails, beyond the F&PS specified value range, or at large local zenith angle (> 60°) or large solar zenith angle (> 80°).

Table 3-19 . ABI aerosol algorithm output

Name	Type	Description	Dimension
AOD at 550nm	output	Retrieved aerosol optical depth at 550 nm	Grid (xsize, ysize)
AOD in ABI channels	output	Retrieved aerosol optical depth in ABI channels 1,2,3,5,6	Grid (xsize, ysize) x 5
Particle size	output	Ångström Exponents (proxy for particle size) calculated from AOD at two pairs of wavelengths (0.47,0.86 μm and 0.86,2.25 μm)	Grid (xsize, ysize) x 2
Suspended matter mass concentration	output	Column aerosol mass	Grid (xsize, ysize)
Overall QC flag	output	Overall quality flag for aerosol retrieval: 0: good 1: bad	Grid (xsize, ysize)
Detailed QC flags	output	Detailed input and output quality and critical path flags (see Table 3-20)	Grid (xsize, ysize)
Aerosol type ID	intermediate	Aerosol model selected from prescribed models during the retrieval; 0: oceanic aerosol; 1: dust over land; 2: generic aerosol over land; 3: urban aerosol over land; 4: smoke over land.	Grid (xsize, ysize)
Fine mode aerosol index	diagnostic	Index of fine mode aerosol model over ocean	Grid (xsize, ysize)
Coarse mode aerosol index	diagnostic	Index of coarse mode aerosol model over ocean	Grid (xsize, ysize)
Fine mode weight	diagnostic	Fine mode weight over ocean	Grid (xsize, ysize)

Land surface reflectance	diagnostic	Surface reflectance of land retrieved in three channels (1,2 and 6)	Grid (xsize, ysize) x 3
--------------------------	------------	---	-------------------------

Table 3-20 Detailed input and output quality and critical path flags

Byte	Bits	Quality Flag Name	Meaning
1: Input Geometry Quality Flag: QCInputGeo	0	QC_INPUT_LON	0: valid longitude (-180 - 180°) 1: out-of-range longitude
	1	QC_INPUT_LAT	0: valid latitude (-90 - 90°) 1: out-of-range latitude
	2	QC_INPUT_ELEV	0: valid elevation (-2000 – 10,000 m) 1: out-of-range elevation
	3	QC_INPUT_SOLZEN	0: valid solar zenith (0 - 90°) 1: out-of-range solar zenith
	4	QC_INPUT_SATZEN	0: valid satellite zenith (0 - 90°) 1: out-of-range satellite zenith
	5	QC_INPUT_SOLAZI	0: valid solar azimuth (-180 - 180°) 1: out-of-range solar azimuth
	6	QC_INPUT_SATAZI	0: valid satellite azimuth (-180 - 180°) 1: out-of-range satellite azimuth
2: Input Ancillary Data Flag: QCInputAnc	0	QC_INPUT_TPW_ABI	0: TPW data from ABI retrieval 1: TPW data not from ABI retrieval
	1	QC_INPUT_TPW_MODEL	0: TPW data from model 1: TPW data not from model
	2	QC_INPUT_OZONE_ABI	0: ozone data from ABI retrieval 1: ozone data not from ABI retrieval
	3	QC_INPUT_OZONE_MODEL	0: ozone data from model 1: ozone data not from model
	4	QC_INPUT__PRES	0: valid model surface pressure (500 – 1500 mb) 1: constant surface pressure (1013 mb)
	5	QC_INPUT_HGT	0: valid model surface height (-2 – 10 km) 1: constant surface height (0 km)
	6	QC_INPUT_WSP	0: valid model surface wind speed (0 – 100 m/s) 1: constant surface wind speed (6 m/s)
	7	QC_INPUT_WDR	0: model surface wind direction (0° - 360°) 1: fixed surface wind direction (90°)
3: Input Reflectance Data Flag: QCInputRef	0	QC_INPUT_REFL_CH1	0: valid ABI reflectance in band 1 (0 – 1) 1: out-of-range ABI reflectance in band 1
	1	QC_INPUT_REFL_CH2	0: valid ABI reflectance in band 2 (0 – 1) 1: out-of-range ABI reflectance in band 2
	2	QC_INPUT_REFL_CH3	0: valid ABI reflectance in band 3 (0 – 1) 1: out-of-range ABI reflectance in band 3

	3	QC_INPUT_REFL_CH5	0: valid ABI reflectance in band 5 (0 – 1) 1: out-of-range ABI reflectance in band 5
	4	QC_INPUT_REFL_CH6	0: valid ABI reflectance in band 6 (0 – 1) 1: out-of-range ABI reflectance in band 6
4: Critical Path Flag: QCPath	0	QC_CLOUD_MASK	0: clear sky 1: cloudy sky
	1	QC_RET_SCENE	0: over-land algorithm is used 1: over-water algorithm is used
	2	QC_LAND_TYPE	0: vegetation 1: soil
	3	QC_LAND_BRISFC	0: dark surface 1: bright surface
	4	QC_LAND_SNOW	0: no snow contamination 1: with snow contamination
	5	QC_WATER_GLINT	0: no sunglint contamination 1: with sunglint contamination
	6	QC_WATER_TURBID	0: no turbid water contamination 1: with turbid water contamination
5: AOD Product Quality Flag: QCAOD	0	QC_RET	0: AOD is retrieved 1: AOD is not retrieved
	1	QC_RET_EXTRP	0: interpolation within LUT AOD range 1: extrapolation of AOD used
	2	QC_OUT_SPEC	0: within F&PS specification range 1: out of F&PS specification range
	3	QC_LOWSUN	0: solar zenith angle not larger than 80° 1: solar zenith angle larger than 80°
	4	QC_LOWSAT	0: local zenith angle not larger than 60° 1: local zenith angle larger than 60°

In addition, the following metadata information is included in the output:

- DateTime (swath beginning and swath end)
- Bounding Box
  - product resolution (nominal and/or at nadir)
  - number of rows and
  - number of columns,
  - bytes per pixel
  - data type
  - byte order information
  - location of box relative to nadir (pixel space)
- Product Name

- Product Units
- Ancillary Data to Produce Product (including product precedence and interval between datasets is applicable)
  - Version Number
  - Origin (where it was produced)
  - Name
- Satellite
- Instrument
- Altitude
- Nadir pixel in the fixed grid
- Attitude
- Latitude
- Longitude
- Grid Projection
- Type of Scan
- Product Version Number
- Data compression type
- Location of production
- Citations to Documents
- Contact Information
- Mean and standard deviation of AOD retrievals at 550nm and ABI channels 1, 2, 3, 5, 6 over land
- Mean and standard deviation of AOD retrievals at 550nm and ABI channels 1, 2, 3, 5, 6 over ocean
- Maximum and minimum AOD retrievals at 550nm and ABI channels 1, 2, 3, 5, 6 over land
- Maximum and minimum AOD retrievals at 550nm and ABI channels 1, 2, 3, 5, 6 over ocean
- For each QA flag value, the following information is required:
  - Percent of retrievals with the QA flag value
  - Definition of QA flag
- Total number of pixels where retrieval was attempted separately for land and ocean
- Number of pixels with local zenith angle less than 60 degrees
- For each 10° latitude zone and surface type:
  - Zonal min, max, mean and standard deviation of AOD at 550nm over land and ocean, respectively
  - Zonal min, max, mean and standard deviation of AOD at ABI channels 1, 2, 3, 5, 6 over land and ocean, respectively
  - Zonal min, max, mean and standard deviation of surface reflectivity at ABI channel 1, 2 and 6 over land
  - Geographic bounding box
  - For each QA flag value, the following information is required:
    - Percent of retrievals with the QA flag value
    - Definition of QA flag

- Total number of pixels where retrieval was attempted separately for land and ocean
- Number of pixels with local zenith angle less than 60 degrees

## 4 TEST DATA SETS AND OUTPUTS

### 4.1 Input Data Sets

Proxy clear-sky TOA reflectances in the ABI bands are needed for algorithm development and testing. Such data can be obtained from observations of existing satellites. For example, MODIS reflectances can be used because the spectral placement of the MODIS channels is similar to those of ABI (Table 4.1). The advantage of this approach is that the scenes are realistic. However, some of the MODIS channels do not exactly match the ABI channels so appropriate spectral transformations would be needed to convert the MODIS reflectances to ABI reflectances. Such conversions can only be derived from radiative transfer calculations for different (but a limited number of) atmospheric and surface conditions (scenes). These transformations are not expected to hold for all possible scenes encountered in real observations. One can avoid the spectral conversion if the band-dependent components of the algorithm (e.g. LUT) are built for the MODIS band. In this case, however, one is not fully testing the ABI algorithm. Another possibility for generating proxy reflectances is to simulate them with a radiative transfer model. The advantage is that one can “match” the ABI channels exactly, and the “true” AOD is also known. However, this approach can only offer a limited realism and because of its nature must be confined to specific, very limited scenes. A third possibility, which has been adopted for the ABI aerosol algorithm development, combines the best of the two approaches mentioned above. In this method, MODIS derived atmospheric (cloud mask, AOD, total column ozone and water vapor) and surface (8-day composite surface reflectance) properties are used with solutions of radiative transfer calculation represented in the form of LUT as described in the next section [Laszlo et al., 2007].

Table 4-1. Channel mapping between ABI and MODIS

ABI Channel	MODIS Channel
Channel 1: 0.47 $\mu$ m	Channel 3: 0.47 $\mu$ m
Channel 2: 0.64 $\mu$ m	Channel 1: 0.66 $\mu$ m
Channel 3: 0.86 $\mu$ m	Channel 2: 0.86 $\mu$ m
Channel 4: 1.38 $\mu$ m	Channel 26: 1.38 $\mu$ m
Channel 5: 1.61 $\mu$ m	Channel 6: 1.64 $\mu$ m
Channel 6: 2.26 $\mu$ m	Channel 7: 2.13 $\mu$ m

#### 4.1.1 Development of a fast simulator to simulate cloud-free ABI TOA reflectance

To simulate cloud-free radiance fields in six ABI bands, i.e., 0.47, 0.64, 0.865, 1.378, 1.61 and 2.25  $\mu\text{m}$ , a fast ABI simulator was developed. This scheme bypasses time-consuming RT calculations by using pre-calculated look-up tables and empirical relationships. Inputs required for the simulations, including bidirectional reflectance distribution function (BRDF) of land surface, aerosol optical depth and type, total amount of ozone and water vapor, are obtained from MODIS products. The advantage of this scheme lies in three aspects. First, it is designed to substantially reduce CPU time; for example, the computational time for one MODIS granule is reduced from about two weeks with direct 6S RT simulation to less than 10 minutes with the LUT with nearly 80% coverage of aerosol retrievals. Second, the speed of the fast scheme is not achieved at the cost of the accuracy, as the difference in TOA reflectance between the fast scheme and 6S RTM calculation is less than 3%. Third, the fast scheme applies to both land and ocean. In brief, the fast scheme is able to efficiently generate TOA radiance fields for developing and validating the aerosol retrieval algorithm, not only for an individual granule, but also for global coverage with sufficient accuracy. The flowchart of the fast simulator is shown in Figure 4-1.

#### **4.1.1.1 One MODIS/Terra granule for dust case over ocean**

As an example, reflectances simulated for four ABI channels (2, 3, 4 and 6) for one MODIS/Terra granule on September 30, 2002 over ocean are presented in Figure 4-2. The RGB image for this granule is also shown. This scene has scattered clouds mixed with small aerosol loading (AOD <0.5). This is also shown in the MODIS retrieved aerosol optical depth at 550 nm (top right in Figure 4-2), which is one of the inputs to the simulation scheme. The fine mode weight (another input) indicates that aerosols in this scene are dominated by fine mode. The map of wind speed shows that most parts of the scene have moderate roughness; however, high wind (up to 14 m/s) is seen in the upper-left corner of the granule and at the middle of the left edge, where slightly higher fine mode aerosol loading appears. Note that the black patch in the center of the simulated reflectance fields is the place where the sun glint angle is less than 40 and no retrieval was performed by the MODIS aerosol algorithm.

#### **4.1.1.2 Two MODIS/Aqua granules for smoke case over land**

Figure 4-3. shows simulations for two MODIS granules over land. One is from April 12, 2003 and the other is from May 16, 2007. Both cases contain smoke from wild fires. These can be seen in the RGB images. For the case on April 12, 2003, higher surface reflectance is indicated in TOA reflectance in Channel 6 as a result of lower vegetation coverage.

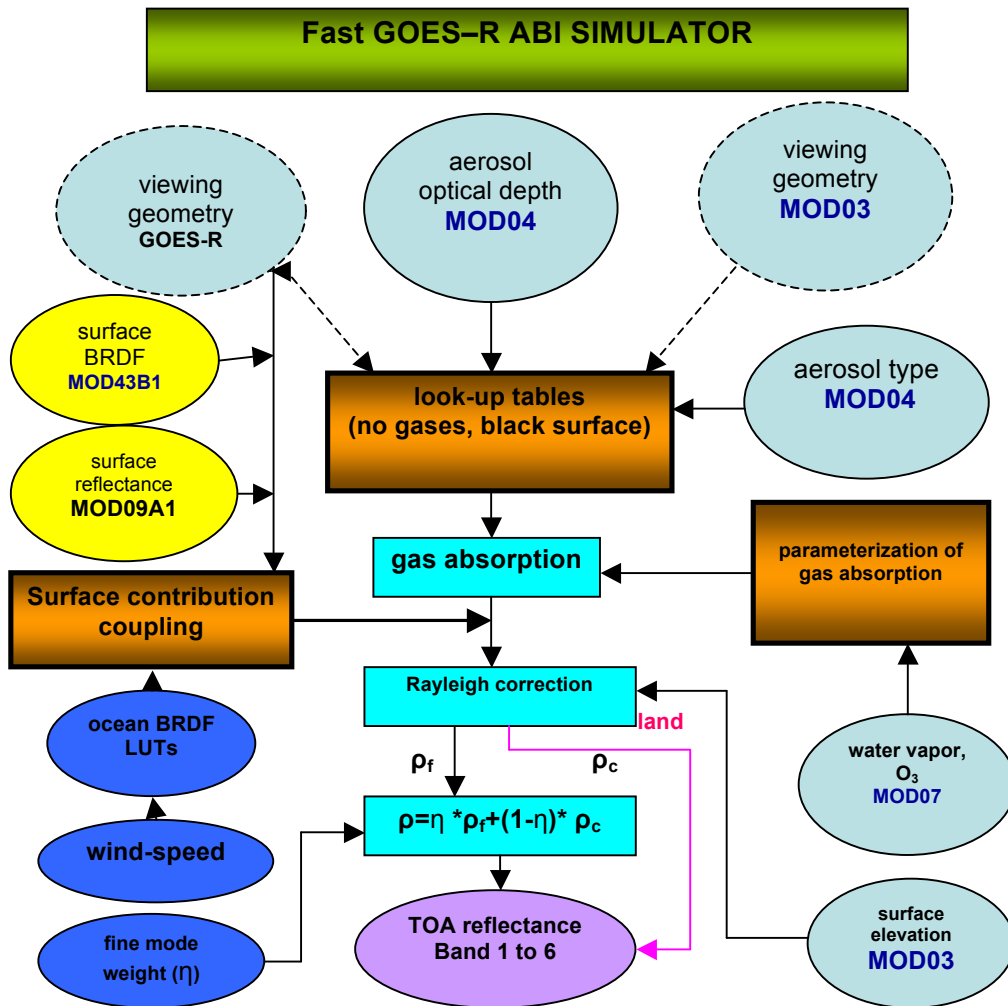


Figure 4-1. Flow chart of fast simulation scheme for GOES-R ABI radiance field.

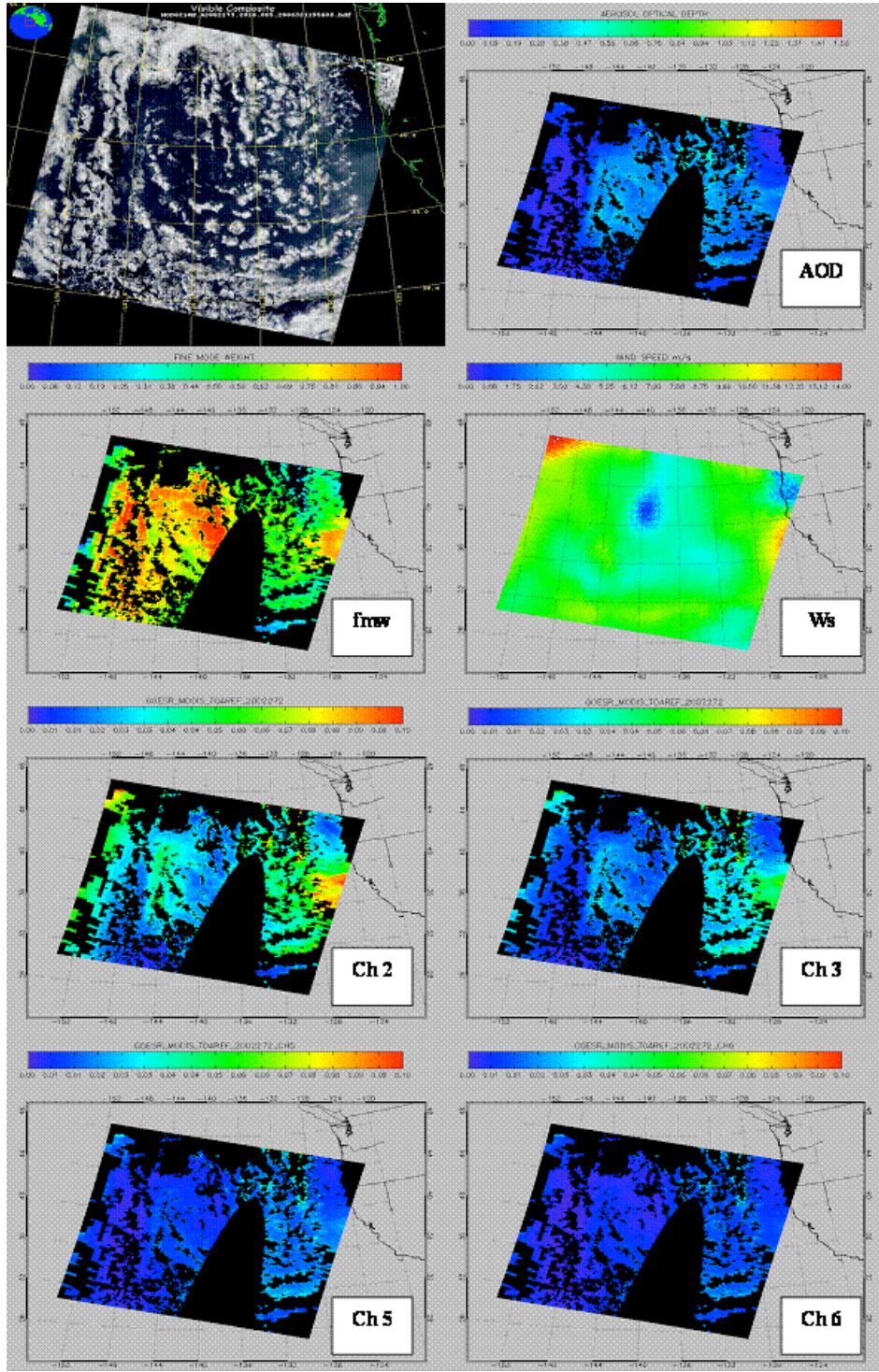


Figure 4-2. Example of ABI reflectances simulated from one MODIS/TERRA granule at UTC 20:10 on September 30 (day 273), 2002. Top left: RGB image; top right: AOD: aerosol optical depth at 550 nm; second row left: fine mode to coarse mode optical depth weight (FMW); second row right: wind speed; third and fourth rows: simulated for channel 2, 3, 5, and 6 reflectances.

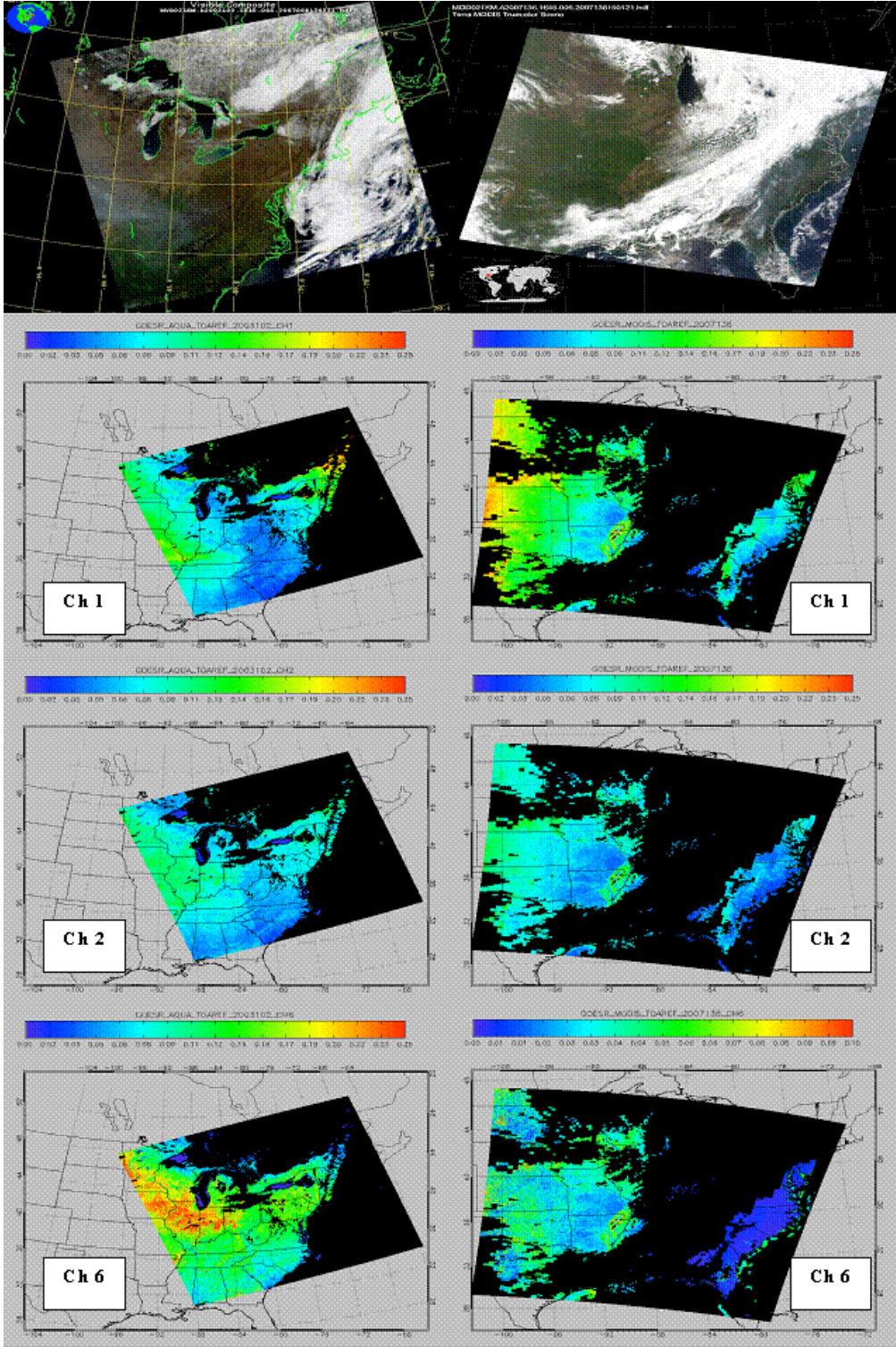


Figure 4-3. Reflectance fields simulated for MODIS/AQUA granules at UTC: 18:15 on April 12, 2003 (left panel) and at UTC 16:45 on May 16, 2007 (right panel). RGB images are shown in the top row.

### **4.1.2 MODIS radiance as proxy data sets**

In addition to proxy data from the fast simulator, clear-sky MODIS reflectances are also used as proxy data for algorithm development and evaluation. This is because the MODIS channels have spectral placement and width similar to those of ABI. For this, new LUTs specific to the MODIS channels and band passes were created using the 6S radiative transfer model. Cloud screening, dark land surface selection and quality assurance are performed following the MODIS scheme. Hereafter the ABI algorithm with direct inputs of MODIS products is referred to as the ABI/MODIS algorithm.

The ground-based remote sensing network, AEROSol Robotic Network (AERONET), equipped with well-calibrated sunphotometers over more than 100 sites throughout the world, measures and derives quality-assured aerosol optical properties for a wide diversity of aerosol regimes, for up to the last 10 years [Holben et al., 1998; 2001; Dubovik et al., 2002]. These high quality data have been widely used as ground “truth” for evaluation and validation of satellite remote sensing of aerosols [Yu et al., 2003; Remer et al., 2005].

AERONET version 2 level 2.0 data and MODIS collection 5 aerosol product for the years 2000-2009 (2000-2009 for Terra and 2002-2008 for Aqua) are collected, collocated and analyzed. The collocation follows the MODIS validation strategy [Ichoku et al., 2002; Remer et al., 2005], in which AERONET data is temporally averaged within a one-hour window around the MODIS overpass time and the MODIS data are spatially averaged in a 50x50 km box centered on the AERONET station. The MODIS reflectances used here are the gas-absorption corrected reflectances available in the MODIS aerosol product. Because of this, this procedure does not test calculation of the gas absorption implemented in the ABI aerosol algorithm.

## **4.2 Output Analysis from Input Data Sets**

### **4.2.1 Precisions and accuracy estimates**

The validation of the aerosol products compares satellite-retrieved AOD and ASP with reference (“truth”) values, and it involves calculation of certain metrics that characterize the level of agreement between the satellite retrievals and reference values. The reference data include (1) aerosol data used in the simulation of ABI radiances, and (2) measurements of aerosol properties made from the ground measurements. The primary means of validation is the comparison with the ground measurements made at the AERONET sites. Evaluation is also done by performing retrievals from model-simulated proxy ABI data, and by comparing the retrieved aerosol product to the known aerosol input used in the forward simulation. This type of validation is ideal for “deep-dive” evaluation of the algorithm because all relevant data are known from the simulations. It is, however, necessarily limited to scenes selected for simulation.

Performance of the ABI aerosol algorithm is measured by two metrics: precision and accuracy of the retrievals. AWG defines

- Accuracy as the mean difference (bias, systematic error) between the retrieved and reference “truth” values. The ABI retrievals and reference data should be appropriately averaged in space and time to avoid sampling issues.
- Precision is defined as the standard deviation of the differences between ABI and reference data representing the random error of ABI products.

In addition to the accuracy and precision other commonly used statistics, like the root mean square error (RMSE) of the differences and correlation between ABI and reference data, are also calculated. Histograms of the differences are also analyzed. The ABI aerosol products are considered validated if the overall accuracy and precision satisfy the requirements specified in the F&PS and MRD.

#### 4.2.1.1 Estimates using simulated input radiances

The ABI algorithm was tested with TOA reflectances simulated using the fast simulator described in Section 4.1.1. Figure 4-4. shows the comparison of ABI AOD and fine-mode weight (FMW) retrieved over ocean with reference values obtained from a MODIS granule over the North Pacific Ocean near the North American Continent on day 273 of 2002. A good agreement is seen with correlation coefficients 0.99 for both AOD and FW. The mean differences are 0.00017 and 0.00069, and standard deviations are 0.00043 and 0.00354 for AOD and FW, respectively. The analysis shows that the relatively large differences between the MODIS reference and ABI-retrieved FWs are associated either with relatively small optical depth ( $AOD \leq 0.1$ ) or with relatively large AOD retrieval error ( $ABI \text{ retrieval} - MODIS \text{ input } AOD > 0.02$ ).

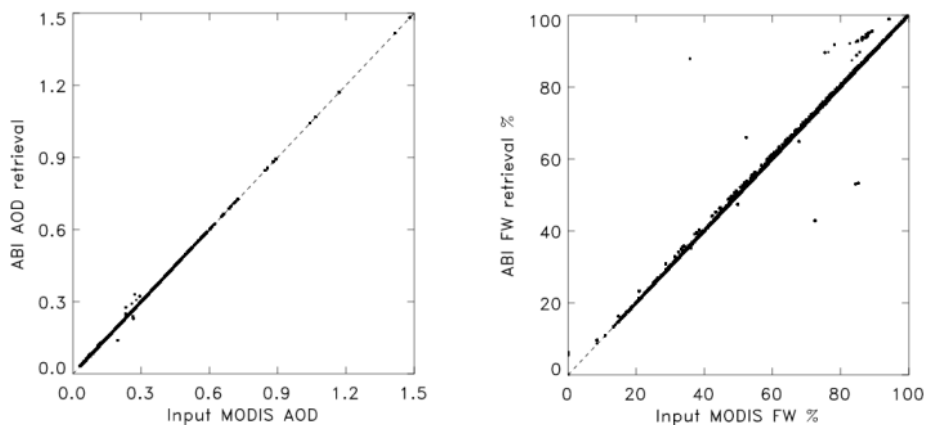


Figure 4-4. Comparison of AOD (left) and fine-mode weight (FW) in percentage (right) from the MODIS reference with those retrieved from the ABI algorithm for a selected test scene over ocean.

Figure 4-5 shows an example of validating AOD retrieved over land with MODIS input AOD used in the simulation for two days. As seen for May 16, 2007, the agreement is relatively good; the mean difference is only 0.0005 (~ 0.2% difference) and the standard deviation is 0.0006. However, for day April 12, 2002, the mean difference and RMS can be as large as 0.02 and 0.023 (~11% difference), respectively.

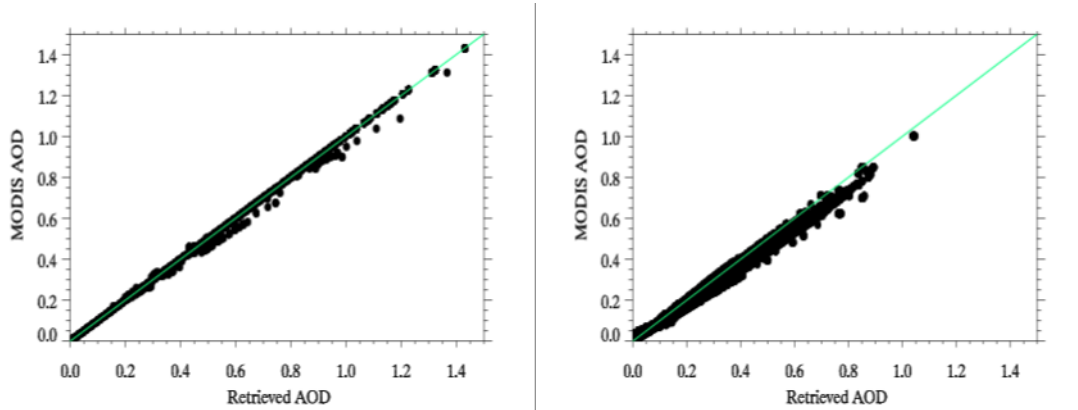


Figure 4-5. Comparison of retrieved and reference (MODIS) AOD for two MODIS granules: (left) May 16, 2007, (right) April 12, 2002.

#### 4.2.1.2 Estimates using MODIS reflectances

An extensive collocated MODIS-AERONET dataset for the years 2000-2009 are used for the retrieval of aerosol with the ABI algorithm and for the evaluation of the retrieved product. The gas-absorption-corrected “aerosol” reflectances in the MODIS aerosol product are used as proxy inputs to the ABI/MODIS aerosol algorithm. For the comparison with the ground measurements, the AERONET data at 550 nm are linearity interpolated between the 440- and 870-nm AOD values in log-log space. Note that the range of AOD reported in ABI, MODIS and AERONET are different. The ABI retrievals have a product measurement range for AOD of [-1.0, 5.0]. MODIS reports negative values up to -0.05, but over land only; it does not report negative values over water. AERONET do not allow negative values. Therefore the total number of samples used in the comparisons of ABI with reference data depends on whether the reference data are the MODIS retrievals or the AERONET values.

Table 4-2. and Table 4-3. show the overall statistics between ABI/MODIS AODs with AERONET measurements at 550 nm. Generally, ABI and MODIS statistics are comparable over land; the ABI bias is somewhat smaller over ocean, most likely due to using variable wind speed in the calculation of surface reflectance of water. Figure 4-6. and Table 4-4. show the accuracy and precision values for the different AOD ranges specified in the F&PS. The results indicate the AOD product meets the 100% F&PS requirements.

Table 4-2. AOD validation statistics over land obtained from the collocated AERONET-MODIS dataset for years 2000-2009. RMSE is the root mean square error. MinErr and MaxErr are minimum and maximum differences, respectively.

	Accuracy	Precision	RMSE	Correlation	MinErr	MaxErr
<b>ABI</b>	0.028	0.137	0.140	83.3%	-2.179	1.982
<b>MODIS</b>	0.027	0.124	0.127	87.2%	-1.889	3.331

Table 4-3. AOD validation statistics over ocean obtained from the collocated AERONET-MODIS dataset for years 2000-2009. RMSE is the root mean square error. MinErr and MaxErr are minimum and maximum differences, respectively.

	Accuracy	Precision	RMSE	Correlation	MinErr	MaxErr
<b>ABI</b>	0.008	0.091	0.091	87.0%	-1.014	2.546
<b>MODIS</b>	0.017	0.100	0.102	84.8%	-0.976	2.668

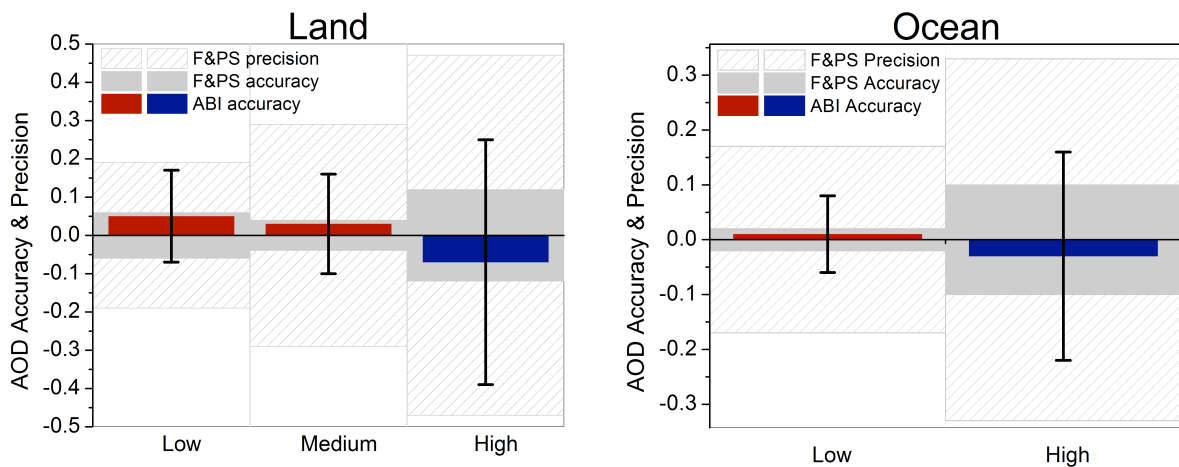


Figure 4-6. Comparison of ABI AOD with AERONET AOD at 550 nm over land (left) and over ocean (right) using collocated AERONET-MODIS dataset for years 2000-2009.

Table 4-4. Accuracy and precision of ABI AOD from comparison with AERONET AOD at 550 nm over land (left) and over water (right) using collocated AERONET-MODIS dataset for years 2000-2009. F&PS requirements are in parenthesis.

Range	Land				Ocean			
	AOD	Accuracy	Precision	# of points	AOD	Accuracy	Precision	# of points
Low	<0.04	0.05 (0.06)	0.12 (0.13)	18,100	<0.4	0.01 (0.02)	0.07 (0.15)	27,975
Medium	0.04 - 0.8	0.03 (0.04)	0.13 (0.25)	109,308				
High	> 0.8	-0.07 (0.12)	0.32 (0.35)	3,225	>0.4	-0.03 (0.10)	0.19 (0.23)	2592

Figure 4-7. displays the histogram of the Ångström Exponent (AE) derived from ABI, MODIS and AERONET. The distribution of ABI and MODIS AE are similar. Both show two peaks (~0.6 and ~1.7) over land. These peaks correspond to the assumed fine and coarse modes. The AERONET AE also peaks around 1.4 but it does not have a peak at the small AE. In contrast, over water, the AERONET AE has two peaks which are not captured well by either of the satellite retrievals. Nevertheless, the ABI Ångström Exponent retrievals meet the F&PS requirement of 0.3 for accuracy, as seen in

Table 4-5.. Neither of the satellite retrievals of AE meets the requirement for precision (0.15).

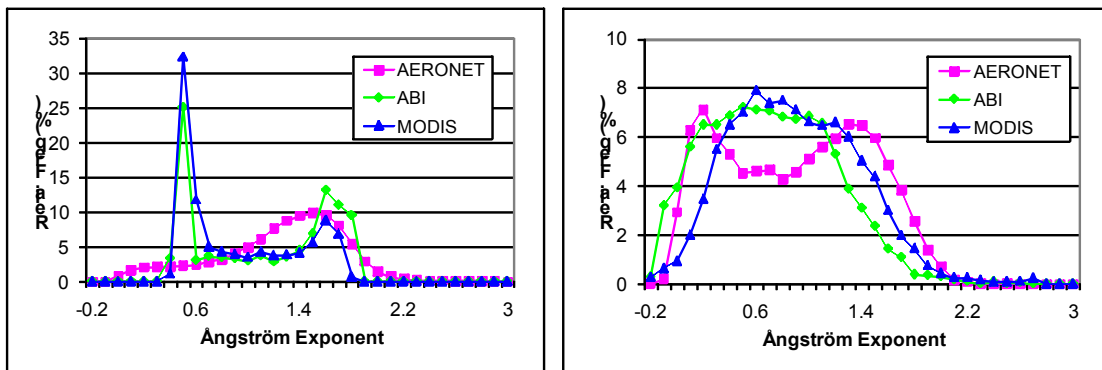


Figure 4-7. Comparison of ABI Ångström Exponent with AERONET over land (left) and over ocean (right) using collocated AERONET-MODIS dataset for years 2000-2009.

Table 4-5. Accuracy and precision of Ångström Exponent retrieval from collocated AERONET-MODIS dataset for years 2000–2009.

	Land		Water	
	Accuracy	Precision	Accuracy	Precision
<b>ABI</b>	-0.13	0.57	-0.20	0.40
<b>MODIS</b>	-0.33	0.53	-0.01	0.36

### 4.2.1.3 Framework validation using MODIS radiance

The aerosol algorithm validation discussed in Section 4.2.1.1 and 4.2.1.2 was conducted for the AWG’s science code. The science code is integrated into AIT’s Framework, and the AIT prepares the algorithm inputs for framework runs on 1-km resolution using MODIS reflectances as proxy data, which includes the L1b reflectance, geolocation data, cloud mask, water vapor and ozone from MODIS; and surface pressure, surface height, and surface wind speed/direction from NCEP.

One granule of MODIS data for 03:25 UTC on June 4, 2005 have been used to verify the implementation of the algorithm in AIT’s framework on a Linux machine within the collaborative environment. The results from the AIT and the AWG runs were compared and confirmed on a pixel by pixel basis (Figure 4-9.). The maximum difference is on the order of  $1.0E-6$  over land and  $1.0E-4$  over ocean, and the data with difference larger than  $1.0E-6$  is about  $\sim 0.015\%$ . The difference is believed to be the result of the different compilers used; AIT uses the Intel compiler, while AWG uses g++.

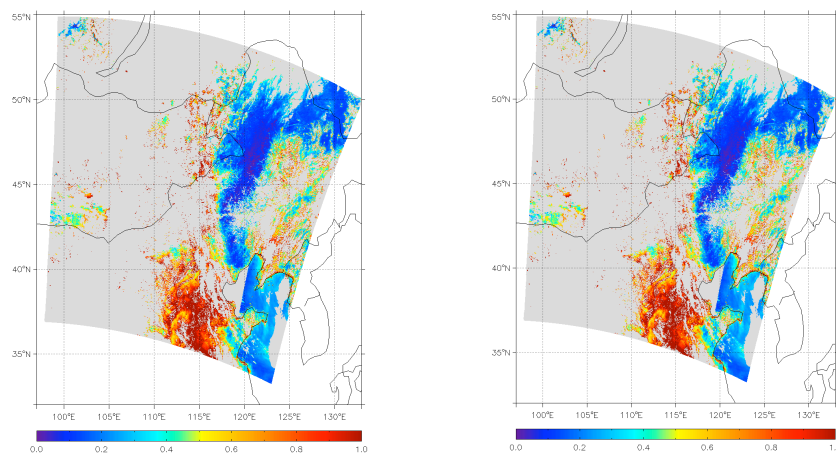


Figure 4-8. Aerosol optical depths at 550 nm, for one MODIS granule at 03:25 UTC on June 4, 2005, generated by the AIT framework run (left) and the AWG research code (right).

Currently data from two days (Aug. 24 and Aug. 25, 2006) are available for analysis. For the analysis of the framework results with AERONET, the AERONET data are averaged within a one-hour window and the collocated ABI estimates are spatially averaged for a  $50\text{km} \times 50\text{ km}$  region. Following the approach used in the offline validation, the highest 50% and lowest 20% of AODs in the  $50 \times 50\text{ km}$  boxes are screened out, and the rest are averaged for comparison with AERONET.

Figure 4-9. shows, as a scatter-plot, the comparison between ABI AODs with AERONET measurements at 550 nm over land and water. The overall statistics, including the accuracy, precision and correlation coefficients are presented. The data are also averaged over different AOD ranges to see the dependence of accuracy and precision on AOD as shown in Table 4-6.. Note that the match-up points from the two days are quite limited, especially over water, and the statistics cannot be considered representative.

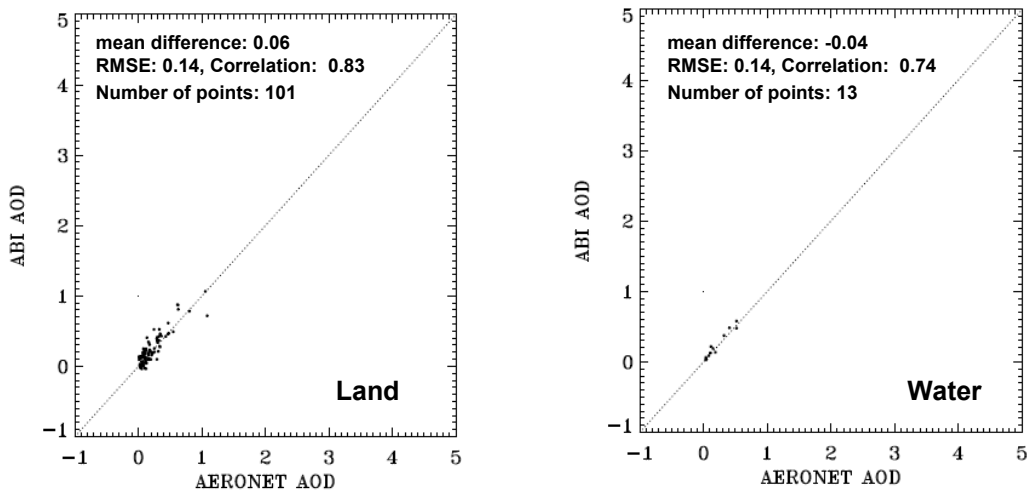


Figure 4-9. Comparison of framework ABI AOD with AERONET AOD at 550 nm over land and over water from 2-day framework run of Aug. 24-25, 2006.

Table 4-6. Accuracy and precision for different AOD ranges from 2-day framework run.

Range	Land				Water			
	AOD	Accuracy	Precision	# of points	AOD	Accuracy	Precision	# of points
Low	<0.04	0.09	0.01	16	<0.4	-0.03	0.02	10
Medium	0.04 - 0.8	0.06	0.03	82				
High	> 0.8	-0.04	0.01	3	>0.4	-0.05	0.02	3

## 4.2.2 Error Budget

The atmosphere and surface input parameters required for the ABI aerosol retrieval algorithm have associated uncertainties. This section explores the effect of these uncertainties on the retrieved aerosol properties. For this, the input parameters are perturbed (changed) by expected ranges of the uncertainties, and the retrieved aerosol properties are compared to the results from retrievals with unperturbed inputs.

TOA reflectances are simulated with the 6S RTM covering a wide range of geometries and aerosol conditions (Table 4-7.). Unless otherwise stated, the climatology water vapor (2.0 cm), ozone (380 Dobson units), fixed wind (6 m/s, westerly) are used in the simulation and retrieval processes. The sensitivity experiments for varying parameters are listed in Table 4-8. For each sensitivity test, the values listed in Table 4-8. are used in the forward simulation and a systematic perturbation is applied to the input (for example,  $\pm 8\%$  for the ozone test). The retrieved aerosol products are then compared with those without perturbation in the input (used as reference). Ozone and water vapor are ABI products and the uncertainty levels used are from their product specifications. Cloud contamination is assumed to increase the TOA reflectance in all ABI channels by 5% or 10%. Surface pressure and ocean surface wind speed/direction are from NCEP data, and the perturbation for surface pressure is assumed as 3% and wind direction as  $10^\circ$  for simplicity. The NCEP wind speed is strongly influenced by observed SSM/I (special sensor microwave imager) data; and the algorithm used to derive wind speed has an RMS error of 1.65 m/s compared with buoys for observations peaking in the 4-7 m/s range [Kalnay et al., 1995; Krasnopolsky et al., 1995]. Taking 6 m/s as the mean value, this RMS difference leads to an uncertainty of  $\sim 25\%$ .

Table 4-7. Geometry and aerosol conditions

Parameters		Dimension	Values
Geometry	cosine of solar zenith angle	10	from 0.4 to 1.0 with a constant interval of 1/15
	cosine of local zenith angle	10	from 0.4 to 1.0 with a constant interval of 1/15
	relative azimuth angle	10	from $0^\circ$ to $180^\circ$ with a constant interval of $20^\circ$
Aerosol optical depth at $0.55\mu\text{m}$		7	0.1, 0.2, 0.4, 0.6, 0.8, 1.0, 1.5
Aerosol models (ocean only)	Fine mode	4	four fine modes same as those in the retrieval algorithm
	coarse mode	5	five coarse modes same as those in the retrieval algorithm
	Fine mode weight	6	0, 0.2, 0.4, 0.6, 0.8, 1.0
Aerosol models (land only)		4	dust, generic, urban, heavy smoke same those in the retrieval algorithm
Land surface reflectance at $2.25\mu\text{m}$ (land only)		10	from 0.02 to 0.2 with a constant interval of 0.02

Table 4-8. Uncertainty levels and values of input atmospheric and surface parameters

Parameters	Uncertainty level	Values
Ozone	+8%	0.095, 0.19, 0.38, 0.76 ( $\times 10^3$ Dobson units)
	-8%	
Water vapor	+9%	0.5, 1.0, 2.0, 4.0, 8.0 (cm)
	-9%	
Surface pressure	+3%	standard surface pressure 1013 (hPa)
	-3%	
Cloud contamination	+5%	Modify TOA reflectance at all ABI channel
	-5%	
Surface wind speed (ocean only)	+25%	1.5, 3, 6, 9, 12 (m/s)
	-25%	
Surface wind direction (ocean only)	10°	30, 60, 90, 120, 150 (°)
	-10°	

The multi-channel aerosol algorithm retrieves aerosol optical depth (AOD), aerosol model and fine-mode weight (FMW) over ocean. A perturbation can change the AOD value, as well as the aerosol model selection and FMW due to the complex multi-channel interdependencies. Figure 4-10. shows the mean value and standard deviation of relative AOD uncertainty (defined as  $\frac{test - reference}{reference}$  for AOD at 550nm) versus AOD over land and over water, respectively. The relative AOD uncertainty is larger at low AOD values and smallest for middle AOD values, except for the ‘dust in SWIR’ case that is discussed later. Among all tests, the aerosol retrieval is the least sensitive to the change in wind direction and therefore not included in Figure 4-10, where the overall relative AOD and FMW uncertainty are within 0.03%, and the model misidentification rate is ~0.8%. In the ocean algorithm, wind direction is fixed as westerly in the LUT, and the test of  $\pm 10^\circ$  change only modifies the sunglint directional reflectance.

In Figure 4-10., the uncertainty is generally smaller over ocean than over land mainly because the ocean aerosol retrieval uses more ABI channels, and some channels with less sensitivity to the specified change will weaken the overall effect. The results for the cloud contamination test and wind speed is not displayed in Figure 4-10 due to their relatively large influence as listed in Table 4-9. The aerosol algorithm is less sensitive to uncertainty in ozone and water vapor, suggesting the use of climatology data may be reasonable when the ABI products are missing. However, it is more sensitive to surface pressure, ocean wind speed, and especially cloud contamination, suggesting a need for high quality for those inputs. Over water, the uncertainty due to cloud contamination is expected to be smaller because the specified absolute perturbation is larger for the same percentage level change over land. The percentage of aerosol model misidentification over land is illustrated in Figure 4-11.. Based on the results shown in this figure the algorithm can meet specification (11%) for differentiating dust from non-dust aerosols.

The FMW uncertainties (defined as *test – control*) over water are generally within 0.05 except for cloud contamination at the 10% level, as shown in Figure 4-12..

Table 4-9. Mean values and standard deviations of relative AOD errors due to cloud contamination and error in wind speed. (AOD550: aerosol optical depth at 550 nm; wspd: wind speed)

AOD550	LAND		WATER			
	cloud +5%	cloud +10%	cloud +5%	cloud +10%	wspd +25%	wspd -25%
<b>Bias</b>						
0.1	0.4939	1.0128	0.1168	0.2357	-0.1580	0.0963
0.2	0.3010	0.5952	0.0643	0.1472	-0.0813	0.0478
0.4	0.2155	0.4527	0.0531	0.1098	-0.0401	0.0213
0.6	0.1826	0.4097	0.0581	0.1109	-0.0241	0.0124
0.8	0.1743	0.4181	0.0631	0.1207	-0.0163	0.0081
1.0	0.1794	0.4414	0.0649	0.1279	-0.0118	0.0054
1.5	0.1714	0.4217	0.0715	0.1472	-0.0059	0.0025
<b>Standard deviation</b>						
0.1	0.2372	0.4976	0.1646	0.2401	0.2512	0.1818
0.2	0.2173	0.5043	0.1215	0.1812	0.144	0.0945
0.4	0.2232	0.4463	0.0869	0.1352	0.0816	0.0485
0.6	0.1398	0.3904	0.0777	0.1474	0.0544	0.0324
0.8	0.2050	0.4378	0.0744	0.1468	0.0411	0.0253
1.0	0.2763	0.4700	0.0822	0.1524	0.0323	0.0194
1.5	0.3167	0.3816	0.0859	0.1507	0.0194	0.0111

Underestimating (or neglecting) aerosol scattering in the SWIR channel may introduce large errors for dust particles. To quantify this error, scattering by dust aerosol in all ABI channels (including the SWIR channel) is accounted for in the forward simulation that provides the input TOA reflectances, but not in the retrieval process. The results are then compared with the case of no dust in the forward simulation or in the retrieval process. Underestimating dust in the SWIR channel increases the surface reflectance in this channel and hence those in the red and blue channels, which results in the underestimation of AOD by 10-15% for different AOD values (denoted as ‘dust in swir’ test in Figure 4-12.) and the dust misidentification rate is about 11%.

Doubling/halving of chlorophyll concentration, used in the ocean reflectance model, slightly changes (~0.0003) the water-leaving radiance at 0.64µm. However, the effect is so small that it does not change the selection of model combination and FMW from the minimum residual calculation, and hence do not modify the AOD retrieval from the reference channel.

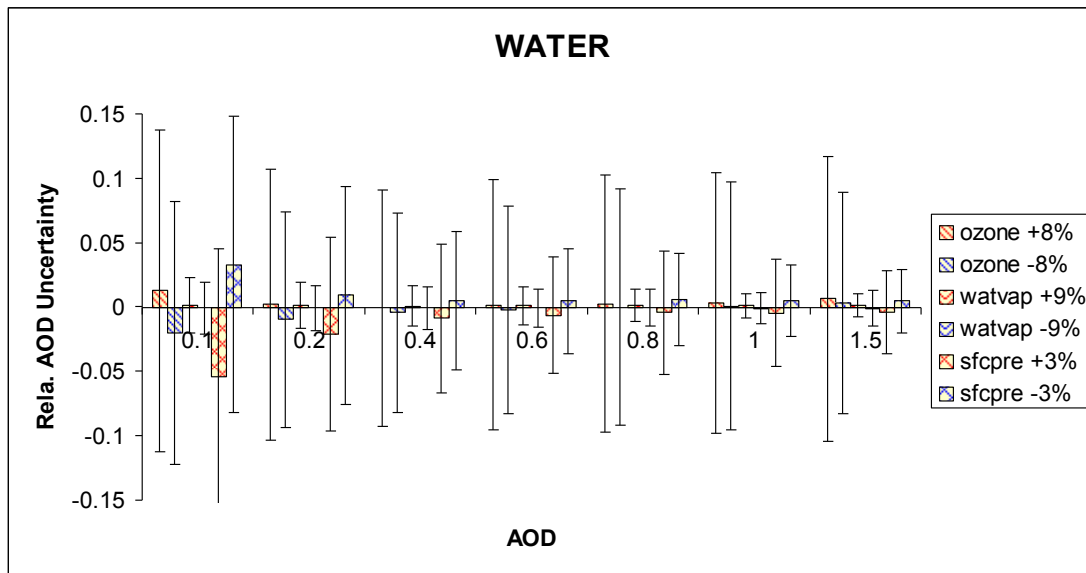
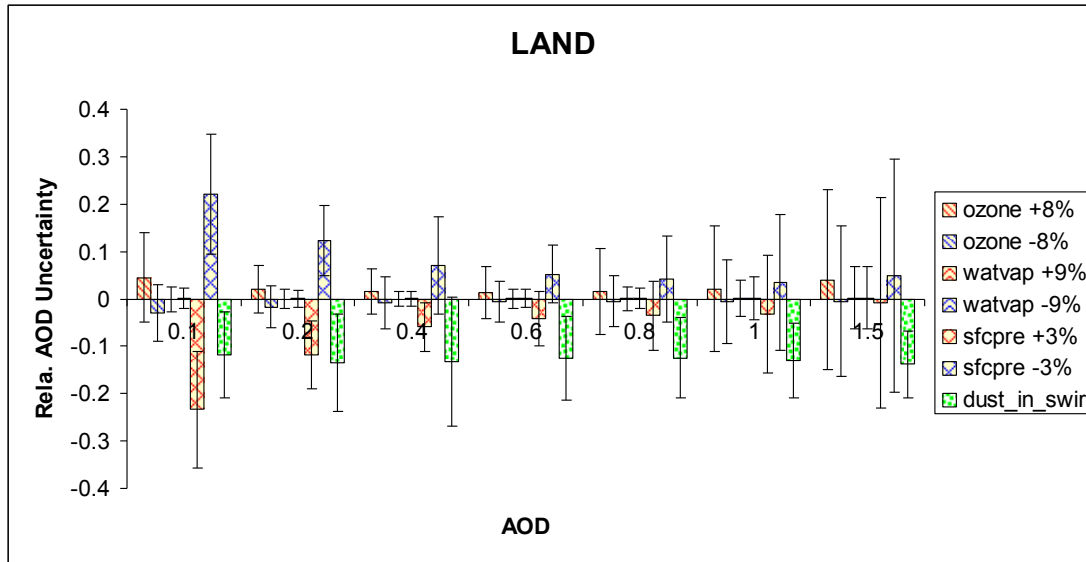


Figure 4-10. Mean values and standard deviations of relative AOD uncertainty for uncertainties in ozone, water vapor (watvap) and surface pressure (sfcpre) over land and water, and dust presence test in SWIR channel (dust in swir) over land.

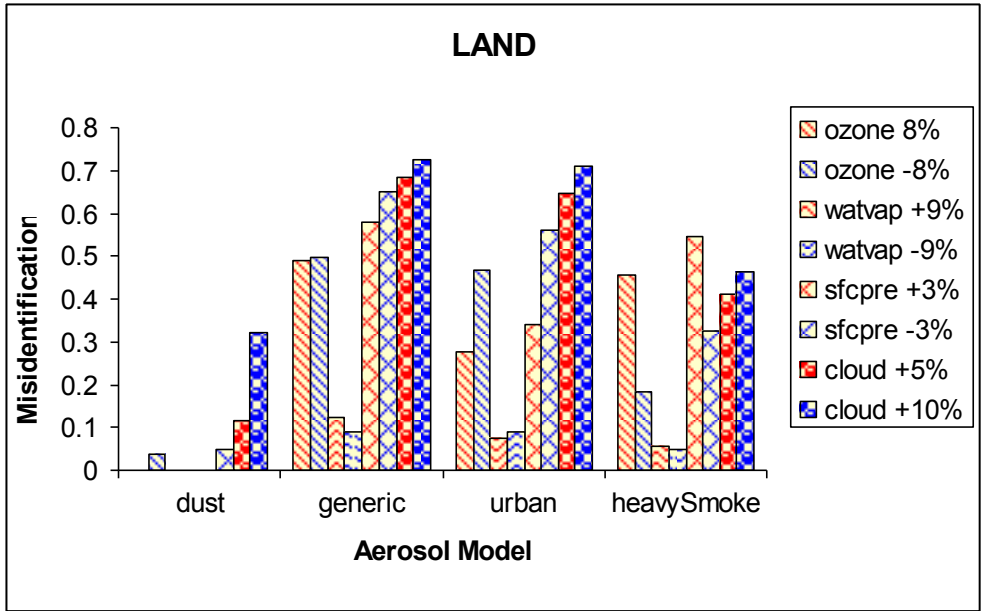


Figure 4-11. Land aerosol model misidentification for ozone, water vapor (watvap), surface pressure (sfcpre) and cloud contamination (cloud) tests.

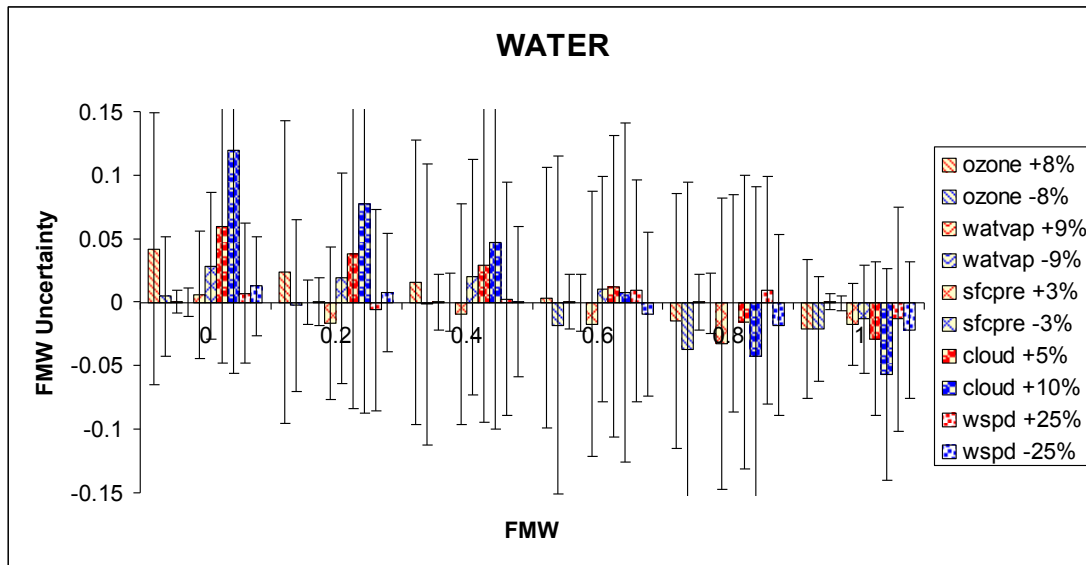


Figure 4-12. Mean values and standard deviations of fine-mode weight (FMW) uncertainty over water for ozone, water vapor (watvap), surface pressure (sfcpre), cloud contamination (cloud), and surface wind speed (wspd) tests.

## **5 PRACTICAL CONSIDERATIONS**

### **5.1 Numerical Computation Considerations**

The LUT approach uses pre-calculated values of spectral atmospheric transmittances, reflectances, spherical albedo and surface BRDF as functions of AOD at 550 nm, aerosol models, geometries and ocean surface wind speeds. In the LUT, following the VIIRS approach [Vermote et al., 2006], the TOA is given as a function of scattering angle with an interval of 4 degrees. The range of scattering angles is calculated from the solar and local zenith angles and the relative azimuth angle. This method provides a relatively rapid search of the LUT. Just like in the standard MODIS algorithm [Remer et al., 2005], the interval halving method is used in LUT for searching for the “best” combination of fine and coarse mode of ocean aerosol models; this increases efficiency as well.

### **5.2 Programming and Procedural Considerations**

The aerosol retrieval is carried out pixel by pixel. It requires calibrated and geo-located ABI reflectances, ABI cloud mask and snow/ice mask as ABI dynamic input. Mapping processes for static ancillary (e.g. surface elevation) can be processed offline. The programming design uses modules, providing the flexibility for ease upgrades.

The data that need to be configurable for possible post-launch adjustment include algorithm coefficients (LUT and land surface reflectance relationship), criterion values (e.g. selecting atmospheric conditions), water vapor and ozone dataset depending on the ABI data availability, and metadata setting.

### **5.3 Quality Assessment and Diagnostics**

The following flags will be produced:

- Missing/No data
- Coast, Snow/Ice, Cloud proximity
- Cloud (retrieval from “possibly clear” reflectance category)
- Pixel with large local zenith angle (> 60 degrees)
- Less than maximum number of channels used for retrieval
- Large solar zenith angles
- Negative retrievals
- Retrievals over bright surfaces
- Flags based on spatial variability tests for residual cloud contamination

### **5.4 Exception Handling**

The quality control flags for aerosol retrieval will be checked and inherited from the flagged Level 1b sensor input data, including bad sensor input data, missing sensor input data and validity of each aerosol channel; and will be checked and inherited from the ABI cloud mask at each pixel for clear, possibly clear, cloud and possibly cloudy.

The algorithm does checks for conditions not favorable for aerosol retrieval and generates quality control flags for snow/ice pixel, bright surface, nearby cloud and costal pixel, and viewing geometry.

## **5.5 Algorithm Validation**

During the pre-launch phase of development, and testing, the primary means of aerosol product validation is the comparison with measurements made from the ground such as AERONET. Because of the limited number of ground locations where high quality ground observations of aerosol properties are made this type of validation is necessarily restricted in space. Evaluation is also done by performing retrievals from model-simulated proxy ABI data, and by comparing the retrieved aerosol product to the known aerosol data used in the simulation. This type of validation is ideal for evaluating algorithm performance not only for the aerosol products but also for all other (input, internal, and ancillary) parameters that influence aerosol retrievals. Because all relevant data are known in the simulations uncovering algorithm (programming) problems is also relatively easy. However, due to the excessive computational burden realization of a wide range of realistic scenarios may not be practical, and thus the validation may be limited in scope. Comparison with (independent) satellite-based aerosol products tests the consistency of ABI retrievals under realistic conditions. To be useful this type of evaluation should be performed for long (preferably continuous) time periods. For this purpose, routine comparisons are carried out by running the ABI retrieval algorithm with near-real time MODIS L1-B radiance data, and then comparing to MODIS products, which are considered to be independent.

Once the actual (final) spectral response functions of the ABI sensors are known the atmosphere and ocean surface LUTs must be re-generated, and the relationship between VIS and SWIR surface reflectances must be re-derived. The validation methodologies listed above will be applied to actual aerosol products.

Validation of the current (Version 5) algorithm is presented in Section 4.2. The detailed aerosol products validation is described in the GOES-R aerosol product validation plan documents.

## **6 ASSUMPTIONS AND LIMITATIONS**

This section describes the limitations and assumptions in the current version of the aerosol retrieval algorithm, and potential future enhancements to the algorithm.

## 6.1 Performance

The following assumptions have been made in the current algorithm developing:

- Aerosol shape is spherical. Accounting for the non-spherical shape of dust aerosol is studied in a separate and independent research; the results of that research may be included in the retrieval in the future.
- Aerosol is vertically well-mixed, and the impact of aerosol height may not be a priority because the ABI channels for aerosol retrieval are well selected to minimize gas absorption.
- Surface reflectance of ocean can be calculated and that of land can be estimated with sufficient accuracy;
- Land surface is dark and Lambertian. In an AWG sponsored project, an alternative algorithm is currently being developed that may extend the retrievals for bright surfaces. This algorithm does not assume Lambertian surface reflectance. Instead, bidirectional surface reflectance and aerosol optical depth are simultaneously retrieved.
- Calibrated and geo-located radiances in ABI channels 1-6 are available.
- ABI cloud mask is available.
- Ancillary data are available.

The limitations in the current retrieval algorithm are:

- Retrieval limited to dark surface;
- Retrieval limited to clear-sky conditions;
- Retrieval limited to daytime only;
- Retrievals may not be valid at certain viewing geometry.

The 2.25- $\mu\text{m}$  channel is critical for the over-land algorithm. Without this channel surface reflectance cannot be estimated and aerosol retrieval is not performed. Loss of either of the 0.47- $\mu\text{m}$  or the 0.64- $\mu\text{m}$  channel would degrade the performance, since aerosol type cannot be retrieved in this case. Loss of any of the channels used in the over-ocean retrieval would likely lead to decrease of quality. No mitigation against channel loss is implemented in the current (Version 5) algorithm.

## 6.2 Assumed Sensor Performance

The calibrated and geo-located ABI channel radiances are assumed to be available for the current aerosol retrieval algorithm. Over land, loss of 2.25  $\mu\text{m}$  channel will disable the algorithm as it is needed to estimate surface reflectance. Similarly, aerosol type cannot be estimated in case the 0.47- or 0.64- $\mu\text{m}$  channel is missing. Over ocean, loss of one or two channels of 0.64, 0.86, 1.61 and 2.25  $\mu\text{m}$  increases the bias to be about twice of the base case with four channels.

## 6.3 Pre-Planned Product Improvements

### 6.3.1 Retrieval over bright land surface

An alternate land algorithm, the Multiangle Implementation of Atmospheric Correction algorithm (MAIAC), developed by the team at the University of Maryland Baltimore County, may replace the current over-land algorithm. MAIAC is designed to work over most surface types including bright surfaces (except snow). MAIAC uses the time sequence of images, and thus takes advantage of geostationary geometry of fixed local zenith angle and changing solar zenith angle in a way that allows the simultaneous retrieval of AOD and surface bidirectional reflectance.

### 6.3.2 Additional internal tests

The current algorithm only includes test for sunglint. However, experience with the MODIS algorithm showed that aerosol retrievals are very sensitive to contaminations by clouds, snow/ice, fire, turbid water, etc. [Remer et al., 2006]. Test for the presence of snow/ice and turbid were tested within the ABI algorithm. These tests were designed based on similar tests applied in the MODIS and VIIRS algorithms. Their implementation in the ABI algorithm is, however, not straightforward, since not all channels used in the MODIS/VIIRS algorithms are available from ABI. Therefore, the tests require further development and evaluation. Details of the tests currently being developed are provided in Appendix C1 and C3.

Note that implementation of internal tests to eliminate cloud, snow/ice contamination, identification of turbid water, etc. may require using the 1-km Level 1b reflectances. In this case, the algorithm need to be updated such that averaging of qualified reflectances for the 2-km grid is done inside the aerosol retrieval algorithm.

## REFERENCES

- Ackerman, A.S., O.B. Toon, D.E. Stevens, A.J. Heymsfield, V. Ramanathan, and E.J. Welton, Reduction of tropical cloudiness by soot, *Science*, 288, 1042-1047, 2000.
- Albrecht, B.A., Aerosols, cloud microphysics, and fractional cloudiness, *Science*, 245, 1227-1230, 1989.
- Bohren, C.F., and D.R. Huffman, *Absorption and Scattering of Light by Small Particles*, John Wiley, Hoboken, N.J., 1983.

- Chameides, W.L., et al., A case study of the effects of atmospheric aerosols and regional haze on agriculture: An opportunity to enhance crop yields in China through emission controls? *Proc. Natl. Acad. Sci.*, 96, 13,626-13,633, 1999.
- Chandrasekhar, S., 1960: *Radiative Transfer*, New York, Dover, 393 p.
- Charlson, R.J., S.E. Schwartz, J.M. Hales, R.D. Cess, J.A. Coakley, J.E. Hansen, and D.J. Hofmann, Climate forcing by anthropogenic aerosols, *Science*, 255, 423-430, 1992.
- Coakley, J.A., R.D. Cess, and F.B. Yurevich, The effect of tropospheric aerosols on the Earth's radiation budget: a parameterization for climate models, *J. Atmos. Sci.*, 40, 116-138, 1983.
- Cox, C., and W. Munk (1954). Statistics of the sea surface derived from sun glitter. *J. Mar. Res.*, 13, 198-208.
- Dubovik, O., et al., Variability of absorption and optical properties of key aerosol types observed in worldwide locations, *J. Atmos. Sci.*, 59, 590-608, 2002.
- Dubovik, O., et al., Application of spheroid models to account for aerosol particle nonsphericity in remote sensing of desert dust, *J. Geophys. Res.*, 111, D11208, doi:10.1029/2005JD006619, 2006.
- Govaerts, Y. M., S. Wagner, A. Lattanzio, and P. Watts, Joint retrieval of surface reflectance and aerosol optical depth from MSG/SEVIRI observations with an optimal estimation approach: 1. Theory, *J. Geophys. Res.*, 115, D02203, doi:10.1029/2009JD011779, 2010.
- Hansen, J., M. Sato, and R. Ruedy, Radiative forcing and climate response, *J. Geophys. Res.*, 102, 6831-6864, 1997.
- Holben B.N., et al., AERONET - A federated instrument network and data archive for aerosol characterization, *Rem. Sens. Environ.*, 66, 1-16, 1998.
- Holben, B.N., et al., An emerging ground-based aerosol climatology: Aerosol Optical Depth from AERONET, *J. Geophys. Res.*, 106, 12,067-12,097, 2001
- Holben, B.N., et al., An emerging ground-based aerosol climatology: Aerosol Optical Depth from AERONET, *J. Geophys. Res.*, 106, 12,067-12,097, 2001
- Ichoku, C., et al., A spatio-temporal approach for global validation and analysis of MODIS aerosol products, *Geophys. Res. Lett.*, 29(12): art. no.-1616, 2002.
- Kalnay, E., et al., The NCEP/NCAR 40-Year Reanalysis Project, *Bull. Amer. Meteor. Soc.*, 77, 437-471, 1996.
- Kaufman, Y. J., and D. Tanré, Algorithm for Remote Sensing of Tropospheric Aerosol from MODIS, <http://eosps0.gsfc.nasa.gov/atbd/modistables.html>, 1996

- Kaufman, Y. J., N. Gobron, et al., Relationship between surface reflectance in the visible and mid-IR used in MODIS aerosol algorithm – theory, *Geophys. Res. Lett.* 29(23): art. no.-2116, 2002.
- Kaufman, Y. J., and L. Remer, “Detection of forests using mid-IR reflectance: An application for aerosol studies,” *IEEE Trans. Geosci. Remote Sensing*, vol. 32, pp. 672–683, 1994.
- Kaufman, Y. J., D. Tanré, et al., Operational remote sensing of tropospheric aerosol over land from EOS moderate resolution imaging spectroradiometer, *J. Geophys. Res.*, 102(D14): 17051-17067, 1997
- Kaufman, Y. J., A. E. Wald, et al., The MODIS 2.1- $\mu$ m channel – Correlation with visible reflectance for use in remote sensing of aerosol, *IEEE Transactions On Geoscience and Remote Sensing* 35(5): 1286-1298, 1997
- King, M.D., D.M. Byrne, B.M. Herman and J.A. Reagan, Aerosol size distribution obtained by inversion of optical depth measurements, *J. Atmos. Sci.*, 35, 2153- 2167, 1978.
- Knapp, K. R., R. Frouin, S. Kondragunta, and A. Prados, Toward aerosol optical depth retrievals over land from goes visible radiances: Determining surface reflectance, *Int. J. Remote Sens.*, 26(18), 4097 –4116, 2005.
- Koepke, P., Effective reflectance of oceanic whitecaps, *Appl. Opt.*, 23, 1816-1823, 1984
- Koren, I.Y., Y.J. Kaufman, L.A. Remer, and J.V. Martins, Measurement of the effect of Amazon smoke on inhibition of cloud formation, *Science*, 303, 1342, 2004.
- Krasnopolsky, V.M., L.C. Breaker, and W.H. Gemmill, A neural network as a nonlinear transfer function model for retrieving surface wind speeds from the SSM/I, *J. Geophys. Res.*, 100, 11,033-11,045, 1995.
- Kotchenova S.Y. and E. F. Vermote, A vector version of the 6S radiative transfer code for atmospheric correction of satellite data: an Overview, presented at 29th Review of Atmospheric Transmission Models Meeting, Lexington, Mass., USA, 13–14 June 2007.
- Kotchenova S.Y., E.F. Vermote, R. Matarrese, and F.J. Klemm, Jr., Validation of a vector version of the 6S radiative transfer code for atmospheric correction of satellite data. Part I: Path radiance, *Appl. Opt.*, 45, 6762-6774, 2006.
- Kotchenova S.Y. and E.F. Vermote, Validation of a vector version of the 6S radiative transfer code for atmospheric correction of satellite data. Part II. Homogeneous Lambertian and anisotropic surfaces, *Appl. Opt.*, 46, 4455-4464, 2007.

- Laszlo I., P. Ciren, H. Liu, S. Kondragunta, J. D. Tarpley and M. D. Goldberg, 2008: Remote sensing of aerosol and radiation from geostationary satellites, *Adv. Space Res.*, **41**, 11, 1882-1893, doi: 10.1016/j.asr.2007.06.047
- Levy, R.C., L.A. Remer, and O. Dubovik, Global aerosol optical properties and application to Moderate Resolution Imaging Spectroradiometer aerosol retrieval over land, *J. Geophys. Res.*, 112(D13210), doi: 10.1029/2007JD009007, 2007
- Pinty, B., F. Roveda, M. M. Verstraete, N. Gobron, Y. Govaerts, J. V. Martonchik, D. J. Diner, and R. A. Kahn, Surface albedo retrieval from Meteosat: 1. Theory, *J. Geophys. Res.*, 105, 18,099– 18,112, 2000.
- Pope, C Arden; et al., Cancer, cardiopulmonary mortality, and long-term exposure to fine particulate air pollution, *J. Amer. Med. Assoc.* 287: 1132–1141, doi:10.1001/jama.287.9.1132, 2002.
- Ramanathan, V., P.J. Crutzen, J.T. Kiehl, and D. Rosenfeld, Aerosols, climate, and the hydrological cycle, *Science*, 294, 2119-2124, 2001
- Remer, L. A., Y. J. Kaufman, et al., The MODIS aerosol algorithm, products, and validation, *J. Atmos. Sci.*, 62(4), 947-973, 2005
- Remer, L. A., D. Tanre, Y.J. Kaufman, R. Levy and S. Mattoo, Algorithm for Remote Sensing of Tropospheric aerosol from MODIS: Collection 5, Product ID MOD04/MYD04, 2006.
- Rosenfeld, D., and I.M. Lensky, Satellite-based insights into precipitation formation processes in continental and maritime convective clouds, *Bull. Am. Met. Soc.*, 79, 2457-2476, 1998.
- Schmit, T.J., M.M. Gunshor, W.P. Menzel, J.J. Gurka, J. Li, and A.S. Bachmeier, Introducing the next generation advanced baseline imager on GOES-R, *Bull. Am. Met. Soc.*, 86 (8), 1079-1096, 2005.
- Shettle, E. P., and R. W. Fenn, Models for the aerosol of the lower atmosphere and the effect of humidity variations on their optical properties, *AFGL Tech. Rep. AFGL-TR 790214*, Opt. Phys. Div., Air Force Geophys. Lab., Hanscom Air Force Base, Mass., 1979.
- Tanré, D., Y. J. Kaufman, et al., Remote sensing of aerosol properties over oceans using the MODIS/EOS spectral radiances, *J. Geophys. Res.*, 102(D14), 16971-16988, 1997.
- Thomas, G., C. Poulsen, R. Curier, G. De Lewuw, S. Marsh, E. Carboni, R. Grainger, and R. Siddans, Comparison of AATSR and SEVIRI aerosol retrievals over the Northern Adriatic, *Q. J. R. Meteorol. Soc.*, 133(S1), 85– 95, 2007.

- Twomey, S., The influence of pollution on the shortwave albedo of clouds, *J. Atmos. Sci.*, 34, 1149-1152, 1977.
- Vermote, E. and D. Tanré, Analytical expressions for radiative properties of planar rayleigh scattering media, including polarization contributions. *J. Quant. Spectrosc. Radiat. Transfer*, Vol. 47, No. 4, 305-314, 1992.
- Vermote, E. F., D. Tanre, J. L. Deuze, M. Herman, and J. J. Morcrette (1997), Second Simulation of the Satellite Signal in the Solar Spectrum, 6S: An overview, *IEEE Trans. Geosci. Remote Sens.*, 35(3), 675-686, 1997.
- Vermote, E. F., R. Slonaker, S. Vibert, B. Petrenko, National Polar-orbiting Operational Environmental Satellite System (NPOESS) VIIRS Aerosol Optical Thickness and Particle Size Parameter Algorithm Theoretical Basis Document, Version 5, Revision 8: June 2006, Document #: Y2388
- Wang, M., and H.R. Gordon, Radiance reflected from the ocean-atmosphere system: synthesis from individual components of the aerosols size distribution, *Appl. Opt.*, 33, 7088-7095, 1994.
- Yu, H., S.C. Liu, and R.E. Dickinson, Radiative effects of aerosols on the evolution of the atmospheric boundary layer, *J. Geophys. Res.*, 107, 4142, 2002.
- Yu, H., R.E. Dickinson, M. Chin, Y.J. Kaufman, B.N. Holben, I.V. Geogdzhayev, and M.I. Mishchenko, Annual cycle of global distributions of aerosol optical depth from integration of MODIS retrievals and GOCART model simulations, *J. Geophys. Res.*, 108, 4128, 2003.

## APPENDIX

### A. Effect of Instrument noise on AOD Retrieval

The effect of this instrument noise on the retrieved aerosol optical depth is estimated from the Signal-to-Noise Ratio (SNR) following Tanre et al. (1997). In that method a SNR is defined in terms of aerosol optical depth as  $\tau / \Delta\tau$ , where  $\tau$  is the “typical” value of the aerosol optical depth, and the ‘Noise Equivalent Differential Optical Depth’  $\Delta\tau$  is estimated using the single-scattering approximation:

$$\Delta\tau = \Delta\rho \frac{4\cos(\theta_v)\cos(\theta_s)}{\omega_0 P(\Theta)}, \quad (\text{A-1})$$

where  $\theta_v$  and  $\theta_s$  are solar and local zenith angles,  $\omega_0$  is the aerosol single scattering albedo,  $P(\Theta)$  is the aerosol phase function, and  $\Delta\rho$  is the ‘Noise Equivalent Differential Spectral Reflectance’ calculated from the SNR for reflectances. Note that different aerosol models have different optical properties ( $\omega_0$ ,  $P$ ) leading to different, aerosol-model dependent sensitivities.

These reflectances are listed in Table A-1 for the required resolution of 2 km for the aerosol retrieval channels. It is noted that the noise for the 0.64- $\mu\text{m}$  channel at 500 m resolution is 1/1000, instead of 1/300, because a SNR of 50:1 must be achieved for targets of 5% reflectance, as specified in PORD. (For a detector with SNR=300 for target of 100% reflectance, the noise is 0.33% (in reflectance units). If the noise is also 0.33% for a target of 5% reflectance, the SNR will be  $5\% / 0.33\% = 15$ . Therefore the noise is assumed to be 0.1%, which means SNR=50 at 5% and SNR=1000 at 100%.)

The largest noise in aerosol optical depth  $\Delta\tau$  is expected for the Sun at zenith ( $\theta_s = 0$ ) and for nadir observation  $\theta_v = 0$ , and for the lowest value of phase function at a scattering angle of  $120^\circ$  (Tanre et al., 1997; Shettle and Fenn, 1979). The single-scattering albedo and phase function are calculated using nine ocean aerosol models used in the ABI aerosol retrieval (four fine modes and five coarse modes, see Section 3.4.1.2). The resulting  $\Delta\tau$  is listed in Table A-2. Typical values of the spectral aerosol optical thickness  $\tau$  are taken from Hoppel et al., (1990) and also shown in Table A-1. From these values the SNR at 2 km resolution is then calculated. The results for ocean appear in Table A-3.

Table A-1.  $\Delta\rho$  and  $\tau$  for the ABI “aerosol” channels.

Channel	0.47 $\mu\text{m}$	0.64 $\mu\text{m}$	0.86 $\mu\text{m}$	1.61 $\mu\text{m}$	2.25 $\mu\text{m}$
Noise in Reflectance at 2km	1/600	1/4000	1/600	1/600	1/300
Typical $\tau$	0.2	0.1	0.05	0.03	0.01

Table A-2. Aerosol optical depth sensitivity  $\Delta\tau$  for ABI ocean aerosol models.

Channel	0.47 $\mu\text{m}$	0.64 $\mu\text{m}$	0.86 $\mu\text{m}$	1.61 $\mu\text{m}$	2.25 $\mu\text{m}$
F1	0.033	0.003	0.015	0.014	0.033
F2	0.050	0.006	0.031	0.019	0.030
F3	0.064	0.008	0.042	0.023	0.034
F4	0.070	0.009	0.051	0.029	0.041
C1	0.083	0.012	0.082	0.085	0.153
C2	0.096	0.013	0.080	0.085	0.170
C3	0.118	0.014	0.083	0.082	0.170
C4	0.097	0.010	0.055	0.058	0.112
C5	0.118	0.012	0.068	0.063	0.116

Table A-3. Signal-to-noise ratio for optical depth for ocean aerosol models at 2-km resolution.

Channel	0.47 $\mu\text{m}$	0.64 $\mu\text{m}$	0.86 $\mu\text{m}$	1.61 $\mu\text{m}$	2.25 $\mu\text{m}$
F1	6.01	32.07	3.32	2.08	0.30
F2	4.02	16.49	1.62	1.56	0.33
F3	3.11	12.23	1.18	1.30	0.30
F4	2.87	10.65	0.98	1.04	0.25
C1	2.40	8.36	0.61	0.35	0.07
C2	2.09	8.00	0.63	0.35	0.06
C3	1.69	7.16	0.60	0.36	0.06
C4	2.05	10.20	0.91	0.52	0.09
C5	1.69	8.40	0.74	0.47	0.09

The optical properties of land aerosol models are assumed to be functions of the optical depth in the ABI aerosol algorithm. However, to simplify estimating the effect of noise in the over-land retrieval the single typical  $\tau$  values in Table A-1 are used again. The signal-to-noise ratios in terms of aerosol optical depth for the land aerosol models are shown in Table A-4.

Table A-4. Signal-to-noise ratio of optical depth for land aerosol models at 2-km resolution.

Channel	0.47 $\mu\text{m}$	0.64 $\mu\text{m}$	0.86 $\mu\text{m}$	1.61 $\mu\text{m}$	2.25 $\mu\text{m}$
Smoke	4.23	19.21	1.83	0.65	0.09
Dust	4.84	18.66	1.58	0.86	0.13
Generic	3.59	16.96	1.68	0.63	0.09
Urban	3.21	15.11	1.65	0.66	0.09

The SNRs for optical depth in Table A-3 and Table A-4 indicate that the noise at the 2-km resolution may be too large for accurate aerosol retrieval from ABI channels with wavelengths of 0.86  $\mu\text{m}$  and higher. In terms of this SNR, retrievals might be better performed from the 0.64- $\mu\text{m}$  channel where the optical-depth SNRs are 7 or larger. Decreasing the resolution from 2 km to 4 km decreases the noise by a factor of 2, and hence increases the SNR by a factor of 2, and so on. The SNR at different resolutions are shown for the least sensitive (2.25- $\mu\text{m}$ ) channel for ocean and land aerosol models in Table A-5 and Table A-6, respectively. These results show that the SNR is close to or larger than unity for the 2.25- $\mu\text{m}$  channel for all aerosol models when the spatial resolution increases to 32 km. It should be emphasized again that aerosol retrieval in the ABI algorithm is effectively done from the shorter wavelength channels (reference channels of 0.47  $\mu\text{m}$  for land, and 0.86  $\mu\text{m}$  for ocean) where the SNRs are higher.

Table A-5. Aerosol optical depth signal-to-noise ratio for ocean aerosol models at 2.25  $\mu\text{m}$  for different spatial resolutions.

Resolution	2 km	4 km	8 km	16 km	32 km
F1	0.30	0.60	1.20	2.39	4.78
F2	0.33	0.66	1.32	2.65	5.30
F3	0.30	0.59	1.19	2.37	4.75
F4	0.25	0.49	0.98	1.97	3.94
C1	0.07	0.13	0.26	0.52	1.05
C2	0.06	0.12	0.24	0.47	0.94
C3	0.06	0.12	0.23	0.47	0.94
C4	0.09	0.18	0.36	0.71	1.43
C5	0.09	0.17	0.35	0.69	1.38

Table A-6. Aerosol optical depth signal-to-noise ratio for land aerosol models at 2.25  $\mu\text{m}$  for different spatial resolutions.

Resolution	2 km	4 km	8 km	16 km	32 km
Smoke	0.09	0.17	0.34	0.78	1.38
Dust	0.13	0.26	0.53	1.19	2.12
Generic	0.09	0.17	0.35	0.78	1.38
Urban	0.09	0.19	0.37	0.84	1.49

The above analysis assumes the noise is constant and always present at the same level. A more appropriate interpretation of the SNR values in Table 2-5 is to treat the noise as a random process with a mean of zero and standard deviation of the SNR. In this model the reflectance error is  $\Delta\rho = \mu_0^{-1} N(0, \sigma)$ , where  $\mu_0$  is the cosine of the solar zenith angle, and

$N$  is the random noise with standard deviation  $\sigma$  whose values are the SNRs listed in Table 2.5. The effect of the noise on the optical depth retrieval was estimated using this noise model by performing the ABI aerosol retrieval once from noise free reflectances ( $\sigma = 0$ ) and once with noisy reflectances ( $\sigma = SNR$ ). The reflectances used for this exercise were the MODIS collection 5 10-km aerosol reflectances for 03/2000-12/2007 for Terra and 07/2002 -12/2007 for Aqua. (The MODIS reflectances were assumed to be noise free in this exercise.) Taking the difference of the two retrievals provided a measure of the impact of noise. The retrievals from both reflectances were then compared to collocated AERONET version 2 level 2.0 aerosol data; accuracies and precisions were calculated, which in turn were compared to the requirements. The results indicated only small biases ( $3 \times 10^{-5}$ - $5 \times 10^{-3}$ ) and standard deviations of the biases (0.049) as a result of the assumed noise.

The effect of noise was also evaluated by perturbing the radiance by a constant noise at the level specified in Table A-1. In this exercise the perturbed reflectance  $\rho'_\lambda$  is expressed as

$$\mu_0 \rho'_\lambda = \mu_0 \rho_\lambda + Noise \tag{A-2}$$

Here  $\mu_0$  is cosine of solar zenith angle;  $\rho_\lambda$  is the un-perturbed TOA reflectance. The TOA ABI reflectances in the aerosol channels were calculated from forward simulation for sample locations selected within the GOES East and West domains with local zenith angles less than  $60^\circ$ . For the east domain 31 locations were specified over ocean and 10 over land. For the west domain 39 locations were used over ocean and 3 over land. The locations are shown in Figure A-1.

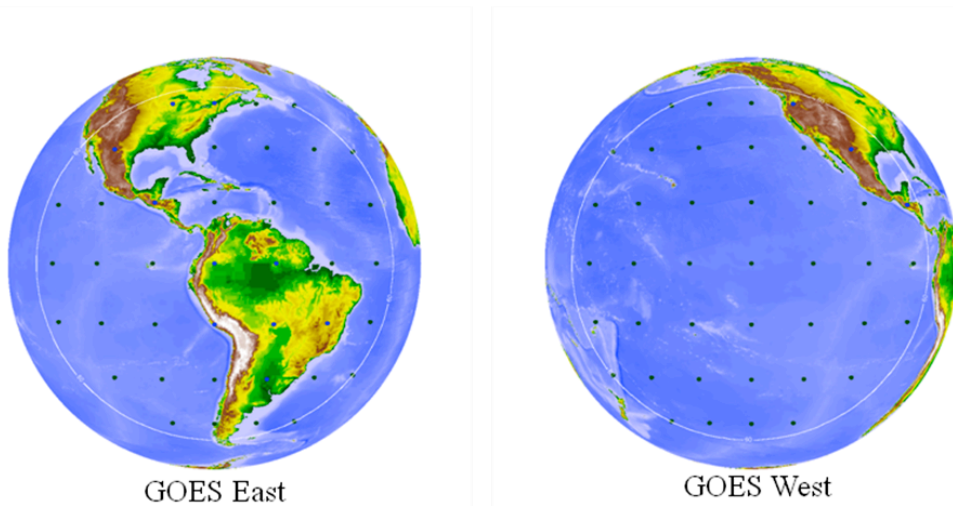


Figure A-1. Locations selected for aerosol retrievals in the GOES east and west domains.

Solar and local zenith and azimuth angles were calculated for every hour of four days (Mar 20, Jun 21, Sep 22, and Dec 21 (solstices and equinoxes)). Solar zenith angles were restricted to be less than  $80^\circ$ . Constant values of total precipitable water (2.0 cm), column

ozone amount (0.38 atm-cm), surface elevation (sea level), surface pressure (1013 mb), wind speed (6 m/s), and wind direction (due east) were assumed. Aerosol models and optical depths and surface albedo over land were as follows:

- Over water
  - 4 fine mode aerosol types
  - 5 coarse mode aerosol types
  - 6 fine mode weight: 0.0, 0.2, 0.4, 0.6, 0.8, 1.0
  - 9 aerosol optical depth at 0.55 $\mu$ m: 0.05, 0.1, 0.2, 0.3, 0.4, 0.6, 0.8, 1.0
- Over land
  - 4 aerosol models: dust, generic, urban, smoke
  - 9 aerosol optical depth at 0.55 $\mu$ m: 0.05, 0.1, 0.2, 0.3, 0.4, 0.6, 0.8, 1.0
  - 10 surface albedo at 2.26  $\mu$ m: 0.02, 0.04, 0.06, 0.08, 0.10, 0.12, 0.14, 0.16, 0.18, 0.20

Retrievals were performed from 1) reflectances without noise; 2) reflectances with positive noise added; and 3) reflectances with negative noise added. The AOD retrieved from the perturbed (noise added) reflectances were then compared to those retrieved from the un-perturbed ones, and the aerosol optical depth at 0.55 $\mu$ m and Ångström Exponent were analyzed to evaluate the impact of noise. The results are shown in Table A-7, Table A-8, Table A-9, and Table A-10.

Table A-7. Bias and standard deviation (Std.dev) of AOD retrieved over water from noisy reflectances relative to that from noise-free reflectance.

Input AOD	Positive Noise Added			Negative Noise Added		
	Bias	Std. dev	Number	Bias	Std. dev	Number
<b>0.05</b>	0.007	0.016	276120	0.010	0.025	51878
<b>0.1</b>	-0.002	0.024	276120	0.013	0.031	132643
<b>0.15</b>	-0.009	0.030	276120	0.017	0.036	180733
<b>0.2</b>	-0.015	0.037	276120	0.020	0.041	206434
<b>0.3</b>	-0.025	0.052	276120	0.026	0.054	228493
<b>0.4</b>	-0.031	0.067	276120	0.027	0.080	241682
<b>0.6</b>	-0.039	0.103	276120	0.027	0.123	259060
<b>0.8</b>	-0.037	0.155	276120	0.033	0.171	264795
<b>1.0</b>	-0.031	0.211	276120	0.042	0.220	267165

The results in Table A-7 show that adding positive/negative specified noise leads to, on average, negative/positive biases in the retrieved AOD. These are somewhat unexpected since one would think that an increased TOA reflectance would lead to an increase in the retrieved AOD. The counter-intuitive results can be attributed to the dynamic selection of aerosol model (fine/coarse aerosol types and fine mode weight). As shown in , perturbing the TOA reflectance by adding noise changes the spectral shape of reflectances. As a result, larger/smaller aerosol model is selected when the

positive/negative noise is added. Due to different aerosol models being selected, increasing/decreasing TOA reflectance can lead to smaller/larger AOD being retrieved, and the impact increases as the input AOD increases.

Table A-8. Bias and standard deviation (Std.dev) of the Ångström Exponent retrieved over water from noisy reflectance relative to that from noise-free reflectance.

<b>Ångström Exponent (0.47-0.86 µm)</b>						
<b>Input AOD</b>	<b>Positive Noise Added</b>			<b>Negative Noise Added</b>		
	<b>Bias</b>	<b>Std. dev</b>	<b>Number</b>	<b>Bias</b>	<b>Std. dev</b>	<b>Number</b>
<b>0.05</b>	-0.611	0.543	276120	0.700	0.552	51878
<b>0.1</b>	-0.308	0.396	276120	0.424	0.371	132643
<b>0.15</b>	-0.166	0.328	276120	0.334	0.334	180733
<b>0.2</b>	-0.091	0.281	276120	0.274	0.300	206434
<b>0.3</b>	-0.025	0.249	276120	0.200	0.237	228493
<b>0.4</b>	-0.012	0.231	276120	0.160	0.207	241682
<b>0.6</b>	-0.008	0.214	276120	0.122	0.179	259060
<b>0.8</b>	-0.008	0.186	276120	0.097	0.157	264795
<b>1.0</b>	-0.008	0.167	276120	0.081	0.143	267165
<b>Ångström Exponent (0.86-2.13 µm)</b>						
<b>Input AOD</b>	<b>Positive Noise Added</b>			<b>Negative Noise Added</b>		
	<b>Bias</b>	<b>Std. dev</b>	<b>Number</b>	<b>Bias</b>	<b>Std. dev</b>	<b>Number</b>
<b>0.05</b>	-0.810	0.853	276120	0.791	0.643	51878
<b>0.1</b>	-0.685	0.778	276120	0.613	0.530	132643
<b>0.15</b>	-0.602	0.724	276120	0.537	0.518	180733
<b>0.2</b>	-0.543	0.685	276120	0.462	0.487	206434
<b>0.3</b>	-0.465	0.638	276120	0.348	0.429	228493
<b>0.4</b>	-0.405	0.602	276120	0.259	0.368	241682
<b>0.6</b>	-0.322	0.523	276120	0.152	0.336	259060
<b>0.8</b>	-0.258	0.436	276120	0.113	0.294	264795
<b>1.0</b>	-0.224	0.384	276120	0.102	0.230	267165

Table A-9. Bias and standard deviation (Std.dev) of AOD retrieved over land from noisy reflectances relative to that from noise-free reflectance.

<b>Input AOD</b>	<b>Positive Noise Added</b>			<b>Negative Noise Added</b>		
	<b>Bias</b>	<b>Std. dev</b>	<b>Number</b>	<b>Bias</b>	<b>Std. dev</b>	<b>Number</b>
<b>0.05</b>	0.017	0.010	21880	-0.016	0.009	21816
<b>0.1</b>	0.016	0.013	21880	-0.012	0.016	21816

<b>0.15</b>	0.015	0.018	21880	-0.009	0.020	21816
<b>0.2</b>	0.016	0.022	21880	-0.012	0.021	21816
<b>0.3</b>	0.025	0.111	21880	-0.016	0.028	21816
<b>0.4</b>	0.035	0.176	21880	-0.016	0.049	21816
<b>0.6</b>	0.038	0.149	21880	-0.017	0.060	21816
<b>0.8</b>	0.041	0.202	21880	-0.017	0.106	21816
<b>1.0</b>	0.054	0.359	21880	-0.006	0.263	21816

Table A-10. Bias and standard deviation (Std.dev) of the Ångström Exponent retrieved over land from noisy reflectance relative to that from noise-free reflectance.

<b>Ångström Exponent (0.47-0.86 µm)</b>						
<b>Input AOD</b>	Positive Noise Added			Negative Noise Added		
	Bias	Std. dev	Number	Bias	Std. dev	Number
<b>0.05</b>	0.296	0.402	21880	-0.597	0.420	21816
<b>0.1</b>	0.285	0.436	21880	-0.664	0.537	21816
<b>0.15</b>	0.263	0.434	21880	-0.443	0.567	21816
<b>0.2</b>	0.215	0.404	21880	-0.223	0.461	21816
<b>0.3</b>	0.121	0.300	21880	-0.058	0.259	21816
<b>0.4</b>	0.067	0.211	21880	-0.032	0.210	21816
<b>0.6</b>	0.038	0.191	21880	-0.019	0.188	21816
<b>0.8</b>	0.010	0.180	21880	-0.015	0.193	21816
<b>1.0</b>	-0.018	0.159	21880	-0.011	0.206	21816
<b>Ångström Exponent (0.86-2.13 µm)</b>						
<b>Input AOD</b>	Positive Noise Added			Negative Noise Added		
	Bias	Std. dev	Number	Bias	Std. dev	Number
<b>0.05</b>	0.253	0.323	21880	-0.488	0.338	21816
<b>0.1</b>	0.253	0.361	21880	-0.545	0.441	21816
<b>0.15</b>	0.244	0.377	21880	-0.368	0.487	21816
<b>0.2</b>	0.210	0.372	21880	-0.180	0.432	21816
<b>0.3</b>	0.130	0.308	21880	-0.021	0.288	21816
<b>0.4</b>	0.074	0.251	21880	0.010	0.262	21816
<b>0.6</b>	0.029	0.259	21880	0.023	0.243	21816
<b>0.8</b>	-0.008	0.267	21880	0.019	0.236	21816
<b>1.0</b>	-0.224	0.384	276120	0.102	0.230	267165

The results presented in the tables above indicate that effects of perturbing TOA reflectance with noise on the aerosol retrieval are three-fold:

1. Increasing/decreasing TOA reflectance in the reference channel (0.86  $\mu\text{m}$  for water and 0.47  $\mu\text{m}$  for land) directly leads to higher/lower AOD being retrieved (if same aerosol model is used).
2. The change of spectral shape of TOA reflectance leads to different aerosol models being selected.
3. Over land, change of TOA reflectance at SWIR channel affects the estimated surface reflectance.

As a result, the impact on the retrieved AOD is not straightforward. As shown in the tests over water, an increase of TOA reflectance leads to decreased AOD on average.

Defining the Signal-to-Noise Ratio in terms of AOD (SNR-AOD) as the ratio of input AOD over the standard deviation of retrieval error, it is seen that for a typical AOD value of 0.15 over water, the SNR-AOD is  $\sim 5$ . Over land, for a typical value of 0.2, the SNR-AOD is  $\sim 10$ . These SNR-AOD values suggest that the noise for the 2-km “pixel” is small enough to retrieve an AOD.

## B. Sunlint directional reflectance

In calculating the reflectance of water Cox and Munk (1954) considered the system of coordinates (P,X,Y,Z) where P is the observed point, Z the altitude, PY is pointed to the sun direction and PX to the direction perpendicular to the sun plane. Using spherical trigonometry, the components of surface slope  $Z_x$  and  $Z_y$  which is so inclined to reflect an incoming ray from the sun toward the satellite can be related to the sun-satellite geometry through:

$$Z_x = \frac{-\sin(\theta_v)\sin(\phi_s - \phi_v)}{\cos(\theta_s) + \cos(\theta_v)}; \quad (\text{B-1})$$

$$Z_y = \frac{\sin(\theta_s) + \sin(\theta_v)\cos(\phi_s - \phi_v)}{\cos(\theta_s) + \cos(\theta_v)} \quad (\text{B-2})$$

To simplify the calculation, the (P,X,Y) coordinate system is rotated to a new set of principal axes (P, X', Y') with PY' parallel to the wind direction. The slope components are now expressed as:

$$Z'_x = \cos(\chi)Z_x + \sin(\chi)Z_y; \quad (\text{B-3})$$

$$Z'_y = -\sin(\chi)Z_x + \cos(\chi)Z_y, \quad (\text{B-4})$$

where  $\chi$  is the relative azimuth angle between sun and wind direction. The possibility for the occurrence of such slope is calculated as:

$$p(Z'_X, Z'_Y) = (2\pi\sigma'_X\sigma'_Y)^{-1} \exp\left(-\frac{\xi^2 + \eta^2}{2}\right) \times \left\{ \begin{aligned} &1 - \frac{1}{2}C_{21}(\xi^2 - 1)\eta - \frac{1}{6}C_{03}(\eta^3 - 3\eta) + \frac{1}{24}C_{40}(\xi^4 - 6\xi^2 + 3) + \\ &\frac{1}{4}C_{22}(\xi^2 - 1)(\eta^2 - 1) + \frac{1}{24}C_{04}(\eta^4 - 6\eta^2 + 3) \end{aligned} \right\} \quad (\text{B-5})$$

where  $\xi = Z'_X/\sigma'_X$  and  $\eta = Z'_Y/\sigma'_Y$ .  $\sigma'_X$  and  $\sigma'_Y$  are the root mean square values of  $Z'_X$  and  $Z'_Y$ , the skewness coefficients  $C_{21}$  and  $C_{03}$ , and the peakedness coefficients  $C_{40}$ ,  $C_{22}$  and  $C_{04}$  have been defined by Cox and Munk for a clean surface as follows:

$$\begin{aligned} \sigma'^2_X &= 0.003 + 0.00192ws; & \sigma'^2_Y &= 0.00316ws \\ C_{21} &= 0.01 - 0.0086ws; & C_{03} &= 0.04 - 0.033ws \\ C_{40} &= 0.40, & C_{22} &= 0.12; & C_{04} &= 0.23, \end{aligned}$$

where  $ws$  is the wind speed with a lower limit set as 0.1 m/s to ensure numerical stability.

The directional reflectance is written as:

$$\rho_{sgt}(\theta_s, \theta_v, \phi_s, \phi_v) = \frac{\pi \cdot p(Z'_X, Z'_Y) \cdot R(n_r, n_i, \theta_s, \theta_v, \phi_s, \phi_v)}{4 \cdot \cos\theta_s \cdot \cos\theta_v \cdot \cos^4\beta}, \quad (\text{B-6})$$

where  $\beta$  is the tilt ( $\tan\beta = \sqrt{Z'^2_X + Z'^2_Y}$ ).

Fresnel's reflection Coefficient  $R(n_r, n_i, \theta_s, \theta_v, \phi_s, \phi_v)$  is computed as:

$$R(n_r, n_i, \theta_s, \theta_v, \phi_s, \phi_v) = \frac{1}{2} \left\{ \frac{[(n_r^2 - n_i^2)\cos\theta_i - u]^2 + [2n_r n_i \cos\theta_i + v]^2}{[(n_r^2 - n_i^2)\cos\theta_i + u]^2 + [2n_r n_i \cos\theta_i - v]^2} + \frac{(\cos\theta_i - u)^2 + v^2}{(\cos\theta_i + u)^2 + v^2} \right\} \quad (\text{B-7})$$

where,

$$\begin{aligned} u^2 &= \frac{1}{2} \left\{ |n_r^2 - n_i^2 - \sin^2\theta_i| + \sqrt{(n_r^2 - n_i^2 - \sin^2\theta_i)^2 + 4n_r^2 n_i^2} \right\} \\ v^2 &= \frac{1}{2} \left\{ -|n_r^2 - n_i^2 - \sin^2\theta_i| + \sqrt{(n_r^2 - n_i^2 - \sin^2\theta_i)^2 + 4n_r^2 n_i^2} \right\} \\ \cos\theta_i &= \sqrt{\frac{1}{2} [1 + \cos\theta_s \cos\theta_v + \sin\theta_s \sin\theta_v \cos(\phi_s - \phi_v)]} \\ \sin\theta_i &= \sqrt{\frac{1}{2} [1 - \cos\theta_s \cos\theta_v - \sin\theta_s \sin\theta_v \cos(\phi_s - \phi_v)]} \end{aligned}$$

Normalized integral of downward diffuse radiation by sunglint directional reflectance  $\overline{\rho_{sgt}}$  is pre-calculated using the 6S RTM and stored in LUT for varying geometry (solar zenith angle, local zenith angle, and relative azimuth (sun – satellite)),

aerosol model and optical depth, and surface wind speed (see section 3.4.4).  $\overline{\rho'_{sgt}}$  is the normalized integral of upward diffuse radiation by sunglint directional reflectance and can be obtained from the same LUT as  $\overline{\rho_{sgt}}$  by swapping solar zenith and local zenith angles. Linear interpolation is used for intermediate values of arguments from LUT. Noted that wind direction is fixed when calculating  $\overline{\rho_{sgt}}$  and  $\overline{\rho'_{sgt}}$  in the glint LUT, but not for explicit calculation of specular reflection (calculated with analytical Fresnel Equation).

The sunglint spherical albedo  $\overline{\overline{\rho_{sgt}}}$  is also calculated following 6S RTM. In each ABI channel, the sunglint spherical albedo decreases with wind speed from 2 to 14 m/s by about 5%, therefore it is parameterized as a function of surface wind speed.

## C. Internal checks for aerosol retrieval

### C.1. Snow/ice contamination over land

In addition to the official MODIS snow mask, the MODIS aerosol team of NASA/GSFC developed an empirical method using an NDVI-like ratio of 0.86- and 1.24- $\mu\text{m}$  reflectances and the 11- $\mu\text{m}$  brightness temperature to mask out residual snow/ice contamination over land as:  $(\rho_{0.86} - \rho_{1.24})/(\rho_{0.86} + \rho_{1.24}) > 0.05$ , and  $T_{11,\mu\text{m}} < 285\text{K}$  [Li et al., 2005]. To adapt such an approach for ABI, the 1.24- $\mu\text{m}$  channel is replaced by 1.61  $\mu\text{m}$  since the 1.24- $\mu\text{m}$  channel is not available on ABI. An analysis, similar to the one done for the VIS/SWIR land surface relationship in Section 3.4.2.3, is conducted using seven years of MODIS reflectances. The normalized difference snow index (NSDI)  $(\rho_{0.86} - \rho_{1.61})/(\rho_{0.86} + \rho_{1.61})$ , called 1.61- $\mu\text{m}$  NSDI, was studied in terms of  $(\rho_{0.86} - \rho_{1.24})/(\rho_{0.86} + \rho_{1.24})$ , called 1.24- $\mu\text{m}$  NSDI, for the thresholds of  $> 0.05$  or  $\leq 0.05$  respectively. As shown in Figure C-1, where the frequency of 1.61- $\mu\text{m}$  NSDI is plotted as a function of the 1.24- $\mu\text{m}$  NSDI, the overlap area between 1.24- $\mu\text{m}$  NSDI  $> 0.05$  and 1.24- $\mu\text{m}$  NSDI  $\leq 0.05$  is only about 10%, which suggests the 1.61- $\mu\text{m}$  NSDI maybe a good substitute, and the corresponding threshold is about 0.2 at the cross-over point. Therefore, the relationship to rule out snow-contamination was transformed for ABI use as:

$$(\rho_{0.86} - \rho_{1.61})/(\rho_{0.86} + \rho_{1.61}) > 0.2, \quad (\text{C-1})$$

$$\text{and } T_{11,\mu\text{m}} < 285\text{K}. \quad (\text{C-2})$$

This test, however, is currently not implemented as it requires further testing. The thresholds will also need to be adjusted after GOES-R launch.

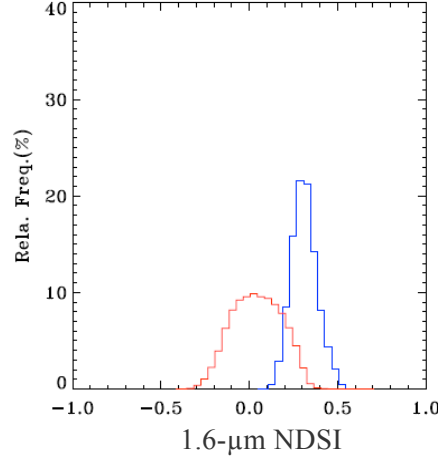


Figure C-1: Relative frequency of 1.6- $\mu\text{m}$  NDSI, i.e.  $(\rho_{0.86} - \rho_{1.61})/(\rho_{0.86} + \rho_{1.61})$ , for 1.24- $\mu\text{m}$  NDSI (i.e.  $(\rho_{0.86} - \rho_{1.24})/(\rho_{0.86} + \rho_{1.24}) > 0.05$  (in blue) and 1.24- $\mu\text{m}$  NDSI  $\leq 0.05$  (in red) using MODIS reflectances.

## C.2. Glint

Aerosol is only retrieved over dark ocean, i.e., away from glint. The glint angle is the angle between the viewing direction and the direction of specular reflection and defined as,

$$\theta_g = \cos^{-1}((\cos\theta_s \cos\theta_v) - (\sin\theta_s \sin\theta_v \cos\phi)), \quad (\text{C-3})$$

where  $\theta_s$ ,  $\theta_v$ , and  $\phi$  are the solar zenith, the view zenith and the relative azimuth angles (between the sun and satellite), respectively. If  $\theta_g > 40^\circ$ , retrieval is not performed to avoid glint contamination [Remer et al., 2006]. This test is implemented in the ABI aerosol algorithm.

## C.3. Turbid water over ocean

The algorithm adopts the MODIS techniques for glint and turbid water screening over ocean. The method to rule out the turbid water over coastal area uses the unique spectral signature by strong water absorption different from sediments in the water or a shallow ocean floor [Li et al., 2003]. It uses  $\Delta\rho_{0.55} > 0.01$ , i.e. the reflectance difference at 0.55  $\mu\text{m}$  between observed and the interpolation based on the power law derived from 0.47, 1.24, 1.64 and 2.13- $\mu\text{m}$  channels, and with the additional test  $\rho_{0.49} \leq 0.25$  to avoid misidentification of heavy dust/smoke from turbid water. Since ABI does not have the 0.55- $\mu\text{m}$  channel the 0.66- $\mu\text{m}$  is studied as an alternative.  $\Delta\rho_{0.66}$  is studied in terms of  $\Delta\rho_{0.55} > 0.01$  or  $\leq 0.01$ , respectively, using seven years of MODIS reflectance (Figure C-2). However, the overlap area between the red and blue lines is over 30% with a cross-

over point of near zero, and thus may not well-separate turbid water. A coastal map as ancillary input needs to be considered to assist in flagging coastal area. This test is currently not implemented as it requires further testing.

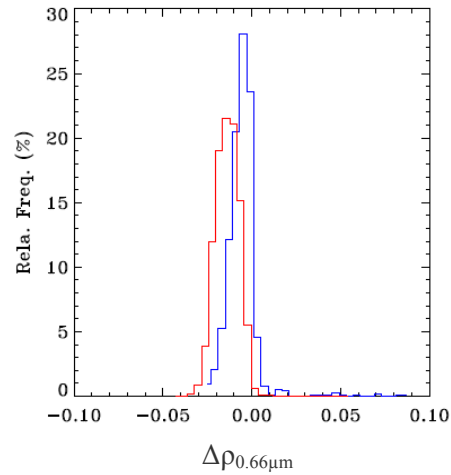


Figure C-2: Relative frequency of  $\Delta\rho_{0.66}$  for  $\Delta\rho_{0.55} > 0.01$  (turbid water indicator, in blue) and  $\Delta\rho_{0.55} \leq 0.01$  (in red) using MODIS reflectances.

## Appendix D: Common Ancillary Data Sets

### 1. LAND\_MASK\_NASA\_1KM

#### *a. Data description*

**Description:** Global 1km land/water used for MODIS collection 5

**Filename:** lw\_geo\_2001001\_v03m.nc

**Origin:** Created by SSEC/CIMSS based on NASA MODIS collection 5

**Size:** 890 MB.

**Static/Dynamic:** Static

#### *b. Interpolation description*

The closest point is used for each satellite pixel:

- 1) Given ancillary grid of large size than satellite grid
- 2) In Latitude / Longitude space, use the ancillary data closest to the satellite pixel.

### 2. MDS\_L2\_CLD\_MASK\_FILE

#### *a. Data description*

**Description:** MODIS L2 cloud mask 1km

**Filename:** MOD35\_L2.AYYYYDDD.HHMM.005.yyydddhhmmss.nc /  
MYD35\_L2.AYYYYDDD.HHMM.005.yyydddhhmmss.nc.

Where,

MOD35\_L2/ MYD35\_L2 – Level 2 Cloud Mask from TERRA  
(MOD) /

AQUA (MYD)

A – Nothing to do here

YYYYDDD – 4 digit year plus 3 digit of Julian day

HHMM – 2 digit of hour and 2 digit of minutes in GMT

005 – Processing system version

yydddhhmmss – processing date/time

**Origin:** NASA DAAC

**Size:** 45 MB

**Static/Dynamic:** Dynamic

***b. Interpolation description***

The closest point is used for each satellite pixel:

In Latitude / Longitude space, use the ancillary data closest to the satellite pixel.

**3. MDS\_L2\_OZON\_5KM\_FILE**

***a. Data description***

**Description:** MODIS L2 ozone 5km

**Filename:** MOD07\_L2.AYYYYDDD.HHMM.005.yyyydddhhmmss.nc /  
MYD07\_L2.AYYYYDDD.HHMM.005.yyyydddhhmmss.nc.

Where,

MOD07\_L2/ MYD07\_L2 – Level 2 Product Name from TERRA (MOD) /

AQUA (MYD)

A – Nothing to do here

YYYYDDD – 4 digit year plus 3 digit of Julian day

HHMM – 2 digit of hour and 2 digit of minutes in GMT

005 – Processing system version

yyydddhhmmss – processing date/time

**Origin:** NASA DAAC

**Size:** 31 MB

**Static/Dynamic:** Dynamic

***b. Interpolation description***

The closest point is used for each satellite pixel:

In Latitude / Longitude space, use the ancillary data closest to the satellite pixel.

**4. MDS\_L2\_TPW\_5KM\_FILE**

***a. Data description***

**Description:** MODIS L2 TPW 5km

**Filename:** MOD07\_L2.AYYYYDDD.HHMM.005.yyyydddhhmmss.nc /  
MYD07\_L2.AYYYYDDD.HHMM.005.yyyydddhhmmss.nc.

Where,  
MOD07\_L2/ MYD07\_L2 – Level 2 Product Name from TERRA  
(MOD) /

AQUA (MYD)

A – Nothing to do here

YYYYDDD – 4 digit year plus 3 digit of Julian day

HHMM – 2 digit of hour and 2 digit of minutes in GMT

005 – Processing system version

yyyymmddhhmmss – processing date/time

**Origin:** NASA DAAC

**Size:** 31 MB

**Static/Dynamic:** Dynamic

### ***b. Interpolation description***

The closest point is used for each satellite pixel:

In Latitude / Longitude space, use the ancillary data closest to the satellite pixel.

## **5. NWP\_GFS**

### ***a. Data description***

**Description:** NCEP GFS model data in grib format – 1 x 1 degree  
(360x181), 26 levels

**Filename:** gfs.tHHz.pgrbfhh

Where,

HH – Forecast time in hour: 00, 06, 12, 18

hh – Previous hours used to make forecast: 00, 03, 06, 09

**Origin:** NCEP

**Size:** 26MB

**Static/Dynamic:** Dynamic

### ***b. Interpolation description***

There are three interpolations are installed:

**NWP forecast interpolation from different forecast time:**

Load two NWP grib files which are for two different forecast time and interpolate to the satellite time using linear interpolation with time difference.

Suppose:

T1, T2 are NWP forecast time, T is satellite observation time, and T1 < T < T2. Y is any NWP field. Then field Y at satellite observation time T is:

$$Y(T) = Y(T1) * W(T1) + Y(T2) * W(T2)$$

Where W is weight and

$$W(T1) = 1 - (T-T1) / (T2-T1)$$
$$W(T2) = (T-T1) / (T2-T1)$$

**NWP forecast spatial interpolation from NWP forecast grid points. This interpolation generates the NWP forecast for the satellite pixel from the NWP forecast grid dataset.**

The closest point is used for each satellite pixel:

- 1) Given NWP forecast grid of large size than satellite grid
- 2) In Latitude / Longitude space, use the ancillary data closest to the satellite pixel.

**NWP forecast profile vertical interpolation**

Interpolate NWP GFS profile from 26 pressure levels to 101 pressure levels

For vertical profile interpolation, linear interpolation with Log pressure is used:

Suppose:

y is temperature or water vapor at 26 levels, and y101 is temperature or water vapor at 101 levels. p is any pressure level between p(i) and p(i-1), with p(i-1) < p < p(i). y(i) and y(i-1) are y at pressure level p(i) and p(i-1). Then y101 at pressure p level is:

$$y_{101}(p) = y(i-1) + \log( p[i] / p[i-1] ) * ( y[i] - y[i-1] ) / \log ( p[i] / p[i-1] )$$

## 6. SFC\_ELEV\_GLOBE\_1KM

### a. *Data description*

**Description:** Digital surface elevation at 1km resolution.

**Filename:** GLOBE\_1km\_digelev.nc

**Origin:** NGDC

**Size:** 1843.2 MB

**Static/Dynamic:** Static

### b. *Interpolation description*

The closest point is used for each satellite pixel:

- 1) Given ancillary grid of large size than satellite grid
- 2) In Latitude / Longitude space, use the ancillary data closest to the satellite pixel.

## 7. SNOW\_MASK\_IMS\_SSMI

### a. *Data description*

**Description:** Snow/Ice mask, IMS – Northern Hemisphere, SSM/I – Southern Hemisphere

4km resolution – the 25 km SSM/I has been oversampled to 4km

**Filename:** snow\_map\_4km\_YYMMDD.nc

**Origin:** CIMSS/SSEC

**Size:** 39 MB.

**Static/Dynamic:** Dynamic

### b. *Interpolation description*

The closest point is used for each satellite pixel:

- 1) Given ancillary grid of large size than satellite grid
- 2) In Latitude / Longitude space, use the ancillary data closest to the satellite pixel.